Doctoral Dissertation
Doctoral Program in Civil and Environmental Engineering (34th Cycle)

Mixing Processes in Hyporheic Sediments

By

Ahmed Monofy

******

Supervisor(s):
Prof. Fulvio Boano, Supervisor, Politecnico di Torino, Italy
Prof. Stanley B. Grant, Co-Supervisor, Virginia Tech, USA

Doctoral Examination Committee:

Prof. Alessandra Marzadri, Università di Trento, Italy
Dr. Susa Stonedahl, St. Ambrose University, USA
Prof. Andrea Bottacin-Busolin, University of Padua, Italy
Prof. Roberto Revelli, Politecnico di Torino, Italy
Prof. Ilaria Butera, Politecnico di Torino, Italy

Politecnico di Torino
2022

Declaration

I hereby declare that the contents and organization of this dissertation constitute my own original work and does not compromise in any way the rights of third parties, including those relating to the security of personal data.

Ahmed Monofy

2022

* This dissertation is presented in partial fulfillment of the requirements for **Ph.D. degree** in the Graduate School of Politecnico di Torino (ScuDo).

To all the people out there who love science even if they are not scientists. To the ones who have dedicated their life to unravel the mysteries of this world and bring us a better livable world. To the successors who will pursue our journey for better environment.

"Let us not forget that human knowledge and skills alone cannot lead humanity to a happy and dignified life."

-Albert Einstein

Acknowledgment

During these years of my Ph.D., I have learnt many things on the personal and professional level. I have met many people who have left a great impact on me; the way I think and everything. Since my childhood, I love science, discovering and above all learning. Along this journey, I had the chance to learn many more things and gain more skills, which, undoubtedly, will have an influence on me during the rest of my life.

I am grateful that I had the chance of working under the supervision of two great and well-known professors, from whom I have learnt many things on the personal level and in science. Moreover, I had the opportunity, with the help of my supervisors, who have facilitated many things for me, to have an international experience by spending a long period of my Ph.D. abroad and being associated with two different and well-known universities.

Thank you, Fulvio! You have been very supportive and helpful to me since the beginning to fit in and facilitated everything for me to have a great start with my Ph.D. One of the things that made me happy during this journey is the feeling that you have faith in me, and that you believe in me. I learnt from you many things on the academic level and on the personal level, which of course improved my skills. I have always believed that being smart and hard worker is everything. However, now, I am sure that your supervisor and with who you work have a crucial role; they can encourage you to achieve many things and they can disappoint you and exhaust your skills for nothing. It was a great opportunity to have you as my supervisor, and I hope that this is just the start of us working together, and for me having the chance of learning more from you, thank you again!

Thank you, Stan! I am pleased to have the chance to know you and work under your supervision. The chance that I had to work in the Occoquan lab and follow your class was helpful for me and really improved my scientific skills. “In science, you have to be always up to date”, this sentence (probably not exactly the words but the meaning) you told me once during a ride, and it is still in my mind. This spurs my instinct of learning more and not rely only on what I have learnt so far or what is already known. Thank you, for helping me to settle in during the period that I spent at the lab, and I am looking forward to working with you and learning more.

I would like to thank my parents, to whom I owe all of this, and all whatever I will achieve in my life. Thank you, Mother, for being always caring about me. You have taught me many things since I was young, you gave up everything to take care of me, and I will never forget this. I always loved you and I will always love you. I know it was hard for you every time I have to travel, but you always support me because you believe in me. You made me more stubborn and eager to achieve more success in my life, at least to partially compensate for the time that I am not spending with you. Thank you, Father, you have always believed in me, and always supported me and pushed me to new experiences. You have always trusted me and gave me the chance since my childhood to be independent and learn from my mistakes on my own. Thank you for your financial support during all these years of studying, and all you want is seeing me happy and in the place that is satisfactory for me.

Thank you, Samar. Over this time since I have known you and became my fiancée, you have been a great support during this journey. Thank you for being proud of me, as well as I am proud of you. Even though we like to be always close to each other, you have pushed me to work more on my career. Your support along this journey meant a lot to me.

Many thanks to all the people of DIATI, all technical and research staff, I had the honor to share this experience with, in particular, the people of BAD3: Alice,

Hamed, Cosimo, Lorenzo, Matteo, Bert, Roberto, Davide, Sofia, Usama, Melissa and all my colleagues who have supported me along the way. I hope that our friendship lasts forever.

Many thanks to the family of the Occoquan lab and Virginia Tech, who helped me during my stay in the USA. I had the chance to meet great and caring people. Thank you, Emily, Shantanu, Mimi, and Marilyn, for helping me to settle in the new place and including me in the lab family easily. Thank you, Dr. Megan, for your classes on statistics and your help with my papers and thesis. I wish health and happiness for all of you.

Finally: "The authors acknowledge Compania San Paolo and the U.S. National Science Foundation (NSF) funding for the research that has been done during this PhD."

Thanks to all the people that I did not mention but that, one way or another, they were by my side. Thank you because...

"Believe in yourself, and choose your life company"

Abstract

Hyporheic exchange is the main driver of the biogeochemical transformations of nutrients in streambeds. The bed morphology and its interactions with surface flow induce different scales of flow in the hyporheic zone. The aim of this study is to better understand the mixing processes underpinning hyporheic exchange in streams. Improving our ability to quantify the mixing processes in stream sediments is crucial for enhancing the study of biogeochemical processes involving nutrients and other contaminants in streams.

Alternate bars are one of the complex morphologic configurations that can affect the characteristics of the hyporheic zone. The modeling results presented in this thesis show that two main hyporheic zones are formed in sediments with alternate bars: a shallow zone that is highly linked to the streamflow, and a deep one that is more influenced by groundwater flux variations. This distinction between the two zones is reflected in the hyporheic residence times distribution (RTD), that displays a bimodal shape. This bimodality is enhanced by anisotropic sediment conditions, while it is much milder in isotropic ones. The bar submergence has various effects on the hyporheic zone characteristics; higher bar submergence induces less hyporheic flow with longer residence times in the shallow zone. Moreover, the deep zone is significantly affected by the groundwater flux, which decreases exchange flow, hyporheic extent in the sediment, residence times, and the area of exchange. The hyporheic extent is further enhanced by sediment anisotropy.

Considering a different type of streambed morphology, dune-shaped bedforms have been shown to play a paramount role in driving hyporheic exchange. An analytical representation of the RTDs would be important to facilitate the study of hyporheic exchange processes because of the importance of the RTD for biogeochemical reactions in the hyporheic zone (e.g., as quantified by the Damköhler number). The analysis considered different conditions in terms of dimensionless sediment depth d_b^* and groundwater underflow u_b^* and their influence on the shape of the hyporheic RTD was assessed. Empirical RTDs were generated, over a range of combinations of d_b^* and u_b^* values, with numerical particle tracking experiments. The resulting hyporheic RTDs were then compared to different analytical distributions (Exponential (EXP), Gamma (GAM), Lognormal (LN) and Fréchet (FR)) with the Anderson-Darling test. The empirical

RTDs were found to be represented by different distributions over the considered range of d_b^* and u_b^*. FR is the best fit for deep beds ($d_b^* > 3.2$) and negligible underflow ($u_b^* < 0.1$). LN is often the best representation for $u_b^* \leq 0.8$, while GAM performs better for larger values of u_b^*. In general, LN provides a good description of the empirical RTDs in all cases, as it was identified as either the best or the second-best fitting distribution. The parameters of these analytical distributions vary with d_b^* and u_b^*.

The analysis described above relied on the adoption of a physically based model of hyporheic exchange induced by the streambed morphology. A different approach to describe the surface water-groundwater interactions was also considered in this thesis. It employs the diffusion equation to represent the overall transfer at the Sediment Water Interface (SWI), lumping all the physical mixing processes in the so-called effective diffusion. Specifically, a 1-D diffusive model was adopted to describe the vertical exchange at SWI and in the benthic biolayer, the biologically active upper ($\sim 2 - 5$ cm) layer of the streambed. The model was here applied to an extensive set of previously published laboratory experiments with different morphology types**:** flat beds, ripples and dunes, and alternate bars. Although there are different physical processes at the SWI associated with these morphology types, the overall mixing can be very well represented by a parsimonious diffusion based model controlled by only two parameters. These parameters define the exponential diffusivity model, are the effective diffusion coefficient at the SWI and the decay coefficient of the exponential profile. Moreover, a single predictive equation can estimate the effective diffusion coefficient based on stream and sediment properties. However, different equations are required to predict the decay coefficient of the exponential profile for each morphology type.

Finally, the thesis also focused on travel times of solutes on a much larger spatial scale. The travel times of salt tracers were examined in the Occoquan reservoir in northern Virginia (USA) as a case study. Observed time series of solute concentration and solute load, and discharge time series, were analyzed using a geostatistical method to determine the travel times distribution. The Occoquan reservoir is very relevant as it hosts the Fairfax water treatment plant, that is the main water supply for the surrounding region, and it is affected by the increasing salt concentration in recent years. The analysis of the concentration time series revealed that the salt takes $8 - 9$ days to travel through the system, while analysis of time series of the salt load – as well as discharge – indicated a much faster response (from 5 to 14 hours). These results can be useful in the regulation and operation of the Occoquan reservoir.

Contents

1. Chapter 1 Introduction 1
    1.1 Solute Exchange between Water Column and Sediment 1
        1.1.1 Hyporheic Exchange Characteristics 1
        1.1.2 Solute Transport at the Sediment Water Interface using a Diffusive description. 2
    1.2 Salt Load as a Conservative Solute in Freshwater 3
    1.3 Thesis Outline 4
2. Chapter 2 Hyporheic Zone Characteristics in Alternate Bars 7
    2.1 Introduction. 7
    2.2 Methodology 8
        2.2.1 Alternate Bars Geometry. 9
        2.2.2 Surface Water Modeling. 10
        2.2.3 Groundwater Modeling. 11
        2.2.4 Predictive Model Derivation. 13
    2.3 Results and Discussion. 15
        2.3.1 Hydraulic Head Distribution on Streambed. 15
        2.3.2 Hyporheic Flow and Area. 15
        2.3.3 Hyporheic Residence Times. 21
        2.3.4 Hyporheic Depths. 29
        2.3.4 Predictive Model Results. 33
    2.4 Concluding Remarks. 37
3. Chapter 3 The Effect of Sediment Depth and Groundwater Underflow on Hyporheic Residence Times Distribution in Dune-Like Bedform 42
    3.1 Introduction 42
    3.2 Methodology 44
        3.2.1 Numerical Generation of Empirical RTDs 44
        3.2.2 The Inference of the Analytical Distribution Parameters 47

3.3 Results 48
3.3.1 Hyporheic Flow Paths 48
3.3.2 Analytical Representation of the Empirical RTDs. 49
3.3.3 Inferring the Parameters of the Analytical distributions 52
3.4 Application for Estimating the Damkhöler Number. 53
3.5 Discussions 56
3.6 Conclusion Remarks 58
4. Chapter 4 Diffusive Description of Vertical Mixing in the Benthic Biolayer for Different Stream Morphology. 61
4.1 Introduction 61
4.2 Methodology 62
4.2.1 The Diffusivity Model Framework 62
4.2.2 Dataset Description 64
4.2.3 Classification and Regression Tree (CART) Analysis 66
4.2.4 Multiple Linear Regression (MLR) 67
4.3 Results 68
4.3.1 C Profile versus E Profile Performance 68
4.3.2 The Magnitude and Extent of the Mixing Processes. 69
4.3.3 CART Analysis Results 70
4.3.4 MLR Results 71
4.3.5 Bed Configuration effect on the Mass Transport Process 76
4.4 Discussions 78
4.5 Conclusion Marks and Future research 80
5. Chapter 5 Geostatistical Method Application to Estimate the Response Time to Flow Waves, Salt Concentration and Load in the Occoquan Watershed in Northern Virginia 83
5.1 Introduction 83
5.2 Methodology 84
5.2.1 Data Collection 84

5.2.3 The Geostatistical Method 85
5.3 Results and Discussion 86
5.3.1 Response Time for Flow 86
5.3.2 Response Time for salt Concentration and load 90
5.4 Conclusion Remarks and Future research 92
6. Appendices 96
7. Nomenclature 112
8. REFERENCES 114

List of Figures

Figure 2.1: Water surface elevation for different Q_{surf} cases ((A) $0.5Q_{avg}$, (B) $Qavg$, (C) $2Q_{avg}$, (D) $3Q_{avg}$, (E) Q_{bf}) and bar submergence. The gray surface represents the streambed elevation of the middle alternate bar. 16

Figure 2.2: Hyporheic flux rate (q_h, m/s) spatial distribution over the middle bar in Q_{avg} (left column; A–F) and Q_{bf} (right column; G–L) under different ambient groundwater flux (q_{bot}) in anisotropic conditions. The red areas denote downwelling (losing) areas while the green ones indicate the upwelling (gaining) zones. The numbers in each panel that are written on the horizontal and vertical axes represent the streamwise and spanwise distances (in meters), respectively. .21

Figure 2.3: (A) Normalized hyporheic exchange flow (Q_h/Q_{h_n}) and (B) absolute hyporheic exchange flow (Q_h) values, in the anisotropic conditions. $qbotqhn$ on the horizontal axes represents gaining (positive sign) and losing (negative sign) conditions, where q_{bot} is the value of imposed ambient groundwater. Q_{h_n} and $qhn$are the hyporheic flow and flux, respectively, in the neutral condition. 21

Figure 2.4: Shallow flow paths (blue paths) and deep flow paths (red paths) directions and their associated cumulative RTDs under Q_{avg} (A and C), and Q_{bf} (B and D) cases, in neutral and anisotropic conditions. The blue and red parts of cumulative RTDs line correspond to the blue paths and the red paths, respectively. The blue and red arrows in A and B arrows represent the directions of shallow and deep flow paths, respectively. 23

Figure 2.5: Cumulative frequency distribution of residence times (F(RTs)) in neutral and anisotropic conditions under different streamflow cases ($0.5Q_{avg}$, Q_{avg}, $2Q_{avg}$, $3Q_{avg}$, and Q_{bf}). The gray arrow represents the direction of increasing the streamflow value. 24

Figure 2.6: Cumulative frequency distribution function of residence times (F(RTs)) under different gaining fluxes ($q_{bot} = 0$,$+0.5q_{h_n}$,$+q_{h_n}$,$+1.5\ q_{h_n}$, $+2q_{h_n}$, and $+3q_{h_n}$), and different Q_{surf} cases (Q_{avg} (A) and Q_{bf}(B)), in anisotropic conditions. 27

Figure 2.7: Cumulative frequency distribution of residence times (F(RTs)) in isotropic and anisotropic conditions, for Q_{avg} and Q_{bf} in neutral conditions.....28

Figure 2.8: Hyporheic flow paths extent, in neutral and anisotropic conditions, within the subsurface domain in (A) Q_{avg} and (B) Q_{bf} cases. The grey surface represents the streambed elevation. The flow paths direction is the same as the flow direction (from left to right).....29

Figure 2.9: (A) Shallow hyporheic depth ($Z_{10\%}$) normalized by its corresponding value in neutral condition ($Z_{10_{hn}}$). (B) Deep hyporheic depth ($Z_{90\%}$) normalized by its corresponding value in neutral condition ($Z_{90_{hn}}$). q_{bot}/q_{h_n} on the horizontal axes represents gaining ($+$ sign) and losing ($-$ sign) conditions, where q_{bot} is the value of imposed ambient groundwater and q_{h_n} is the hyporheic flux in neutral condition. The depths values in both (A and B) refer only to anisotropic conditions.....32

Figure 2.10: Comparison between simulated values of q_h/V and Q_h/Q_{surf}, and the predicted values by Eqs. (2.7) and (2.8); A and C are in neutral condition (Eq. (2.7)), and B and D are in gaining/losing conditions (Eq. (2.8)).....35

Figure 2.11: Comparison between simulated values of deep and shallow HZ dimensionless residence times ($\mathrm{RTs}_{90\%}\ K_v/d$ and $\mathrm{RTs}_{10\%}\ K_v/d$), and the predicted values by Eqs. (2.7) and (2.8) the simulations ones; A and C are in neutral condition (Eq. (2.7)), and B and D are in gaining/losing conditions (Eq. (2.8)).....36

Figure 2.12: Comparison between simulated values of deep and shallow HZ dimensionless residence times $Z_{90\%}/d$ and $Z_{10\%}/d$, and the predicted values by Eqs. (2.7) and (2.8) the simulations ones; A and C are in neutral condition (Eq. (2.7)), and B and D are in gaining/losing conditions (Eq. (2.8)).....37

Figure 3.1: A) Representative diagram of a conceptual model representing hyporheic exchange below a dune-like bedform, with pressure head distribution and consequent upwelling and downwelling zones due to the dune morphology. B) Simplified analytical model represented by a Tòth domain with a sinusoidal pressure variation creating upwelling and downwelling zones. 46

Figure 3.2: Pathlines induced by dune morphology in different combinations of d_b^* and u_b^*;(A) $d_b^* \to \infty$ and $u_b^* = 0$, (B) $d_b^* \to \infty$ and $u_b^* = 0.4$, (C) $d_b^* = 0.4$ and $u_b^* = 0$, (D) $d_b^* = 0.4$ and $u_b^* = 0.4$. 50

Figure 3.3: The effect of different values of (A) d_b^* and (B) u_b^* on empirical CDF. The black arrow shows the direction of d_b^* increase (A) and u_b^* increase (B). The black arrows in (A) and (B) indicate the increase in d_b^* and u_b^*, respectively. 51

Figure 3.4: Maps of (A) best and (B) second best analytical representative at different combinations of d_b^* and u_b^*.....51

Figure 3.5: The relative error associated with estimating (A) $t_{20\%}^*$, (B) $t_{50\%}^*$, and (C) $t_{80\%}^*$ by applying Eq. (3.19) on the best analytical distributions to represent the empirical CDF (Figure 3.4A).....52

Figure 3.6: The relative error associated with estimating (A) $t_{20\%}^*$, (B) $t_{50\%}^*$, and (C) $t_{80\%}^*$ by applying Eq. (3.19) on the second-best analytical distributions to represent the empirical CDF (Figure 3.4B). 52

Figure 3.7: Maps showing the parameters values for the four analytical distributions tested in this study ((A) EXP, (B) GAM, (C) LN, and (D) FR) at different combinations of d_b^* and u_b^*.....54

Figure 3.8: Comparison between the Damköhler number of respiration and denitrification (Da_{rp} and Da_{dn}, respectively) calculated at different d_b^* from the empirical RTD (Da_{Emp}), and the ones calculated by different analytical representations (Da_{GAM}, Da_{LN}, Da_{FR}, and Da_{EXP}).....56

Figure 3.9: Difference between relative errors associated with the best analytical representation (Figure 3.5) and the second-best one (Figure 3.6) for (A) $t_{20\%}^*$, (B) $t_{50\%}^*$, and (C) $t_{80\%}^*$.....58

Figure 4.1**:** The constant profile (A) vs the exponential profile (B). y is the vertical axis into the sediment domain, $D_{eff,0}^C$ and $D_{eff,0}^E$ are the effective diffusivity at the SWI for Constant and exponential profile, respectively. a is the decay coefficient of the exponential profile.....64

Figure 4.2: The stream, morphological, and sediment properties included in the CART analysis.....66

Figure 4.3: Fitting the C profile (dashed red line) and E profile (green line) to the flux out of the bed data (open black circles in (A)) of experiment B1 in Richardson and Parr (1988) study (A), and the dimensionless concentration in the water column (open black circles in (B)) of experiment 12 in Tonina and Buffington (2007) study (B).....68

Figure 4.4: Comparison between the fitting criteria of C profile (horizontal axis) vs E profile (vertical axis) in terms of AICc (A) and $R2$ (B) for the whole dataset considered in this study including flat bed, dunes, and alternate bars.....69

Figure 4.5: The effective diffusion coefficient (A) and the decay coefficient (B) values distribution for different morphologies (alternate bars, flat bed, and ripples and dunes). 70

Figure 4.6: The stream, morphological, and sediment properties included in the CART analysis. The cross-validation relative error (X-val relative error) variation with the tree complexity parameter (CP) is shown in A, and B for $\log(D_{eff,0})$ and $\log(a)$, respectively. The dashed black line in A and B represents the value of acceptable X-val relative error. The red arrows represent the pruning size of the tree. C and D are the pruned tree for $\log(D_{eff,0})$ and $\log(a)$. n is the number of data points falling in the corresponding branch. 71

Figure 4.7: Comparison between the fitted values of (A) $\log(D_{eff,0})$ and (B) $\log(a)$ using the E profile, and the predicted values by Eqs. (4.11) and (4.12), respectively. The solid black line is the $1:1$ line while the dashed lines are the 95% prediction interval (PI). 72

Figure 4.8: Comparison between the fitted values of (A) $\log(D_{eff,0}/D_m)$ and (B) $\log(a\ L_b)$ using the E profile, and the predicted values by Eqs. (4.15) and (4.16), respectively. The solid black line is the $1:1$ line while the dashed lines are the 95% prediction interval (PI). The vertical black lines associated with each point represents the measurement errors. 74

Figure 4.9: The variations of the inverse-decay depth over different ranges of the permeability Reynolds number in flat bed experiments (A) with vertical dash dotted lines represent the $\log(Re_k)$ values where $\log(a\ L_b)$ behaviour changes, the dotted black line represents the 95% prediction interval, and the solid line demonstrates the predicted values by Eq. (4.17). A comparison between the predicted values by Eq. (4.13), and the fitted values obtained by applying the diffusivity model on the flat bed experiments (B) with $1:1$ line (black line), and 95% prediction interval (dotted lines). The vertical black lines associated with each point represents the measurement errors. The long dash dots in (A) represents the Rek values of 0.1 and 1. 75

Figure 4.10: The predicted values of a by Eq. (4.18) versus the fitted values by applying the diffusivity model on ripples and dunes experiments. The solid line is the $1:1$ line, while the dotted line is the 95% predition interval. 76

Figure 4.11: The predicted values of $D_{eff,0}/D_m$ by Eq. (4.19) versus the fitted values by running the diffusivity model on the flat bed experiments. The solid line is the $1:1$ line, while the dashed line is the 95% predition interval. 77

Figure 4.12: The predicted diffusivity profile by Eq. (4.19) for $D_{eff,0}$ and Eq. (4.17) for a (solid lines) vs the fitted ones (filled circles) in (A) (Experiment #B8 in Richardson and Parr (1988), (B) Ripples and dunes (Experiment #E15 Flat bed in Elliott and Brooks (1997a)), and (C) Alternate bars (Experiment #E7 in Tonina and Buffington (2007)). 78

Figure 5.1: (A) the map of the Occoquan reservoir and its tributaries, in addition to the data measurement locations, the purple star is the Fairfax Water intake (ST01), while (B) represents Forty years of sodium concentration measurements at the Fairfax Water intake and the upstream stations (ST10, ST45), and the final reclaimed water discharged by UOSA (Bhide et al., 2021).....85

Figure 5.2: The considered events for the water flow data; A) event #1, B) event #2, and C) event #3. 87

Figure 5.3: The considered events for the salt concentration data; A) event#1, and B) event#2. 87

Figure 5.4:The considered events for the salt load data; A) event #1, B) event #2, C) event #3, D) event #4, and E) event #5.....89

Figure 5.5: A comparison between the predicted outflow by the geostatistical method and the observed outflow at station ST01 for events #1 (A), #2 (B), and #3 (C). 89

Figure 5.6: The results for the system response time for the outflow pulses for events #1 (A), #2 (B), and #3 (C). 90

Figure 5.7: A comparison between the predicted concentration by the geostatistical method and the observed concentration at the output station for event #1 (A) and event #2 (B).....91

Figure 5.8: The results for the system response time for concentration spikes for events #1 (A) and #2 (B).....91

Figure 5.9: A comparison between the predicted salt load by the geostatistical method and the observed load at the output station for events #1 (A), #2 (B), #3 (C), #4 (D), and #5 (E). 93

Figure 5.10: The results for the system response time for loads for events #1 (A), #2 (B), #3 (C), #4 (D), and #5 (E). 94

List of Tables

Table 2.1: The performed simulations (checkmarks) conducted in this study in different conditions of stream flow and groundwater flux. Q_{bf} and $Q_{avg}$are the bankfull and average stream flow, respectively.....8

Table 2.2: Hydraulic and Geometric Characteristics of the Maruia River (Berg, 1995) that are used in the present work to build the synthetic reach.....9

Table 2.3: Streamflow cases and bar submergence ratios considered in this study.....10

Table 2.4: Hyporheic flux ($q_h, m/s$), Hyporheic Area (A_h, m^2) and Hyporheic Flow ($Q_h, m^3/d$) in different streamflow cases (0.5 Q_{avg}, Q_{avg}, 2 Q_{avg}, 3 Q_{avg}, Q_{bf}), and different values of gaining and losing Conditions (q_{bot} is expressed as a fraction of the hyporheic flux in neutral condition, q_{h_n}). 19

Table 2.5: Hyporheic flux ($q_h, m/s$), hyporheic area (A_h) and hyporheic flow ($Q_h, m^3/d$) in isotropic and anisotropic conditions under neutral condition ($q_{bot} = 0$).....21

Table 2.6: Residence times at different probability values of the cumulative frequency distributions ($RTs_{90\%}$, $RTs_{80\%}$, $RTs_{50\%}$, $RTs_{20\%}$, $RTs_{10\%}$ and RTs_{mean}; in days) in different streamflow cases ($0.5Q_{avg}, Q_{avg}, 2Q_{avg}, 3Q_{avg}$ and Q_{bf}), and in different values of gaining and losing conditions (q_{bot} is expressed as a fraction of the hyporheic exchange flux in the neutral conditions, q_{h_n}). 25

Table 2.7: Residence times at different probability values of the cumulative frequency distributions ($RTs_{90\%}$, $RTs_{80\%}$, $RTs_{50\%}$, $RTs_{20\%}$, $RTs_{10\%}$ and RTs_{mean}; in days) in isotropic and anisotropic, and neutral conditions. 28

Table 2.8: Maximum hyporheic depth at different probability values of the cumulative frequency distributions ($Z_{90\%}$, $Z_{80\%}$, $Z_{50\%}$, $Z_{20\%}$, $Z_{10\%}$, and Z_{mean}; in meters) in different streamflow cases ($0.5Q_{avg}, Q_{avg}, 2Q_{avg}, 3Q_{avg}$ and Q_{bf}), and different values of gaining and losing conditions (q_{bot} is expressed as a fraction of the hyporheic exchange flux in the neutral conditions, q_{h_n}).....30

Table 2.9: Maximum hyporheic depth at different probability values of the cumulative frequency distributions ($Z_{90\%}$, $Z_{80\%}$, $Z_{50\%}$, $Z_{20\%}$, $Z_{10\%}$, and Z_{mean}; in meters) in isotropic and anisotropic and neutral conditions. 33

Table 2.10: Regression coefficients for Eq. (2.7) (Neutral Condition).....39

Table 2.11: Regression coefficients for Eq. (4.8) (Gaining/ Losing Conditions). 40

Table 3.1: A list of the adopted analytical distributions in this study with their associated pdf formulae and parameters. 48

Table 3.2: Embarras River properties used for normalizing the respiration and denitrification time scales. † Porosity was obtained from Figure 5 in Urumović and Urumović Sr (2014) by considering the referential grain size = D_m. ‡ The hydraulic conductivity was calculated with the Kozeny–Carman equation. 55

Table 4.1: The list of considered experiments in this study with their morphology types and initial conditions of solute concentration in the water column and. The initial conditions in these experiments differ by either introducing the solute tracer in the water column ($C_{w0} > 0$) or in the sediment ($C_{s0} > 0$). Experiment technique indicates wether the expreriment was conducted using a recirculating flume or a strirring tank. Some studies reported the temporal variation of solute flux out of the sedimentbed ($J(t)$), others reported either the temporal variation of solute concentration in the water column ($C_w(t)$) or in the sediment ($C_s(t)$). 65

Table 4.2: The list of dimensional predictive models for $D_{eff,0}$ and a, ranked based on BIC criteria. 72

Table 4.3: The list of dimensionless predictive models for $D_{eff,0}$ and a, ranked based on BIC criteria. 74

Table 5.1: A list of the considered events to estimate the transfer function for flow, load, and concentration.....86

Chapter 1
Introduction

1.1 Solute Exchange between Water Column and Sediment

The solute exchange between streams and their underlying sediment domain plays a paramount role in determining the river system ecology and environment. Many physical and biological processes in aquatic ecosystems depend on, or are strongly affected by, turbulent fluid motions at the sediment-water interface (SWI) (Franca & Brocchini, 2015; Grant et al., 2012). The shallow sediment adjacent and underneath the stream possess unique chemical and biological properties stemming from the mixing between groundwater and surface water (Hester & Gooseff, 2010). Its high potential for nutrients removal and pollutant attenuation has attracted the attention of many researchers (Galloway et al., 2019).

In literature, two main approaches were followed to study the characteristics of this biogeochemically active area. First, the physically based approach aims to reproduce the main physical transport processes, which typically include advection (e.g., Elliott & Brooks, 1997b), and sometimes diffusion and dispersion (e.g., Bardini et al., 2012). These exchange processes form a zone in the shallow sediment called the hyporheic zone (HZ) that possesses a wide range of spatial and temporal scales of transport (e.g., Boano et al., 2014). Second, the lumped approach (e.g., the diffuse approach, which lump all the physical transport processes at the sediment water interface (SWI) in a unique and simplified model (Grant et al., 2020a, 2020b). This later approach uses the so-called benthic biolayer that is a region of the hyporheic zone ranges from $2\ cm$ to $5\ cm$, where microbial biomass and nitrification and denitrification potential tend to be concentrated (Caruso et al., 2017; Knapp & Kelleher, 2020; Tomasek et al., 2019).

1.1.1 Hyporheic Exchange Characteristics

The hyporheic zone is defined as the sediment immediately beneath and adjacent to streams, rivers, and riverine estuaries where surface water and groundwater interact. It is a hotspot for physical, biological, and biogeochemical processes that control pollutant removal (Beaulieu et al., 2011; Grant et al., 2014), stream nitrogen cycling (Galloway et al., 2019), particle transport and mobilization (Stewardson et al., 2016), pathogen sequestration and mobilization (Grant et al., 2011), heat budgets (Sawyer et al., 2012;

White et al., 1987), oxygen consumption (Tonina et al., 2015), habitat quality (Baxter & Hauer, 2000; Wu, 2000) and stream health (Feminella & Walsh, 2005).

The movement of water into and out of the hyporheic zone, or "hyporheic exchange," occurs over a wide range of spatial (and temporal) scales, from > 10 km ($> 1\ year$) to $< 1\ m$ ($< 1\ hr$) (Boano et al., 2014; Gomez-Velez et al., 2014; Wörman et al., 2007). This $> 10^3$ range of temporal and spatial scales raises trade-offs —relative to residence times, reaction times, and exchange rates—that can influence the hyporheic zone's ability to process nutrients and other pollutants (Harvey et al., 2013). The hyporheic flow (Q_h) is hydrologically defined as the volume of stream water per unit of time, which flows through the subsurface domain, and it starts and terminates at the stream after a certain period of time (Hester & Gooseff, 2010). The hyporheic flux (q_h) is the corresponding flow per unit area through the streambed. It differs from groundwater flux because the former is exchanged back and forth across the sediment-water interface (SWI) at a relatively small scale, typically centimeters to tens of meters; in contrast, groundwater flow travels unidirectionally over much longer distances (see for example Boano et al., 2014 and citations therein).

1.1.2 Solute Transport at the Sediment Water Interface using a Diffusive description.

In streams, the hydrodynamic characteristics at the SWI dictate the transport of solutes between the interstitial fluid and the overlying flow (Grant & Marusic, 2011; Huettel et al., 2003). This solute transport through the SWI forms a zone called the benthic biolayer that is the most biogeochemically active in the river. This area is rich in nutrients and biogenic substances that support diverse microbial communities (Hester & Gooseff, 2010; Liu et al., 2021). There are many transport processes simultaneously active within this layer (e.g., advective pumping, dispersion, molecular and turbulent diffusion) (Grant et al., 2020a, 2020b). These many processes grouped together to be expressed as one quantity (effective diffusion) representing the overall transport process through the SWI (Grant et al., 2012; Grant et al., 2020a, 2020b; O'Connor & Harvey, 2008; Voermans et al., 2018).

The interfacial hydrodynamics at the SWI induces different exchange mechanisms. When the sediment has very low permeability, molecular diffusion is primarily responsible for the molecular transport process. For other sediment and overlying flow characteristics, other processes become the main drivers of solute transport. For more permeable sediment, dispersive mixing (Grant et al., 2020a), also called turbulent pumping (Boano et al., 2011; Higashino et al., 2009; Kim et al., 2020; Zhong et al., 2016) occurs when turbulent eddies generate pressure waves over the SWI and cause oscillating laminar flow at the interface (Grant et al., 2020a). For very permeable sediment, exchange is dominated by the turbulent

diffusion process, in which eddies penetrate the sediment and transfer energy and momentum through the SWI (Grant et al., 2020a; Kim et al., 2020; Reidenbach et al., 2010; Ren & Packman, 2004; Roche et al., 2018; Voermans et al., 2018). These two exchange processes (i.e., dispersive mixing and turbulent diffusion) can occur regardless of the streambed morphology. In addition, the presence of dunes further enhances exchange through bedform pumping, which determines advective exchange though downwelling and upwelling zones (e.g., Azizian et al., 2017; Cardenas et al., 2008; Elliott & Brooks, 1997a, 1997b). The 3-D geometry of alternate bars (i.e., pool-riffle sequences) induces a more complex mixing pattern, as large bedforms usually induce more mixing magnitude and depth (Hester et al., 2021). The induce hyporheic flow paths move longitudinally in the downstream direction and laterally in the transverse direction (Marzadri et al., 2010; Monofy & Boano, 2021; Tonina & Buffington, 2007; Trauth et al., 2013). Moreover, turnover exchange due to dune migration can play an important role in the exchange process through the entrapment and release of the interstitial fluid (Elliott & Brooks, 1997a). For all these processes, sediment properties like porosity and permeability influence the overall mixing (Grant et al., 2012; Herzog et al., 2018; Laube et al., 2018; Newcomer et al., 2016; Salehin et al., 2004).

1.2 Salt Load as a Conservative Solute in Freshwater

Increasing salinity in rivers is a worldwide problem that is observed in many regions around the world: North America (Kaushal et al., 2005; Kaushal, Likens, et al., 2018; Stets et al., 2020), South America (Kaushal et al., 2021), Asia (Kaushal et al., 2019, 2021), Africa (Kaushal et al., 2021), Europe (Kaushal et al., 2019; Schulz & Cañedo-Argüelles, 2019), and Australia (Kefford et al., 2003; Rengasamy, 2006; Williams, 2001). The freshwater salinity is caused by various sources in different locations but usually includes Na^+, Ca^{2+}, Mg^{2+}, K^+, Cl^- and ${SO_4}^{2-}$ as major ions (Kaushal et al., 2005). Increasing the concentration of these ions leads to the increase of freshwater salinity, that impacts the natural, social, and built environment, and this condition is known as the Freshwater Salinity Syndrome (FSS) (Kaushal et al., 2022).

Kaushal et al. (2022) hypothesized that there are four main factors (human activity, flow paths, geology, and climate) that control the progression and diversity of FSS, in addition to time as a fifth one. The human activities causing FSS are related to urbanization and land uses that release a variety of ions to the waterways (Kaushal et al., 2017; Kaushal, Gold, et al., 2018), e.g., road salts that release mainly Na^+ and Cl^- plus other ions with lower concentrations (e.g., Kaushal et al., 2005), water softeners (e.g., Bhide et al., 2021), fertilizers that are sources of K^+, Cl^- and ${SO_4}^{2-}$ (Kaushal et al., 2021; Kaushal, Gold, et al., 2018), agriculture lime (Kaushal, Gold, et al., 2018; Raymond et al., 2008), vegetation removal (Rengasamy, 2006), mining (Kaushal, Gold, et al., 2018; Meybeck & Helmer, 1989), urban wastewater (Bhide et al., 2021; Kaushal, Gold, et al., 2018), some household

products (Bhide et al., 2021; Tjandraatmadja et al., 2010), and resource extraction (Galella et al., 2021; Kaushal et al., 2021). Flow paths of water can transport solutes locally and regionally, as they can carry ions on timescales varying from minutes to decades from the source in a catchment to a stream (Hrachowitz et al., 2016; Kirchner et al., 2000). The effect of flow paths on FSS can be observed in groundwater pumping (Paul et al., 2019), saltwater intrusion into groundwater (Galella et al., 2021), and irrigation return flow (Bouzourra et al., 2015). Catchment geology is also a controlling factor of FSS, as exemplified by the interaction of acidic rain with soil lithology (Kaushal et al., 2022). In addition, climate can play a paramount role in altering the freshwater salinity; in semi-arid and Mediterranean climates, high temperatures cause high ion concentration because of evaporation and evapotranspiration (Marie & Vengosh, 2001; Salameh, 2001), and sea water rise (Kaushal et al., 2021; Kaushal, Gold, et al., 2018). FSS develops and progresses over time from a single pulse in a watershed to a long-term trend of high concentration (Kaushal et al., 2022). The previous mentioned factors can affect FSS at different timescales; climate and geology can initially induce FSS that can then be accelerated by human activities through flow paths, which can lead to more severe FSS conditions (Kaushal et al., 2022).

1.3 Thesis Outline

This thesis is organized in five chapters as follows:

Chapter 1: This chapter is an introduction about the general concepts discussed in this thesis. It includes a brief description of solute mass transport at SWI, as well as the definition of the hyporheic zone. In addition, an introduction about the conservative solute transport in the Occoquan reservoir.

Chapter 2: In this chapter, we present the effects of different streamflow, ambient groundwater, and sediment anisotropy on the hyporheic zone (HZ) characteristics in alternate bars. Solutes are advected in the shallow sediment due to different factors. Bed morphology is an important factor that triggers hyporheic exchange and delineates the HZ in the sediment bed and define its characteristics. Several simulations, using a sequentially coupled surface water-groundwater model of a synthetic river reach with fully developed alternate bars morphology, were performed. A predictive model was derived to predict the hyporheic flux, residence times, and hyporheic depths dependence on bar submergence, ambient groundwater, and sediment anisotropy.

Chapter 3: Differently from the previous chapter, in this one we focus on the hyporheic residence times (RTs) in dune-like bedforms. We evaluate the influence of dimensionless sediment depths of d_b^* and of dimensionless groundwater underflow u_b^* on the shape of the hyporheic residence times distributions (RTDs). Empirical RTDs were generated for a

range of combinations of d_b^* and u_b^* values, from numerical particle tracking simulations in which 10000 particles were released over a flat bed domain. These empirical RTDs were then fitted to different analytical distributions (specifically, to the Exponential, Gamma, Lognormal, and Fréchet distributions) to identify the best analytical representation of the RTDs.

Chapter 4: A diffusivity model was introduced to model the reactive and non-reactive solutes such as nutrients, and pollutants vertical transport across the SWI. These solutes transport vertically to the so called benthic biolayer in the shallow sediment. In this biogeochemically active layer, microorganisms catalyze a broad range of redox reactions that can work as a sink or source for nutrients. The vertical transport is due to exchange processes that are controlled by stream and sediment characteristics. In this chapter, we test the dependence of the transport parameters within the introduced diffusivity model on these characteristics. We perform a meta-analysis using previously published laboratory experiments with different streambed configurations that influence the physics of the exchange processes. Finally, we build robust and parsimonious predictive formulae that can predict the exchange parameters on the basis of the stream and sediment characteristics.

Chapter 5: We apply the geostatistical method to estimate the characteristic timescales of salt transport into the Occoquan reservoir in northern Virginia (USA) from its upstream tributaries. This method, formulated in the groundwater field, has been applied to identify contaminant sources in river pollution problems. The problem modeled here consists of recovering a contaminant source at a known location from a finite number of concentration measurements. The Occoquan reservoir is treated as an in input-output system, and the response times of water flow and salt transport are determined. The determination of the response time helps the authorities in the management and operation of the Occoquan reservoir and Fairfax water treatment plant.

Chapter 2
Hyporheic Zone Characteristics in Alternate Bars

2.1 Introduction.

The work presented in this chapter is derived from Monofy & Boano. (2021)

The geometry of alternate bars is more complex than other morphology types (e.g., ripples and dunes), as it induces 3-D patterns of hyporheic flow due to the hydraulic head variations in longitudinal and transverse directions on its morphology (Tonina & Buffington, 2007; Trauth et al., 2013). Many studies have been carried out on the HZ characteristics in 3-D gravel bars morphology. Laboratory experiments and 3-D modeling were conducted to investigate the effect of streamflow and bar amplitude variations on hyporheic exchange flow (Tonina & Buffington, 2007). Alluvium depth can also constrain the extent of the HZ (Tonina & Buffington, 2011). A predictive model was proposed by Marzadri et al. (2010) to estimate the hyporheic residence times (RT) dependence on bar submergence, hydraulic conductivity, and the slope of a stream reach. Additionally, the undermining effect of ambient groundwater on the HZ was analyzed by Trauth et al. (2013) for fully submerged bars.

Despite these many studies, the HZ characteristics in partially submerged bars have not been fully discovered yet. The importance of bars with low submergence lies in their common occurrence during low stream flow periods, e.g., low flow mountain stream during the period of spawning activity of many salmonids (Tonina & Buffington, 2007). Even though the ambient groundwater has a considerable effect on HZ characteristics (Trauth et al., 2013), to our knowledge, it has been less studied for partially submerged bars. Besides, even though sediment anisotropy is very common in nature, no study has deeply disentangled its effect on the HZ characteristics. Here we carried out an extensive modeling study to assess the effect of (a) bar submergence due to different stream flows, (b) ambient groundwater, and (c) sediment anisotropy on the HZ characteristics. From our results, we provided a new set of predictive formulae to account for the variations in HZ characteristics depending on the above mentioned parameters.

2.2 Methodology

In this work we performed 45 numerical simulations to represent different combinations between streamflow (Q_{surf}) and groundwater flux (q_{bot}) (Table 2.1). Out of these simulations, 2 simulations were dedicated to the isotropic conditions ($q_{bot} = 0$). These different combinations between the values of Q_{surf} and q_{bot} were chosen to help understand their effect on the HZ characteristics in alternate bars. For this purpose, a sequentially coupled surface water-groundwater model was built. In our model, it is considered that flow in the surface domain imposes the boundary conditions that drive flow in the subsurface domain, while the latter provides no feedback on surface flow.

Table 2.1: The performed simulations (checkmarks) conducted in this study in different conditions of stream flow and groundwater flux. Q_{bf} and Q_{avg} are the bankfull and average stream flow, respectively.

Groundwater fluxes	**Stream flows**						
	Isotropic conductivity		Anisotropic conductivity				
q_{bot}	$0.5Q_{avg}$	Q_{bf}	$0.5Q_{avg}$	Q_{avg}	$2Q_{avg}$	$3Q_{avg}$	Q_{bf}
$q_{bot} = 0$ (neutral)	✓	✓	✓	✓	✓	✓	✓
$q_{bot} = +0.5\ q_{h_n}$	-	-	-	✓	-	-	✓
$q_{bot} = -0.5\ q_{h_n}$	-	-	-	✓	-	-	✓
$q_{bot} = +\ q_{h_n}$	-	-	✓	✓	✓	✓	✓
$q_{bot} = -\ q_{h_n}$	-	-	✓	✓	✓	✓	✓
$q_{bot} = +1.5\ q_{h_n}$	-	-	-	✓	-	-	✓
$q_{bot} = -1.5\ q_{h_n}$	-	-	-	✓	-	-	✓
$q_{bot} = +2\ q_{h_n}$	-	-	✓	✓	✓	✓	✓
$q_{bot} = -2\ q_{h_n}$	-	-	✓	✓	✓	✓	✓
$q_{bot} = +3\ q_{h_n}$	-	-	✓	✓	✓	✓	✓
$q_{bot} = -3\ q_{h_n}$	-	-	✓	✓	✓	✓	✓

A synthetic stream reach, whose dimensions and characteristics are the same as the Maruia River in New Zealand (reported by Berg (1995) (Table 2.2)), was used in our simulations. However, it is important to highlight that this study does not aim to analyze the hyporheic exchange in the Maruia River. Instead, its geometric and hydraulic properties were used as an example of a realistic stream reach with alternate bars. The river roughness coefficient was calculated with the Manning equation for wide channels due to its large width (w) compared to the channel depth (d), as $w/d = 64$. The median of sediment particles within the riverbed ($D_{50} = 36$ mm) is typical of gravels (Julien, 2002), as alternate bars usually form in gravel bed rivers (Da Silva & Yalin, 2017). Moreover, the flow data exhibit a considerable difference between the average and bankfull streamflow discharge

($Q_{bf} \approx 4Q_{avg}$), hence providing a sufficiently wide range to emphasize the differences in the pertinent HZ characteristics among the different submergence ratios.

Table 2.2: Hydraulic and Geometric Characteristics of the Maruia River (Berg, 1995) that are used in the present work to build the synthetic reach.

Stream reach characteristics	
Bankfull Width (w_{bf})	$87.4\ m$
Bankfull Depth (d_{bf})	$1.36\ m$
Sediment size (d_g)	$36\ mm$
Stream reach slope (S_0)	$3.49\ m/km$
Average discharge (Q_{avg})	$55.8\ m^3/s$
Bankfull discharge (Q_{bf})	$214\ m^3/s$
Sinuosity (p)	1.09
Manning coefficient (n)	0.04
Alternate bars*	
Wavelength (λ_{ab})	$271.5\ m$
Amplitude (Δ_{ab})	$1.25\ m$

* The dimensions of the alternate bars were calculated with the empirical equations of Da Silva & Yalin (2017).

2.2.1 Alternate Bars Geometry.

An idealized rectangular stream reach was built by implementing the geometric data (w, d) of the Maruia river. Alternate bar morphology was imposed on the constructed reach. To estimate the bar dimensions (wavelength λ_{ab}, and amplitude Δ_{ab}), the empirical set of equations recently developed by Da Silva & Yalin (2017) for free-formed one-row bars in wide and straight channels was adopted in our work. The existing morphology is assumed to be in equilibrium with the bankfull flow. Therefore, the calculated single bar wavelength is $\lambda_{ab} = 271.5\,m$ and the amplitude $\Delta_{ab} = 1.25\,m$. Subsequently, gradually varying streambed with respect to the calculated alternate bars dimensions was defined by Eq. (2.1) (Trauth et al., 2013):

$$E_{ab}(x,y) = \Delta_{ab} \sin\left(\frac{2\pi x}{\lambda_{ab}}\right) cos\left(\frac{\pi y}{w_{bf}}\right) \quad (2.1)$$

where E_{ab} is the streambed elevation, x is the longitudinal direction (streamflow direction), y is the transverse direction, and w_{bf} is the reach width under bankfull streamflow. According to Eq. (2.1) , a sequence of peaks and troughs was present along each bank of the stream reach (the gray surface in Figure 2.1). The aspect ratio is $\lambda_{ab}/w = 3:1$, which is within the range reported in literature for free-formed alternate bars ($\approx 3-7$) (Keller, 1972; Leopold & Wolman, 1957). Therefore, this stream reach can be representative of a more common type of alternate bars.

Finally, to avoid the effect of upstream and downstream boundary conditions, a sequence of seven alternate bars was developed to define the model domain extent using Eq. (2.1). Only the middle bar was considered for the hyporheic exchange analysis, similar to the approach followed by Trauth et al. (2013). The smoothly varying bed elevation was built using a fine spatial resolution ($\Delta x = \Delta y = 0.1\, m$). Afterward, it was used as a bottom boundary for the 2-D domain to calculate the surface water elevation (SWE) as well as a top boundary for the subsurface domain.

2.2.2 Surface Water Modeling.

A 2-D model was built using the HEC-RAS 5.0.4 package to simulate different Q_{surf} applied on the constructed stream reach. HEC-RAS 2-D calculates SWE on a defined grid mesh in a x-y plane. In the synthetic stream reach, the vertical length scale is much smaller than the horizontal length scale with a smoothly varying streambed. Therefore, the hydrostatic pressure was assumed to be a good surrogate for the total hydraulic pressure at the streambed (Tonina & Buffington, 2007).

A structured grid mesh of square cells ($0.35\, m\ x\ 0.35\, m$) was applied on the seven bars with a maximum cell size of $0.25\, m^2$, the minimum size of $0.09\, m^2$ and the average size of $0.12\, m^2$. The upstream and downstream boundary conditions were imposed at sections of flat bed to have a streamflow value that is uniformly distributed on the entrance and exit of the calculation domain. At the upstream boundary, five steady streamflow values ($0.5\, Q_{avg}, Q_{avg}, 2Q_{avg}, 3Q_{avg}\ and\ Q_{bf}$ (Table 2.3)) were imposed.

Table 2.3: Streamflow cases and bar submergence ratios considered in this study.

Discharge ratio	***Discharge value (m^3/s)***	***Bar submergence ratio (%) ****	***Bar submerged area (m^2)***
$0.5Q_{avg}$	27.9	65.74	18,432
Q_{avg}	55.8	74.69	19,866
$2Q_{avg}$	111.6	87.63	21,784
$3Q_{avg}$	167.4	97.84	23,060
Q_{bf}	214	105.16	23,888

* The bar submergence ratio associated with each streamflow case is calculated by dividing average flow depth (d) by double bar amplitude ($2\Delta_{ab}$).

The "Normal Depth" boundary condition with the average stream reach slope value was imposed at the downstream boundary. Impermeable non-erodible bed and banks that are commonly used in such simulations (Tonina & Buffington, 2009; Trauth et al., 2013) were assumed in the surface water model. This assumption is common because the hyporheic exchange flow rate (Q_h) is usually ranging from 0.1% to 10% of the river flow (Thibodeaux & Boyle, 1987), and hence its influence on Q_{surf} is negligible.

HEC-RAS 2-D uses a time-stepping approach to solve the 2-D flows until steady state conditions are attained. We started with the dry bed condition with a dynamic wave and set the time step to be such that the Courant number will be below the unity in all cases. The "Diffusion Wave" equations approach was selected over the "Full Momentum" one due to its lower computational cost (USACE, 2016). The "Full Momentum" equations set was activated on one of the streamflow discharges cases (Q_{bf}), and the resulting difference in SWE between the two methods was less than $0.012\ m$. Therefore, the "Diffusion Wave" approach provided very reliable results for the surface water simulations. Finally, a 2-D map of SWE was exported for each Q_{surf} case (section 2.3.1) to be applied afterward as a top boundary condition for the groundwater model.

2.2.3 Groundwater Modeling.

The MODFLOW Flex 2015.1 package was used to build the groundwater numerical model. MODFLOW, that is based on the finite-difference method, is extensively used for addressing flow problems of surface water-groundwater interaction systems (McDonald & Harbaugh, 1988). The model domain included, in length, the pre-built sequence of seven bars and, in-depth, five layers with a deep bottom ($\approx 200m > 2w_{bf}$), which was designed to be deep enough to allow the hyporheic flow paths to develop vertically without any restrictions (Tonina & Buffington, 2011). At first, a finite-difference grid mesh was created under all the streamflow cases to discretize the seven alternate bars domain. The mesh was constructed with 800 cells in the longitudinal direction (x), 250 in the transverse direction (y), and 5 layers in-depth direction. Therefore, each cell dimensions in $x-y$ plane was $2.38\ m\ x\ 0.35\ m$. This cell size was chosen as it limited convergence time for all simulations; finer meshes with square cells ($0.7\ x\ 0.7\ m^2$ and $0.35\ x\ 0.35\ m^2$) were tried in Q_{bf} case, resulting in an error of less than 0.2% for q_h compared to the chosen mesh size. Finally, in z direction, the first two layers were thinner since they were used to calculate the hyporheic exchange flux (vertical Darcy flux) with Eq. (2.1). Therefore, their thicknesses were chosen to be $1\ m$, except for bankfull flow ($0.5\ m$) (thinner thicknesses were tried for lower stream flows, but model convergence was hampered). The third and fourth layers had the same depth of $50\ m$. Finally, the deepest layer had a thickness of $100\ m$.

The head in each cell of the first layer is the surface water hydraulic head imposed as a "Dirichlet" boundary condition. MODFLOW-2005 flow engine was employed to solve the subsurface water flow field in the sediment. The hyporheic exchange flux (q_h) was calculated using Darcy's law (Wu et al., 2018):

$$q_h = -K_v\left(\frac{\Delta H}{\Delta z}\right) \quad (2.2)$$

where ΔH is the head difference between the first two layers of the domain and Δz is the elevation difference between the same layers. Homogeneous anisotropic conductivity was applied over the model domain, where the horizontal value ($K_x = K_y = K_h$) is an order of magnitude higher than the vertical conductivity ($K_z = K_v$). The first four layers were assumed to share the same characteristics of conductivity ($K_h = 10^{-3}\ m/s$, $K_v = 10^{-4}\ m/s$ (Domenico & Schwartz, 1998)), while the deepest layer was assumed to be more compacted (Nelson, 1994) ($K_h = 10^{-4}\ m/s, K_v = 10^{-5}\ m/s$). However, this deep and less conductive layer eventually did not affect the results of the HZ analysis, as the HZ extent is only within the first three layers (Section 2.3). Two homogeneous isotropic simulations ($K_h = K_v = 10^{-3}\ m/s$ for the whole domain) were added as reference cases for Q_{avg} and Q_{bf} to unravel the effect of the sediment anisotropy.

On the upstream and downstream boundaries as well as the domain sides, "Neumann" boundary conditions were applied with no-flux. On the bottom boundary, no ambient groundwater flux ($q_{bot} = 0$; neutral conditions) was assigned in the two isotropic simulations. However, for 43 anisotropic ones, a specified flux value was imposed depending on the ambient groundwater conditions (neutral, gaining, or losing).

In neutral conditions, the no flux boundary condition was applied to the bottom boundary ($q_{bot} = 0$). To represent gaining and losing conditions, positive and negative flux values, respectively, were imposed uniformly on the domain bottom (see Table 2.1). The values of groundwater flux (q_{bot}) were $[\pm 1; \pm 2; \pm 3] \times\ q_{h_n}$, where q_{h_n} is the resulted value of q_h in neutral conditions (obtained after carrying out a simulation with no flux at the bottom layer), whereas positive and negative signs refer to gaining and losing conditions, respectively. Under Q_{avg} and Q_{bf} cases, 4 more simulation steps ($[\pm 0.5; \pm 1.5] \times\ q_{h_n}$) were added to have more refined results under these streamflow cases.

Then, to analyze the characteristics of the hyporheic zone, a particle tracking analysis was performed using MODPATH software with a one-day time step. As proved later by the results, this time step was able to track the hyporheic flow paths with sufficient resolution. Particles were located with $1\ m$ of spacing on $x - y$ plane on the middle bar. Due to the variations in the bar submerged area that corresponds to different streamflow, different particle numbers were injected into the subsurface domain (see bar submerged area in Table 2.3).

To extract only the hyporheic exchange flow paths, the forward particle tracking option was activated in neutral and gaining conditions to force the particles to move in the same direction of the hyporheic flux. Conversely, the backward particle tracking was employed

in losing conditions. Consequently, in all cases, the hyporheic flow paths, which start and end at the streambed, were recognized and separated from the groundwater flow paths. Finally, the aforementioned linked model was run to obtain the HZ characteristics under different Q_{surf} and ambient groundwater conditions. The hyporheic flow paths were exported with the associated values of pressure heads at the top two layers, travel times, and depths data. The flow path flux (q_f), total residence times (RTs), and maximum hyporheic depths (Z) were assigned to each corresponding flow path. q_f for each flow path was calculated by applying Eq. (2.2) to the resulting head difference between the first two layers of the subsurface domain and assigning the resulting value to its corresponding flow path. For all the cases shown in Table 2.1, q_h was calculated by averaging q_f for all flow paths, and flux distribution maps of upwelling and downwelling fluxes with corresponding areas (later denoted as hyporheic exchange area, A_h) were produced. Q_h ($A_h \times q_h$) is here defined as the water volume per unit time that infiltrates into the groundwater aquifer and exits back to the surface water. RTs values of the exported flow paths were determined by the value of the last step on each path when its carried particle reenters the surface water domain. Z of each flow path was calculated as the difference between the streambed elevation (the mean elevation of a flow path starting and ending points) and the elevation of the deepest point reached. The flux-weighted averaging method was used to construct the cumulative RTDs and the maximum depths cumulative distribution ($Z - CD$) of the hyporheic flow paths.

2.2.4 Predictive Model Derivation.

- ***Data Collection***

A total of 41 out of 45 simulations were used to build the regression model, as the remaining 4 (gaining and losing at $q_{bot} = 3q_h$ for streamflow discharges of 0.5 Q_{avg} and Q_{bf}) were excluded because the hyporheic zone disappeared (Tables 2.4, 2.6 and 2.8). The simulations were divided into two groups: a first one is in neutral conditions ($q_{bot} = 0$) containing 7 simulations (corresponding to 5 different Q_{surf}; 5 simulations with homogeneous anisotropic, and 2 simulations with homogeneous isotropic conductivity), and a second one combining gaining and losing conditions ($q_{bot} \neq 0$) with 34 simulations in homogeneous anisotropic conditions.

- ***Multiple Linear Regression***

Multiple Linear Regression (MLR) analysis was implemented on the set of simulations, to build a set of predictive equations for q_h, and specific quantiles of residence times and hyporheic maximum depths ($RTs_{i\%}$, and $Z_{i\%}$, respectively, where $i = 10, 20, 50, 80$ and 90). Therefore, these quantities were included in the model as dependent variables. On the

other hand, the independent variables in the data group for the neutral conditions were average surface water depth (d) and velocity (V), and the horizontal and vertical conductivities (K_h and K_v, respectively). While for the gaining and losing data group, K_h and K_v were constant. Therefore, they were removed, and the included independent variables were d, V and q_{bot}. d was calculated for each Q_{surf} as the average water depth on the middle bar resulted from the surface water modeling (see sections 2.2.2 for method and 2.3.1 for results)

- ***Dimensionless Variables***

Dimensionless groups of the independent variables (d, V, K_h, K_v and q_{bot}) were created. For the neutral conditions, the independent variables can be used to compose two dimensionless quantities. First, the Reynolds number ($R_e = {Vd}/{\nu}$, where $\nu = 10^{-6}\, m^2$ is the water kinematic viscosity) that represents the streamflow regime, and K_v/K_h that denotes the sediment anisotropy. As in the gaining and losing conditions, simulations were performed in a single anisotropic condition, K_v/K_h is constant in the combined gaining and losing data group. However, another dimensionless variable ($|q_{bot}/V|$) was added to account for the effect of groundwater flux, in absolute value, on the HZ characteristics.

3-D dependent variables were also defined as q_h/V, $\mathrm{RTs}_{i\%}K_v/d$, and $Z_{i\%}/d$. This normalization is similar to the one employed by Huang and Chui (2018) work except for $\mathrm{RTs}_{i\%}$, in which V is used instead of K_v. Using K_v in the present work to normalize $\mathrm{RTs}_{i\%}$ resulted in a more robust model which fit the simulations results better than using V (see Section 2.3 for model robustness criteria).

- ***Model Equations and Evaluation***

The relationship between the dimensionless dependent and independent variables can be summarized as follows:

$$F^{neutral} = f\left(R_e, \frac{K_v}{K_h}\right) \qquad (2.3)$$

$$F^{gain/los} = f\left(R_e, \left|\frac{q_{bot}}{V}\right|\right) \qquad (2.4)$$

where F represents the dimensionless dependent variables, $neutral$ and $gain/los$ superscripts refer to the neutral data group and the combined gaining and losing data group, respectively.

A power law form was assumed for function $f()$ in Eqs. (2.3) and (2.4) which, after log-transformation, takes on the following linear forms:

$$\log F^{neutra} = \log a + b \log R_e + c \log \frac{K_v}{K_h} \quad (2.5)$$

$$\log F^{Gain/los} = \log m + n \log R_e + g \log \left| \frac{q_{bot}}{V} \right| \quad (2.6)$$

MLR was performed on the linear forms (Eqs. (2.5) and (2.6)) to estimate the regression coefficients (a, b, c, m, n and g). Various model robustness criteria were used for model evaluation; a better model has a higher the coefficient of determination (R^2), lower Root Mean Square Error ($RMSE$), and lower corrected Akaike Information Criterion (AIC_c) value, which accounts for the trade-off between model complexity and goodness of fitting (Akaike, 1974).

2.3 Results and Discussion.

2.3.1 Hydraulic Head Distribution on Streambed.

2-D spatial SWE maps (Figure 2.1) were exported for each Q_{surf} and bar submergence ratio (Table 2.3) from HEC-RAS (section 2.2.2). The flow is subcritical in all cases; the Froude number is lower than 0.9 at any point in the domain. The longitudinal head variation is due to both the stream reach slope and the morphology features. Also, the sequence of pools and riffles that forms the alternate bar induces a lateral variation of the head distribution where the head is higher on the upstream side of the riffle and dissipates gradually through the lee side of the riffle within the subsequent pool (Figure 2.1). Increasing Q_{surf} as well as decreasing the bar amplitude undermine the lateral head variations. This behavior is due to less horizontal flow displacements (Tonina & Buffington, 2007), as the hydrostatic pressure is dominant compared to the hydrodynamic effect of the morphology pattern as SWE rises (compare pressure head distributions of different Q_{surf} in Figure 2.1).

At lower Q_{surf}, a considerable head variation is evident in the longitudinal and transverse directions because the bed topography has more influence on the streamflow at lower submergence ratios. The instability zones (hydraulic jumps and surface waves) are assumed to be absent in the current analysis because of the very smooth variation in streambed elevation with mild-slope bar ($\Delta_{ab}/\lambda_{ab} \approx 0.004$) and the low Froude number within the surface domain.

2.3.2 Hyporheic Flow and Area.

The value of the hyporheic flux determines the amount of solutes enters to the HZ, which is necessary to fuel the reactions within this biogeochemically active zone (Bardini et al., 2012). Therefore, it is important to be able to quantify the hyporheic flux.

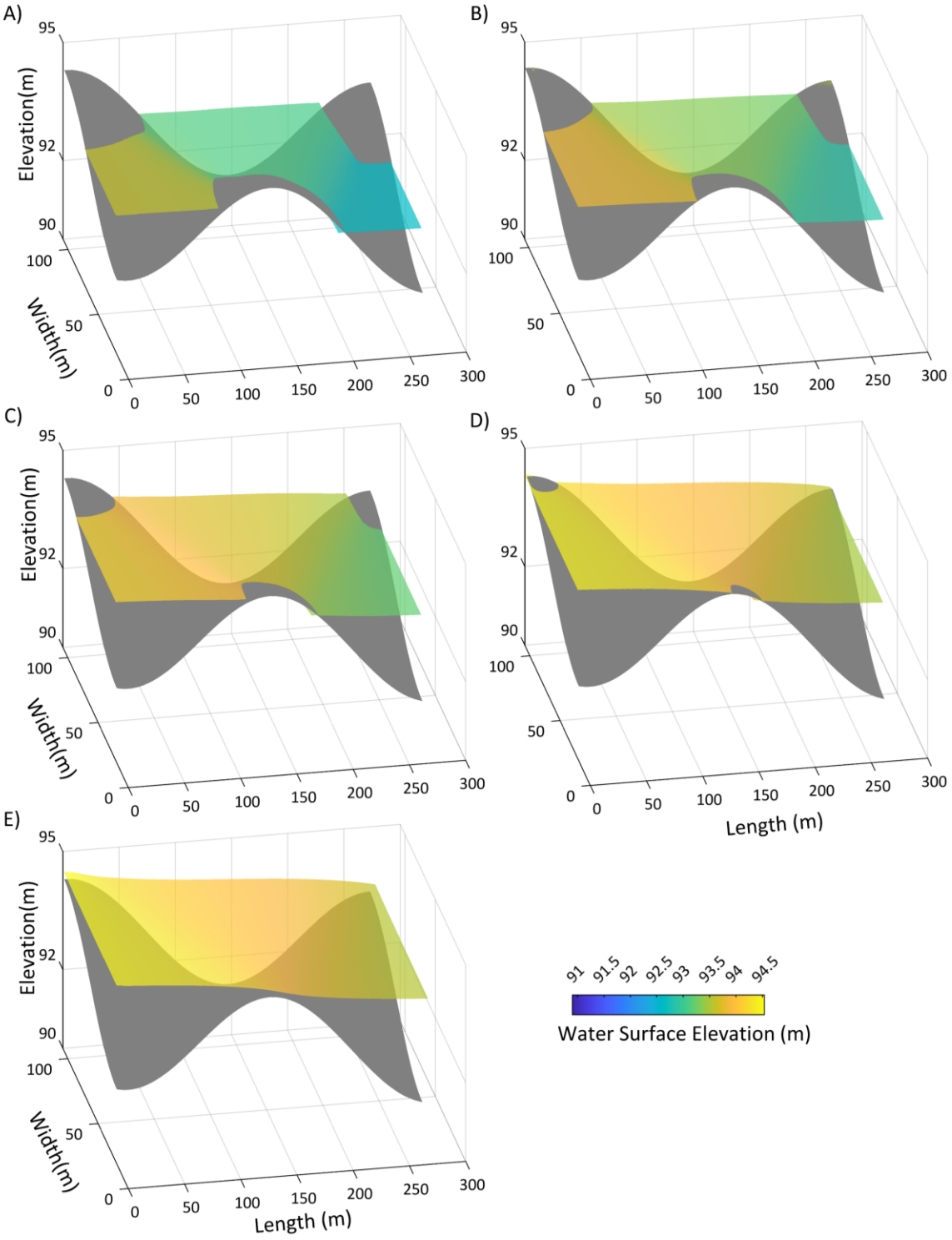

Figure 2.1: Water surface elevation for different Q_{surf} cases ((A) $0.5Q_{avg}$, (B) Q_{avg}, (C) $2Q_{avg}$, (D) $3Q_{avg}$, (E) Q_{bf}) and bar submergence. The gray surface represents the streambed elevation of the middle alternate bar.

Similar to the case of large amplitude in Tonina & Buffington (2011) study (partially submerged bar), a decrease in q_h is observed when increasing Q_{surf} (Table 2.4 and Figure 2.2). This is caused by an overall decrease in head gradient, due to lower influence of the morphological feature, at higher Q_{surf}. Despite the increase in A_h, as a larger portion of the alternate bar is submerged (Table 2.3), Q_h plummets because of the significant decrease in q_h (Table 2.4 and Figure 2.2).

Besides the hydraulic head gradients along the streambed, the hyporheic flow field is also influenced by vertical head gradients that are induced by q_{bot}. In agreement with Trauth et al. (2013), the imposed gaining and losing fluxes decrease Q_h values (Figure 2.3) and significantly shrink A_h in all streamflow cases (Figure 2.2 for Q_{avg} and Q_{bf}). Nevertheless, the shrinkage rate is similar between all streamflow cases (Table 2.4). This decrease is due to either the loss of some flow paths within the subsurface domain to the groundwater flow, or hindering of some surface particles from entering the subsurface domain at SWI. In other words, in losing conditions, some particles (flow paths) enter the subsurface domain without coming back again to the surface water due to the relatively strong vertical negative gradient caused by the assigned negative flux on the domain bottom. On the other hand, in gaining conditions, they are hampered from entering the subsurface domain, as the streambed pressure gradient is overcome by the upward vertical gradient that is induced by the upwelling q_{bot}. At very strong q_{bot}, the hyporheic zone disappears under the cases of very low streamflow (0.5 Q_{avg}) and bank full streamflow (Q_{bf}) due to the large magnitude of q_{bot}, that is proportional to the value of q_h in neutral conditions, compared to the q_h induced by the head variation of the surface water.

Peculiarly, there are some discrepancies in Q_h values and behavior between losing and gaining conditions. It can be explained by the differences between the spatial extent of infiltrating cells (Figure 9 in Trauth et al. (2013)), as different cells are activated in each streamflow case. In partially submerged bars with low Q_{surf} (0.5 Q_{avg}, Q_{avg}, and 2 Q_{avg}), Q_h is more hampered by q_{bot} in gaining condition than in the losing one. Contrarily, and in agreement with fully submerged bars in Trauth et al. (2013), for 3 Q_{avg} and Q_{bf} , in general, Q_h is slightly higher in gaining than in losing conditions. One possible explanation of this behavior is discussed by Tonina & Buffington (2007), who stated that the strength of the pressure gradient is not always decreasing with higher submergence. Instead, at a certain point, it can increase again, which implies a change in the hyporheic exchange mechanism. Also, in partially submerged bars, the existence of dry cells around the bars peaks could contribute to these discrepancies, unlike the case of fully submerged bars.

The sediment properties, especially hydraulic conductivity, are key parameters in determining the HZ characteristics. In gravel sediments, q_h is strongly affected by the vertical hydraulic conductivity (Glose et al., 2019). In other words, increasing the vertical

conductivity from $10^{-4}\,m/s$ to $10^{-3}\,m/s$ in the isotropic conditions decreases the sediment resistance to the flow paths penetration into the streambed. Therefore, q_h increases by almost the same order of magnitude as K_z, while A_h is slightly lower. This decrease in A_h could not compensate for the increase in q_h, thus resulting in higher values of Q_h in isotropic conditions (Table 2.5).

Table 2.4: Hyporheic flux ($q_h, m/s$), Hyporheic Area (A_h, m^2) and Hyporheic Flow ($Q_h, m^3/d$) in different streamflow cases (0.5 Q_{avg}, Q_{avg}, 2 Q_{avg}, 3 Q_{avg}, Q_{bf}), and different values of gaining and losing Conditions (q_{bot} is expressed as a fraction of the hyporheic flux in neutral condition, q_{h_n}).

Groundwater fluxes	$0.5\ Q_{avg}$			Q_{avg}			$2\ Q_{avg}$			$3\ Q_{avg}$			Q_{bf}		
	q_h $10^{-7}\ m$	A_h m^2	Q_h m^3/d	q_h $10^{-7}\ m$	A_h m^2	Q_h m^3/d	q_h $10^{-7}\ m$	A_h m^2	Q_h m^3/d	q_h $10^{-7}\ m$	A_h m^2	Q_h m^3/d	q_h $10^{-7}\ m$	A_h m^2	Q_h m^3/d
$q_{bot} = 0$ *(neutral)*	5.58	9070	437	4.71	9838	400.2	3.4	10892	319.6	2.76	11530	275	1.78	11944	183.8
$q_{bot} = +0.5\ q_{h_n}$				3.49	7076.2	213.1							1.55	8173	109.8
$q_{bot} = -0.5\ q_{h_n}$				4.26	6679	246							1.46	8319	105.1
$q_{bot} = +\ q_{h_n}$	3.12	3400	91.5	2.97	4913	126.1	2.47	5470	116.6	2.11	5718	104.2	1.17	5364	54.1
$q_{bot} = -\ q_{h_n}$	4.59	3700	146.6	3.36	4584	133.2	2.34	6268	126.7	1.83	6269	99.3	1.16	5267	53
$q_{bot} = +1.5\ q_{h_n}$				2.92	2370	59.8							8.07	3081	21.5
$q_{bot} = -1.5\ q_{h_n}$				2.97	3583	92							8.31	2959	21.2
$q_{bot} = +2\ q_{h_n}$	2.97	380	9.8	3.38	1053	30.7	2.83	1849	45.2	2.06	1904	33.8	6.01	1939	10.1
$q_{bot} = -2\ q_{h_n}$	3.96	496	16.9	3.01	1418	36.9	3.03	1766	46.2	1.68	1836	26.7	6.49	1991	11.2
$q_{bot} = +3\ q_{h_n}$	0	0	0	3.44	237	7	3.22	467	13	2.59	553	12.4	0	0	0
$q_{bot} = -3\ q_{h_n}$	0	0	0	5.03	272	11.8	6.06	280	14.7	2.45	394	8.3	0	0	0

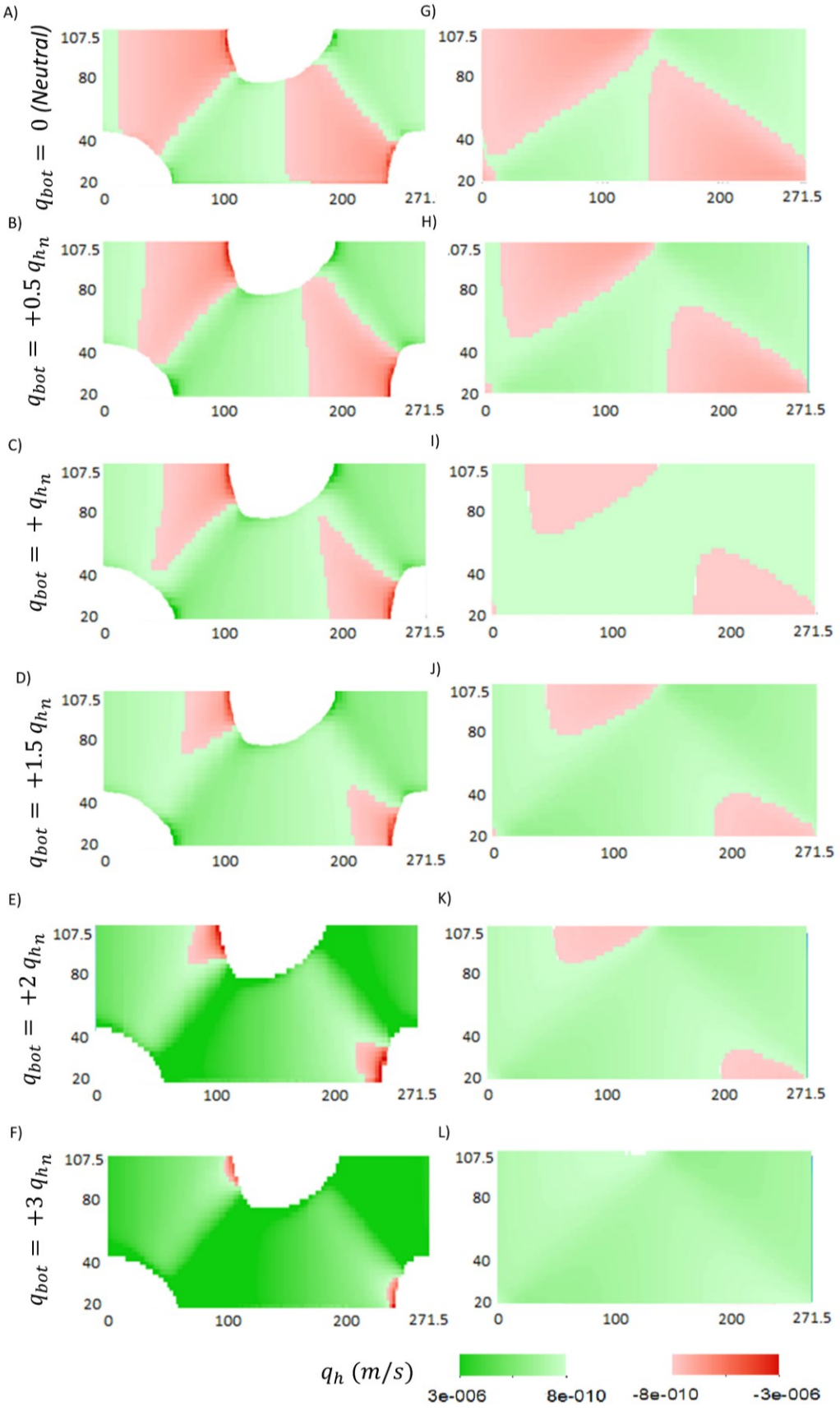
A)
G)
$q_{bot} = 0$ (Neutral)
B)
H)
$q_{bot} = +0.5\ q_{h_n}$
C)
I)
$q_{bot} = +\ q_{h_n}$
D)
J)
$q_{bot} = +1.5\ q_{h_n}$
E)
K)
$q_{bot} = +2\ q_{h_n}$
F)
L)
$q_{bot} = +3\ q_{h_n}$
107.5
80
40
20
0
100
200
271.5
$q_h\ (m/s)$
3e-006
8e-010
-8e-010
-3e-006

Figure 2.2: Hyporheic flux rate ($q_h, m/s$) spatial distribution over the middle bar in Q_{avg} (left column; A–F) and Q_{bf} (right column; G–L) under different ambient groundwater flux (q_{bot}) in anisotropic conditions. The red areas denote downwelling (losing) areas while the green ones indicate the upwelling (gaining) zones. The numbers in each panel that are written on the horizontal and vertical axes represent the streamwise and spanwise distances (in meters), respectively.

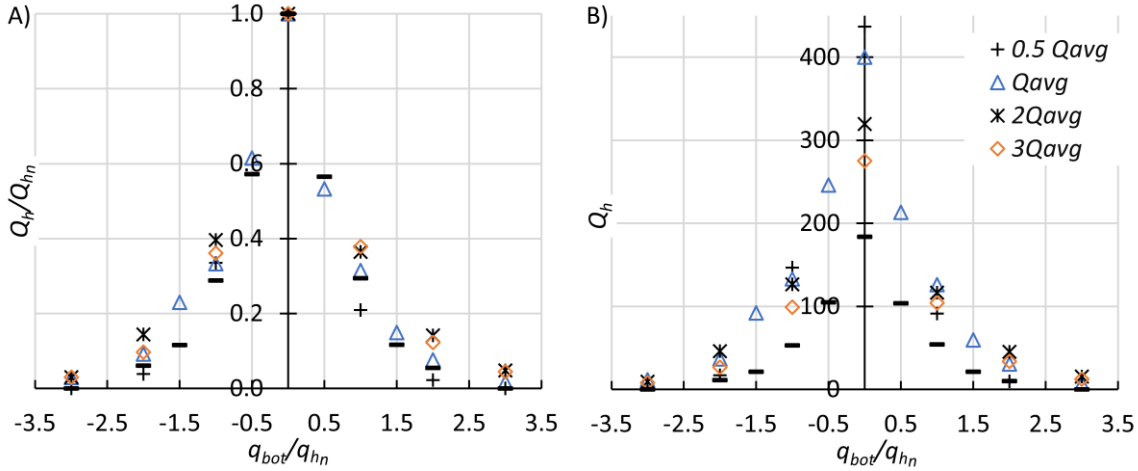

Figure 2.3: (A) Normalized hyporheic exchange flow (Q_h/Q_{h_n}) and (B) absolute hyporheic exchange flow (Q_h) values, in the anisotropic conditions. q_{bot}/q_{h_n} on the horizontal axes represents gaining (positive sign) and losing (negative sign) conditions, where q_{bot} is the value of imposed ambient groundwater. Q_{h_n} and $q_{h_n}$are the hyporheic flow and flux, respectively, in the neutral condition.

Table 2.5: Hyporheic flux ($q_h, m/s$), hyporheic area (A_h) and hyporheic flow ($Q_h, m^3/d$) in isotropic and anisotropic conditions under neutral condition ($q_{bot} = 0$).

	Isotropic condition			***Anisotropic condition***		
Stream Flow	q_h $10^{-7}\ m$	A_h m^2	Q_h m^3/d	q_h $10^{-7}\ m$	A_h m^2	Q_h m^3/d
Q_{avg}	24.9	9605	2066.5	4.71	9838	400.2
Q_{bf}	11.5	11256	1114.6	1.78	11944	183.8

2.3.3 Hyporheic Residence Times.

The longitudinal and lateral flow paths within the HZ are divided into shallow and deep flow paths. This is evident in Figure 2.4A and B, where the group of deep flow paths (red lines) moves longitudinally, while the group of shallow flow paths (blue lines) moves quasi-laterally. These flow paths infiltrate through the downwelling zones and exfiltrate

back to the stream through the upwelling zones (see the downwelling and upwelling zones in Figure 2.2A and G for neutral conditions). The deep flow paths travel relatively deep under the bars as the particles flow into the upstream face of the alternate bar and move longitudinally for a distance of similar magnitude to the bar wavelength λ_{ab} to exfiltrate at the downstream bar face (red lines in Figure 2.4A and B). On the other hand, the shallow flow paths travel quasi-laterally through the pool-riffle sequences. The cumulative RTDs for these flow paths is shown in Figure 2.4C for partially submerged bar under Q_{avg} and in Figure 2.4C for fully submerged bar under Q_{bf}. The blue part of the distribution represents the shallow flow paths while the red one represents the deep one. Evidently, slightly less portion of the flow paths infiltrate laterally in case of fully submerged bar (Figure 2.2D) compared to the partially submerged one (Figure 2.2C). This distinction between the two types of flow paths present within the hyporheic zone creates a bimodal cumulative RTDs, which is demonstrated by the double-S shape of the cumulative RTDs (Figure 2.4C and D), and it is more obvious in case of partially submerged bar (Figure 2.4C). This bimodality was verified by applying HDS_w/BC (Kang & Noh, 2019) and HDS (Hartigan & Hartigan, 1985) tests, as they are very accurate in determining the existence of multimodality (Freeman & Dale, 2013; Kang & Noh, 2019).

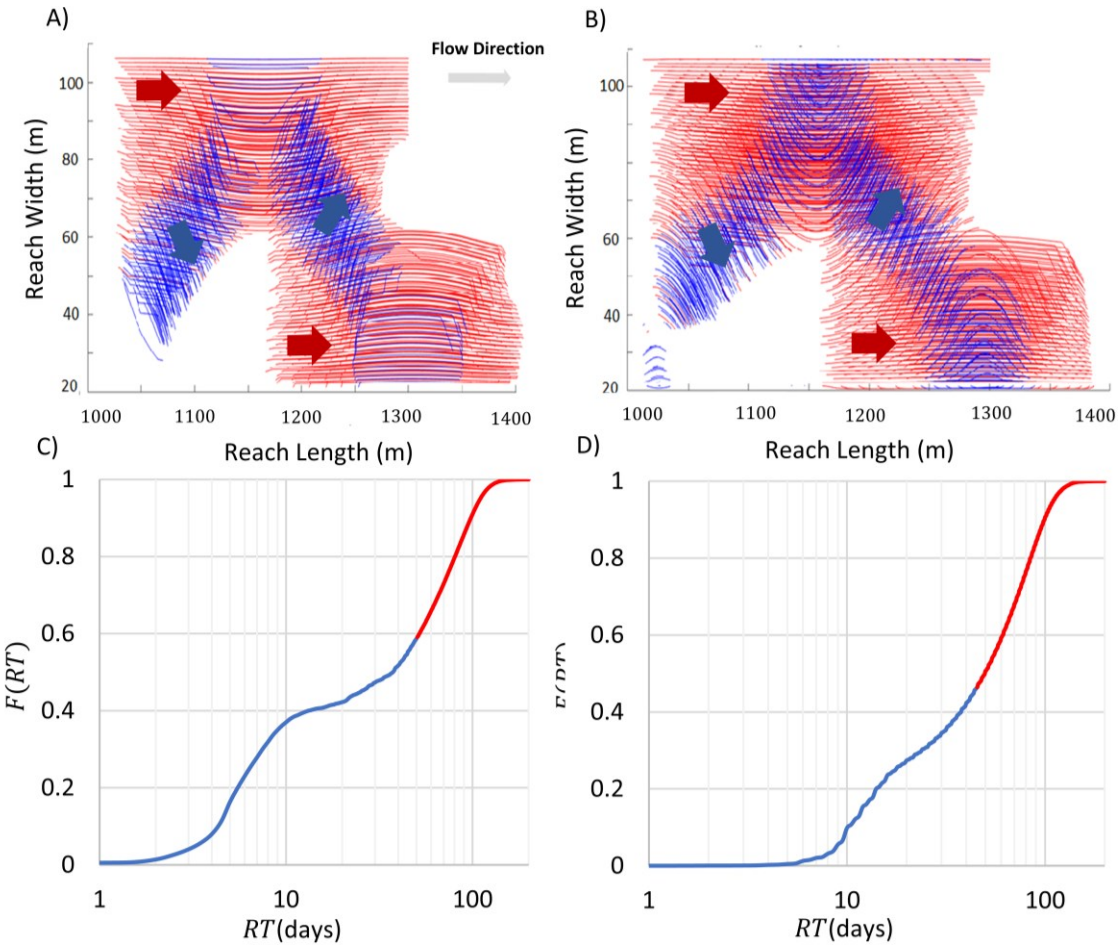

Figure 2.4: Shallow flow paths (blue paths) and deep flow paths (red paths) directions and their associated cumulative RTDs under Q_{avg} (A and C), and Q_{bf} (B and D) cases, in neutral and anisotropic conditions. The blue and red parts of cumulative RTDs line correspond to the blue paths and the red paths, respectively. The blue and red arrows in A and B arrows represent the directions of shallow and deep flow paths, respectively.

The deep flow paths are mostly influenced by the longitudinal variations of head distribution between the upstream and downstream of the riffle peak, and they travel for longer distances and remain in the HZ for a longer time (Figure 2.5 and $RTs_{90\%}$ and $RTs_{80\%}$ in Table 2.6). On the other hand, the shallower ones tend to travel within the sediment domain for a much shorter time ($RTs_{20\%}$ and $RTs_{10\%}$ in Figure 2.5 and Table 2.6) before returning to the surface water domain.

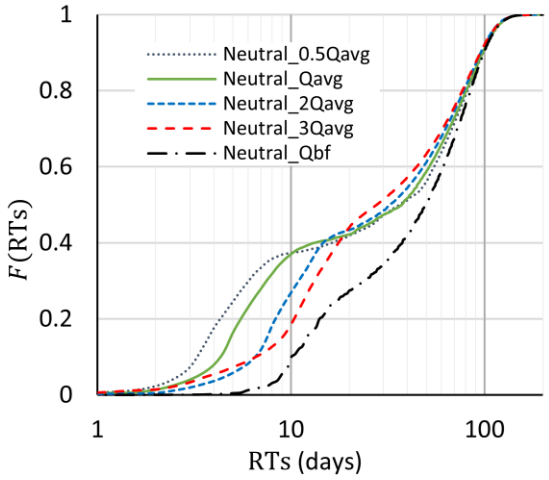

Figure 2.5: Cumulative frequency distribution of residence times (F(RTs)) in neutral and anisotropic conditions under different streamflow cases ($0.5Q_{avg}$, Q_{avg}, $2Q_{avg}$, $3Q_{avg}$, and Q_{bf}). The gray arrow represents the direction of increasing the streamflow value.

In neutral conditions ($q_{bot} = 0$), the residence times of the deep flow paths slightly decrease with increasing Q_{surf}. However, in case of full submergence, $RTs_{80\%}$ increases marginally (Table 2.6). Therefore, the values of $RTs_{80\%}$ in neutral conditions exhibit a slight sensitivity to Q_{surf} variations, implying a weak correlation between the streamflow and RTs in the deep HZ. On the other hand, while an increase in bar submergence generally undermines the role of pool-riffle sequence in driving the hyporheic exchange by reducing the pressure gradient on the streambed, the shallow hyporheic flow paths travel for a longer time for higher Q_{surf} (see $RTs_{10\%}$ and $RTs_{20\%}$ in Table 2.6 and also Figure 2.5). Trauth et al. (2013) found that the median residence times ($RTs_{50\%}$) decrease with increasing Q_{surf} in case of fully submerged bars. This trend is also present in current results for partially submerged bars (Table 2.6, $0.5\ Q_{avg}$ to $3\ Q_{avg}$), although with some minor deviations (compare $RTs_{50\%}$ for $0.5\ Q_{avg}$ and Q_{avg} in Table 2.6). The previous results indicate that residence times in deep HZ are marginally affected by Q_{surf} variations, unlike RTs in the shallow HZ which is more influenced by the surface water domain. In agreement with Tonina and Buffington (2011), the mean residence time (RTs_{mean}) decreases with increasing Q_{surf}, except for fully submerged bar, in which longer RTs within the shallow HZ cause RTs_{mean} to increase again to a higher value than those of partially submerged one.

Table 2.6: Residence times at different probability values of the cumulative frequency distributions ($RTs_{90\%}$, $RTs_{80\%}$, $RTs_{50\%}$, $RTs_{20\%}$, $RTs_{10\%}$ and RTs_{mean}; in days) in different streamflow cases ($0.5Q_{avg}, Q_{avg}, 2Q_{avg}, 3Q_{avg}$ and Q_{bf}), and in different values of gaining and losing conditions (q_{bot} is expressed as a fraction of the hyporheic exchange flux in the neutral conditions, q_{h_n}).

Groundwater fluxes	$\mathbf{0.5\ Q_{avg}}$					
	$RTs_{90\%}$	$RTs_{80\%}$	$RTs_{50\%}$	$RTs_{20\%}$	$RTs_{10\%}$	RTs_{mean}
$q_{bot} = 0$ (neutral)	98.5	81.5	36	4	3	64
$q_{bot} = +0.5\ q_{h_n}$						
$q_{bot} = -0.5\ q_{h_n}$						
$q_{bot} = +\ q_{h_n}$	27	16	7	3.5	2.5	21.7
$q_{bot} = -\ q_{h_n}$	25.5	11	4.5	2.5	2	18.3
$q_{bot} = +1.5\ q_{h_n}$						
$q_{bot} = -1.5\ q_{h_n}$						
$q_{bot} = +2\ q_{h_n}$	17	12.5	6.5	3	2	10.9
$q_{bot} = -2\ q_{h_n}$	9.5	7	3.5	2	1.5	12.2
$q_{bot} = +3\ q_{h_n}$	0	0	0	0	0	0
$q_{bot} = -3\ q_{h_n}$	0	0	0	0	0	0

Groundwater fluxes	$\boldsymbol{Q_{avg}}$					
	$RTs_{90\%}$	$RTs_{80\%}$	$RTs_{50\%}$	$RTs_{20\%}$	$RTs_{10\%}$	RTs_{mean}
$q_{bot} = 0$ (neutral)	97.5	80	37	5	4	56.5
$q_{bot} = +0.5\ q_{h_n}$	57.5	44	10	5	3.5	32.5
$q_{bot} = -0.5\ q_{h_n}$	63	45.5	8	4	3.5	35.7
$q_{bot} = +\ q_{h_n}$	41	27.5	8.5	4	3	28.2
$q_{bot} = -\ q_{h_n}$	35.5	15.5	6	4	3	21.2
$q_{bot} = +1.5\ q_{h_n}$	19	13	6.5	3.5	3	21.4
$q_{bot} = -1.5\ q_{h_n}$	22	14.5	7	3.5	2.5	17.1
$q_{bot} = +2\ q_{h_n}$	15.5	11.5	6	3	2.5	18
$q_{bot} = -2\ q_{h_n}$	13.5	10	6	3	2.5	17.6
$q_{bot} = +3\ q_{h_n}$	14	10	5.5	2.5	2	211.4
$q_{bot} = -3\ q_{h_n}$	10.5	7.5	4	2.5	2	7.3

$2\ Q_{avg}$

Groundwater fluxes	$RTs_{90\%}$	$RTs_{80\%}$	$RTs_{50\%}$	$RTs_{20\%}$	$RTs_{10\%}$	RTs_{mean}
$q_{bot} = 0$ (neutral)	95.5	78	32.5	8	6.5	54.7
$q_{bot} = +0.5\ q_{h_n}$						
$q_{bot} = -0.5\ q_{h_n}$						
$q_{bot} = +\ q_{h_n}$	41	27.5	10.5	5.5	3.5	31.5
$q_{bot} = -\ q_{h_n}$	45	29	11.5	6.5	4.5	27.6
$q_{bot} = +1.5\ q_{h_n}$						
$q_{bot} = -1.5\ q_{h_n}$						
$q_{bot} = +2\ q_{h_n}$	14.5	11.5	6.5	3.5	2.5	18.6
$q_{bot} = -2\ q_{h_n}$	17.5	14	8.5	4.5	3.5	16.3
$q_{bot} = +3\ q_{h_n}$	14.5	13.5	6	3	2.5	12.6
$q_{bot} = -3\ q_{h_n}$	14.5	13.5	6	3.5	2.5	11.9

$3\ Q_{avg}$

Groundwater fluxes	$RTs_{90\%}$	$RTs_{80\%}$	$RTs_{50\%}$	$RTs_{20\%}$	$RTs_{10\%}$	RTs_{mean}
$q_{bot} = 0$ (neutral)	95	76.5	27.5	10	6.5	52.3
$q_{bot} = +0.5\ q_{h_n}$						
$q_{bot} = -0.5\ q_{h_n}$						
$q_{bot} = +\ q_{h_n}$	38	23.5	11	5	3	29.6
$q_{bot} = -\ q_{h_n}$	40	26	13	7	4.5	32.7
$q_{bot} = +1.5\ q_{h_n}$						
$q_{bot} = -1.5\ q_{h_n}$						
$q_{bot} = +2\ q_{h_n}$	19	13	6	3	2.5	24
$q_{bot} = -2\ q_{h_n}$	21.5	15	7.5	4	1.5	26.8
$q_{bot} = +3\ q_{h_n}$	11.5	7.5	4	3	1.5	17.9
$q_{bot} = -3\ q_{h_n}$	13	9	4.5	1.5	1	20

Q_{bf}

Groundwater fluxes	$RTs_{90\%}$	$RTs_{80\%}$	$RTs_{50\%}$	$RTs_{20\%}$	$RTs_{10\%}$	RTs_{mean}
$q_{bot} = 0$ (neutral)	94.5	84	49.5	14	10	59
$q_{bot} = +0.5\ q_{h_n}$	67.5	56	28.5	10.5	8.5	40.7
$q_{bot} = -0.5\ q_{h_n}$	68	57	30	11	9	41.9
$q_{bot} = +\ q_{h_n}$	47	37	15	9	7	29.4

$q_{bot} = -\,q_{h_n}$	49	39	15.5	9.5	7.5	31.9
$q_{bot} = +1.5\,q_{h_n}$	30.5	22	13.5	9	7.5	26.8
$q_{bot} = -1.5\,q_{h_n}$	31	22	13.5	9	7.5	15.4
$q_{bot} = +2\,q_{h_n}$	27	21	13	10	9	26.1
$q_{bot} = -2\,q_{h_n}$	26	20.5	13	9	8	28.4
$q_{bot} = +3\,q_{h_n}$	0	0	0	0	0	0
$q_{bot} = -3\,q_{h_n}$	0	0	0	0	0	0

Generally, RTs values lessen with raising q_{bot} magnitude (Table 2.6 and Figure 2.6). At strong q_{bot}, in both gaining and losing conditions, the cumulative RTD shifts from a bimodal to a unimodal distribution (Figure 2.6). This shift indicates the disappearance of a significant part of the deep hyporheic zone, with the two HZ parts merging into a single shallow hyporheic zone.

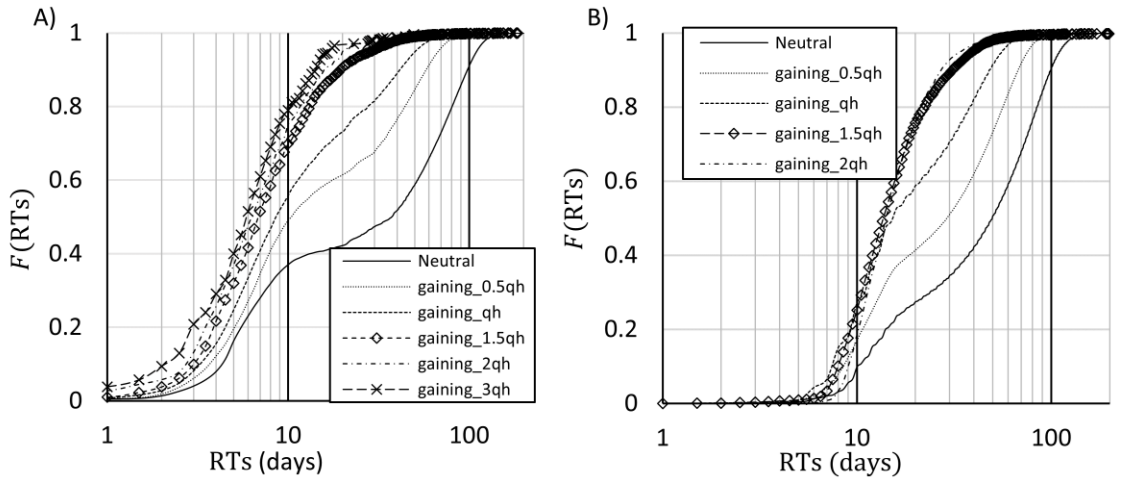

Figure 2.6: Cumulative frequency distribution function of residence times ($F(\mathrm{RTs})$) under different gaining fluxes ($q_{bot} = 0, +0.5q_{h_n}, +q_{h_n}, +1.5\,q_{h_n}, +2q_{h_n}$, and $+3q_{h_n}$), and different Q_{surf} cases (Q_{avg} (A) and Q_{bf}(B)), in anisotropic conditions.

Differently from previous studies (Marzadri et al., 2010; Tonina & Buffington, 2011; Trauth et al., 2013), the cumulative RTDs do not follow a lognormal distribution. However, they are bimodal in both isotropic and anisotropic conditions. Even though the bimodality is very mild in the isotropic conditions (Figure 2.7), it is still detected by the HDS_w/BC and HDS tests. Evidently in the results, sediment anisotropy enhances the distinction between the shallow and deep flow paths. In addition, bar submergence plays a role in forming this bimodal distribution, as increasing the bar submergence decreases the degree of bimodality (Figure 2.7). This bimodality existence is coherent with the presence of two groups of flow paths in both conditions, reported by Trauth et al. (2013) and Tonina and Buffington (2007). Sediment anisotropy also affects the ratio of flow paths that infiltrate

into either the deep or the shallow zone. In isotropic conditions, more than 85% of the flow paths reach the deep zone, unlike in anisotropic conditions in which the flow paths are almost evenly split between both hyporheic zones (Figure 2.7). In agreement with (Marzadri et al., 2010), RTs_{mean} is slightly longer in anisotropic sediments (Table 2.7) than in isotropic ones, this is also true for deep flow paths ($RTs_{80\%}$ and $RTs_{90\%}$ in Table 2.7), as the lower vertical resistance to flow allows for faster and deeper flow within the sediment. On the other hand, shorter residence times ($RTs_{10\%}$, $RTs_{20\%}$ and $RTs_{50\%}$ in Table 2.7) have smaller values in anisotropic conditions.

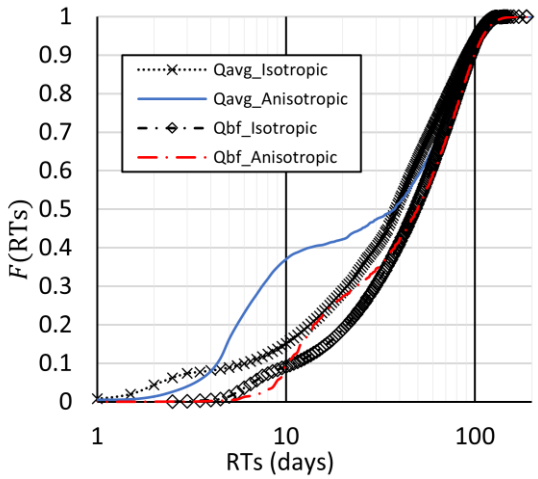

Figure 2.7: Cumulative frequency distribution of residence times (F(RTs)) in isotropic and anisotropic conditions, for Q_{avg} and Q_{bf} in neutral conditions.

Table 2.7: Residence times at different probability values of the cumulative frequency distributions ($RTs_{90\%}$, $RTs_{80\%}$, $RTs_{50\%}$, $RTs_{20\%}$, $RTs_{10\%}$ and RTs_{mean}; in days) in isotropic and anisotropic, and neutral conditions.

	Isotropic condition					
Stream Flow	$RTs_{90\%}$	$RTs_{80\%}$	$RTs_{50\%}$	$RTs_{20\%}$	$RTs_{10\%}$	RTs_{mean}
Q_{avg}	91	72.5	38	13	6	39.7
Q_{bf}	94.5	80.5	48	21	11	50.8

Stream Flow	Anisotropic condition					
	$RTs_{90\%}$	$RTs_{80\%}$	$RTs_{50\%}$	$RTs_{20\%}$	$RTs_{10\%}$	RTs_{mean}
Q_{avg}	97.5	80	37	5	4	53
Q_{bf}	99	84	49.5	14	10	55.5

2.3.4 Hyporheic Depths.

The penetration of the flow paths in the hyporheic zone delineates the hyporheic depth in the subsurface domain (Figure 2.8, for Q_{avg} and Q_{bf}). In the neutral conditions, increasing Q_{surf} decreases the hyporheic depth in both shallow and deep sub-zones for partially submerged bars (Table 2.8). This decrease in hyporheic depth with increasing Q_{surf} is due to milder pressure head variations on the bars morphology, which agrees with the literature results (compare Z_{mean} in Table 2.8 with Figure 2 in Tonina and Buffington (2011)). This trend does not apply for shallow HZ, which can have a deeper extent in fully submerged bars than in the lower submergence case. This difference can be due to the different portions of flow paths between the shallow and deep HZ.

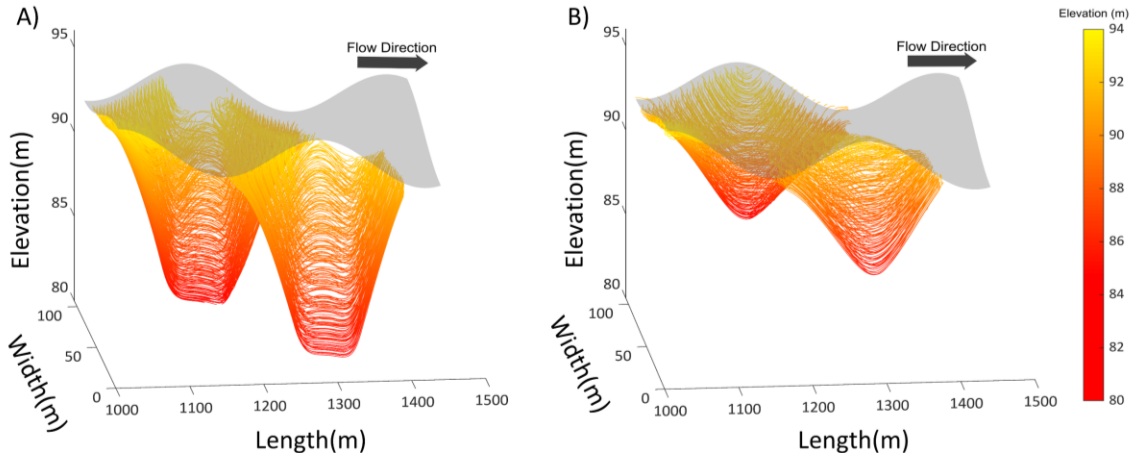

Figure 2.8: Hyporheic flow paths extent, in neutral and anisotropic conditions, within the subsurface domain in (A) Q_{avg} and (B) Q_{bf} cases. The grey surface represents the streambed elevation. The flow paths direction is the same as the flow direction (from left to right).

The imposed gaining and losing conditions decrease the extent of the hyporheic zone considerably (Table 2.8 and Figure 2.9). The deeper flow paths ($Z_{80\%}$ and $Z_{90\%}$) as well as the mean and median hyporheic depth (Z_{mean}, and $Z_{50\%}$, respectively) are more affected by q_{bot} (faster decrease at lower q_{bot}) than the depth of the shallow HZ one. This happens

because the deep HZ is more interactive with the ambient groundwater (Table 2.6 and Table 2.8), while the shallow HZ is more linked to surface water. When q_{bot} is higher than 2 q_h, the shallow depths ($Z_{10\%}$ and $Z_{20\%}$ values in Table 2.8) are also influenced, as the large upwelling flux diminishes the deep HZ extent and interferes with the shallow flow paths.

The lower resistance to the vertical flow in isotropic conditions results in much deeper HZ (Table 2.9). The increase in the extent of the deep HZ is much higher compared the shallow one, as the latter is more influenced by Q_{surf} and the bed morphology.

Table 2.8: Maximum hyporheic depth at different probability values of the cumulative frequency distributions ($Z_{90\%}$, $Z_{80\%}$, $Z_{50\%}$, $Z_{20\%}$, $Z_{10\%}$, and Z_{mean}; in meters) in different streamflow cases ($0.5Q_{avg}, Q_{avg}, 2Q_{avg}, 3Q_{avg}$ and Q_{bf}), and different values of gaining and losing conditions (q_{bot} is expressed as a fraction of the hyporheic exchange flux in the neutral conditions, q_{h_n}).

$0.5\ Q_{avg}$

Groundwater fluxes	$Z_{90\%}$	$Z_{80\%}$	$Z_{50\%}$	$Z_{20\%}$	$Z_{10\%}$	Z_{mean}
$q_{bot} = 0$ (neutral)						
$q_{bot} = +0.5\ q_{h_n}$	8.38	6.45	2.43	0.63	0.42	4.59
$q_{bot} = -0.5\ q_{h_n}$						
$q_{bot} = +\ q_{h_n}$	1.25	0.92	0.55	0.3	0.23	0.6
$q_{bot} = -\ q_{h_n}$	1.43	1.02	0.62	0.37	0.3	0.88
$q_{bot} = +1.5\ q_{h_n}$						
$q_{bot} = -1.5\ q_{h_n}$						
$q_{bot} = +2\ q_{h_n}$	0.72	0.58	0.25	0.06	0.03	0.33
$q_{bot} = -2\ q_{h_n}$	1.06	0.73	0.41	0.28	0.25	0.41
$q_{bot} = +3\ q_{h_n}$	0	0	0	0	0	0
$q_{bot} = -3\ q_{h_n}$	0	0	0	0	0	0

Q_{avg}

Groundwater fluxes	$Z_{90\%}$	$Z_{80\%}$	$Z_{50\%}$	$Z_{20\%}$	$Z_{10\%}$	Z_{mean}
$q_{bot} = 0$ (neutral)	7.82	5.87	2.01	0.62	0.42	3.73
$q_{bot} = +0.5\ q_{h_n}$	4.31	3.09	1.25	0.77	0.62	1.93
$q_{bot} = -0.5\ q_{h_n}$	3.28	2.16	1	0.67	0.57	1.78
$q_{bot} = +\ q_{h_n}$	2.32	1.39	0.68	0.36	0.29	0.9
$q_{bot} = -\ q_{h_n}$	1.71	1.01	0.62	0.38	0.3	0.91
$q_{bot} = +1.5\ q_{h_n}$	1.03	0.86	0.56	0.32	0.26	0.55

$q_{bot} = -1.5\, q_{h_n}$	1.41	1.06	0.58	0.35	0.29	0.59
$q_{bot} = +2\, q_{h_n}$	1	0.83	0.48	0.28	0.1	0.46
$q_{bot} = -2\, q_{h_n}$	1.24	0.56	0.4	0.3	0.28	0.46
$q_{bot} = +3\, q_{h_n}$	0.75	0.6	0.3	0.11	0.08	0.38
$q_{bot} = -3\, q_{h_n}$	1.11	0.64	0.4	0.28	0.24	0.43

$2\, Q_{avg}$

Groundwater fluxes	$Z_{90\%}$	$Z_{80\%}$	$Z_{50\%}$	$Z_{20\%}$	$Z_{10\%}$	Z_{mean}
$q_{bot} = 0$ (neutral)	6.49	4.78	1.53	0.57	0.4	2.76
$q_{bot} = +0.5\, q_{h_n}$						
$q_{bot} = -0.5\, q_{h_n}$						
$q_{bot} = +\, q_{h_n}$	2.18	0.96	0.65	0.38	0.3	0.9
$q_{bot} = -\, q_{h_n}$	2.09	1.34	0.65	0.39	0.32	0.86
$q_{bot} = +1.5\, q_{h_n}$						
$q_{bot} = -1.5\, q_{h_n}$						
$q_{bot} = +2\, q_{h_n}$	0.89	0.74	0.42	0.18	0.1	0.41
$q_{bot} = -2\, q_{h_n}$	0.85	0.73	0.5	0.35	0.3	0.48
$q_{bot} = +3\, q_{h_n}$	0.88	0.68	0.29	0.1	0.07	0.36
$q_{bot} = -3\, q_{h_n}$	6.49	4.78	1.53	0.57	0.4	2.76

$3\, Q_{avg}$

Groundwater fluxes	$Z_{90\%}$	$Z_{80\%}$	$Z_{50\%}$	$Z_{20\%}$	$Z_{10\%}$	Z_{mean}
$q_{bot} = 0$ (neutral)	5.16	3.76	1.15	0.54	0.38	2.09
$q_{bot} = +0.5\, q_{h_n}$						
$q_{bot} = -0.5\, q_{h_n}$						
$q_{bot} = +\, q_{h_n}$	1.3	0.96	0.65	0.38	0.3	0.69
$q_{bot} = -\, q_{h_n}$	1.57	1.05	0.67	0.37	0.29	0.73
$q_{bot} = +1.5\, q_{h_n}$						
$q_{bot} = -1.5\, q_{h_n}$						
$q_{bot} = +2\, q_{h_n}$	0.71	0.62	0.44	0.3	0.26	0.4
$q_{bot} = -2\, q_{h_n}$	0.77	0.65	0.46	0.28	0.2	0.44
$q_{bot} = +3\, q_{h_n}$	0.63	0.56	0.38	0.26	0.11	0.34
$q_{bot} = -3\, q_{h_n}$	0.65	0.59	0.36	0.21	0.1	0.35

	Q_{bf}					
Groundwater fluxes	$Z_{90\%}$	$Z_{80\%}$	$Z_{50\%}$	$Z_{20\%}$	$Z_{10\%}$	Z_{mean}
$q_{bot} = 0$ (neutral)	4.79	3.84	1.83	0.6	0.43	2.03
$q_{bot} = +0.5\ q_{h_n}$	2.69	2.05	0.79	0.28	0.2	1.06
$q_{bot} = -0.5\ q_{h_n}$	2.75	2.15	0.92	0.32	0.23	1.12
$q_{bot} = +\ q_{h_n}$	1.28	0.96	0.38	0.22	0.17	0.55
$q_{bot} = -\ q_{h_n}$	1.41	1.14	0.46	0.27	0.21	0.64
$q_{bot} = +1.5\ q_{h_n}$	0.46	0.37	0.27	0.18	0.15	0.29
$q_{bot} = -1.5\ q_{h_n}$	0.56	0.38	0.26	0.19	0.17	0.33
$q_{bot} = +2\ q_{h_n}$	0.37	0.31	0.23	0.17	0.15	0.25
$q_{bot} = -2\ q_{h_n}$	0.57	0.48	0.32	0.22	0.18	0.36
$q_{bot} = +3\ q_{h_n}$	0	0	0	0	0	0
$q_{bot} = -3\ q_{h_n}$	0	0	0	0	0	0

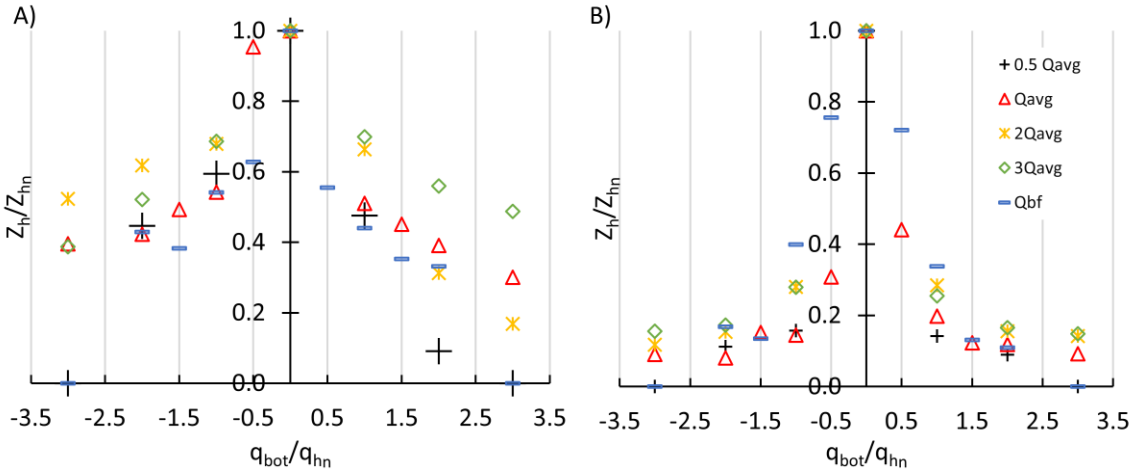

Figure 2.9: (A) Shallow hyporheic depth ($Z_{10\%}$) normalized by its corresponding value in neutral condition (Z_{10hn}). (B) Deep hyporheic depth ($Z_{90\%}$) normalized by its corresponding value in neutral condition (Z_{90hn}). q_{bot}/q_{hn} on the horizontal axes represents gaining (+ sign) and losing (− sign) conditions, where q_{bot} is the value of imposed ambient groundwater and q_{hn} is the hyporheic flux in neutral condition. The depths values in both (A and B) refer only to anisotropic conditions.

Table 2.9: Maximum hyporheic depth at different probability values of the cumulative frequency distributions ($Z_{90\%}$, $Z_{80\%}$, $Z_{50\%}$, $Z_{20\%}$, $Z_{10\%}$, and Z_{mean}; in meters) in isotropic and anisotropic and neutral conditions.

	Isotropic condition					
Stream Flow	$Z_{90\%}$	$Z_{80\%}$	$Z_{50\%}$	$Z_{20\%}$	$Z_{10\%}$	Z_{mean}
Q_{avg}	35.74	29.49	15.59	4.43	1.03	14.09
Q_{bf}	27.87	22.82	11.73	3.54	1.25	11.14

	Anisotropic condition					
Stream Flow	$Z_{90\%}$	$Z_{80\%}$	$Z_{50\%}$	$Z_{20\%}$	$Z_{10\%}$	Z_{mean}
Q_{avg}	7.82	5.87	2.01	0.62	0.42	3.73
Q_{bf}	4.79	3.84	1.83	0.6	0.43	2.03

2.3.4 Predictive Model Results.

The existing predictive equations proposed in previous studies (Huang & Chui, 2018; Tonina & Buffington, 2011; Trauth et al., 2013) were found to provide erroneous estimate of the results of this study in some conditions. Hence, new equations were developed by performing the MLR to identify coefficient values for Eqs. (2.5) and (2.6).

Both models include all the independent variables, as their variance inflation factor (VIF) did not exceed 5, which indicates no significant correlation exists among the independent variables (no multi-collinearity) (Ott et al., 2004). Consequently, the predictive equations are:

$$F^{neutral} = 10^{(a\pm SE_a)} \times R_e^{(b\pm SE_b)} \times \left(\frac{K_v}{K_h}\right)^{(c\pm SE_c)} \quad (2.7)$$

$$F^{gain/los} = 10^{(m\pm SE_m)} \times R_e^{(n\pm SE_n)} \times \left(\left|\frac{q_{bot}}{V}\right|\right)^{(g\pm SE_g)} \quad (2.8)$$

where SE is the standard error associated with the estimated value of each coefficient.

Tables 2.10 and 2.11 show the coefficients values, SE and *P-Values* of each regression coefficient. In neutral conditions, the model works quite well in predicting the simulations

results ($R^2 > 0.93$) (Figures 2.10 and 2.12 and Table 2.10). By looking at the regression coefficients values, the Reynolds number has a strong influence on q_h and Q_h values, while $\mathrm{RTs}_{i\%}$ are more affected by sediment anisotropy. Instead, $Z_{i\%}$ are almost equally affected, within error, by both independent variables (R_e and K_v).

On the other hand, in gaining and losing conditions, the model predicts reasonably well, q_h and Q_h ($R^2 > 0.74$, Figure 2.10), and it also fits better residence times and hyporheic depths of the deep HZ (most of the predicted values are within 90% confidence interval) than the shallow one (compare $\mathrm{RTs}_{90\%}$ and $Z_{90\%}$ to $\mathrm{RTs}_{10\%}$ and $Z_{10\%}$ in Figures 2.11 and 2.12). Similar to the neutral conditions, R_e has a higher effect on q_h and Q_h than the groundwater flux (q_{bot}/V) (Table 2.11).

The novelty of these predictive equations lies in considering the sediment anisotropy as an independent variable. Evidently, it can play a significant role in estimating HZ characteristics, in addition to the inclusion of q_{bot} changes in both gaining and losing conditions. Even though it is hard to build a generalized model, this model helps to understand the dependence of the HZ characteristics on streamflow, sediment anisotropy, and groundwater fluxes.

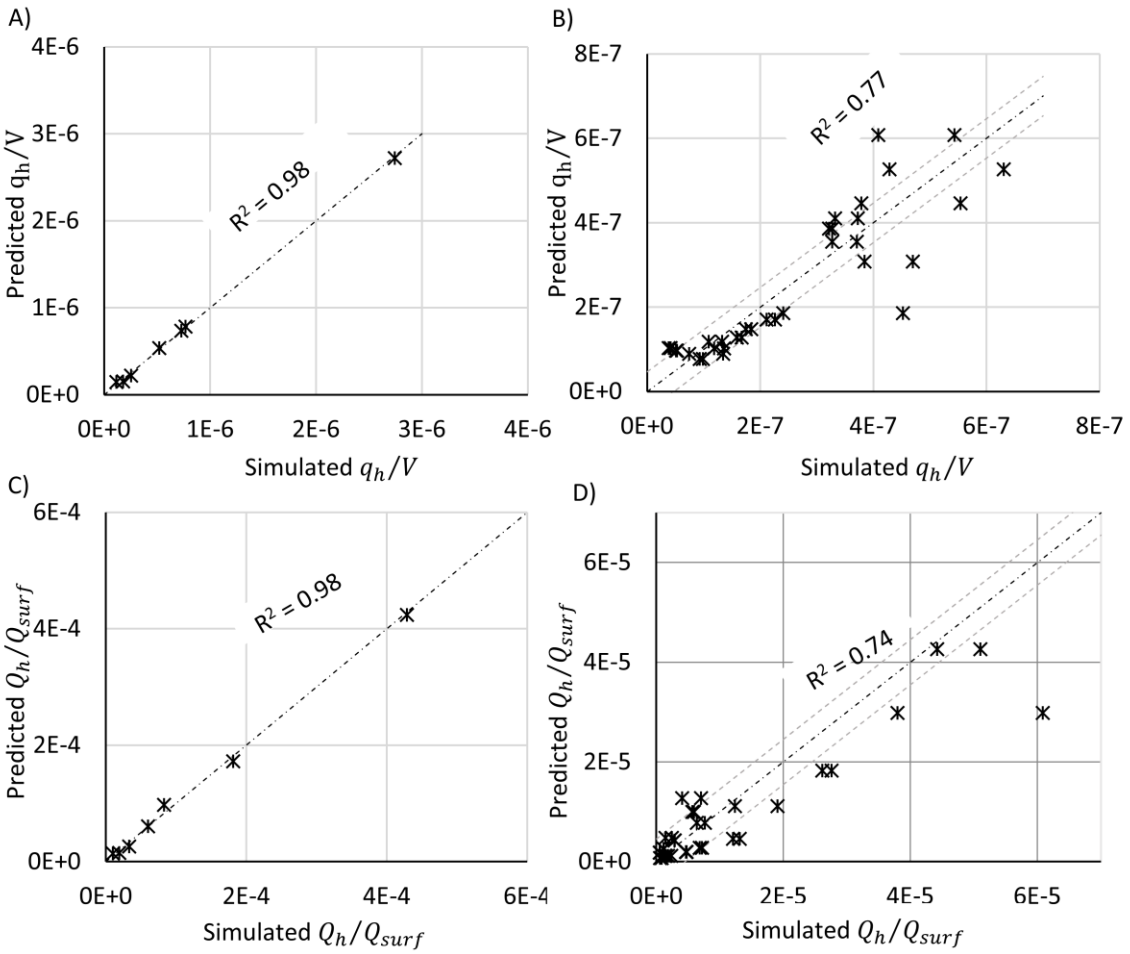

Figure 2.10: Comparison between simulated values of q_h/V and Q_h/Q_{surf}, and the predicted values by Eqs. (2.7) and (2.8); A and C are in neutral condition (Eq. (2.7)), and B and D are in gaining/losing conditions (Eq. (2.8)).

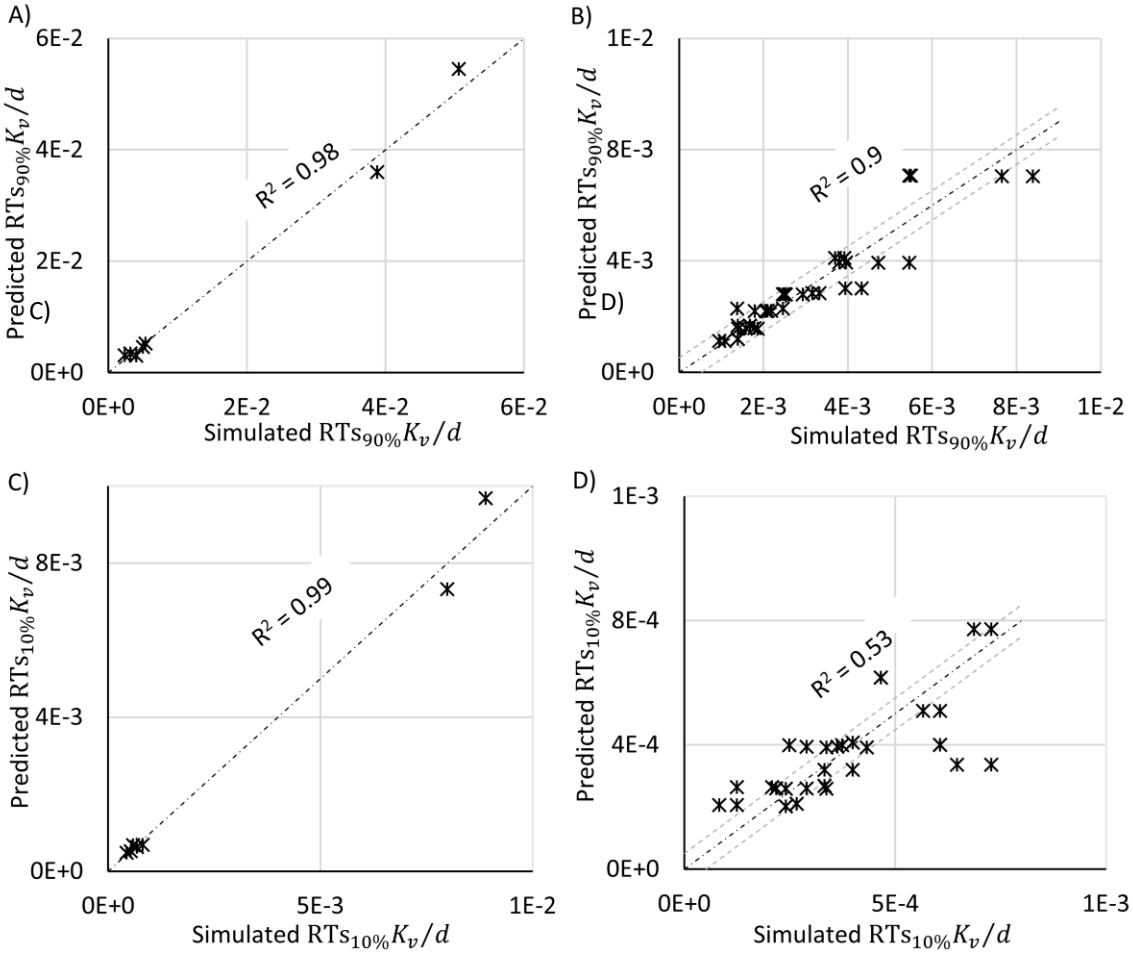

Figure 2.11: Comparison between simulated values of deep and shallow HZ dimensionless residence times ($RTs_{90\%}\ K_v/d$ and $RTs_{10\%}K_v/d$), and the predicted values by Eqs. (2.7) and (2.8) the simulations ones; A and C are in neutral condition (Eq.(2.7)), and B and D are in gaining/losing conditions (Eq.(2.8)).

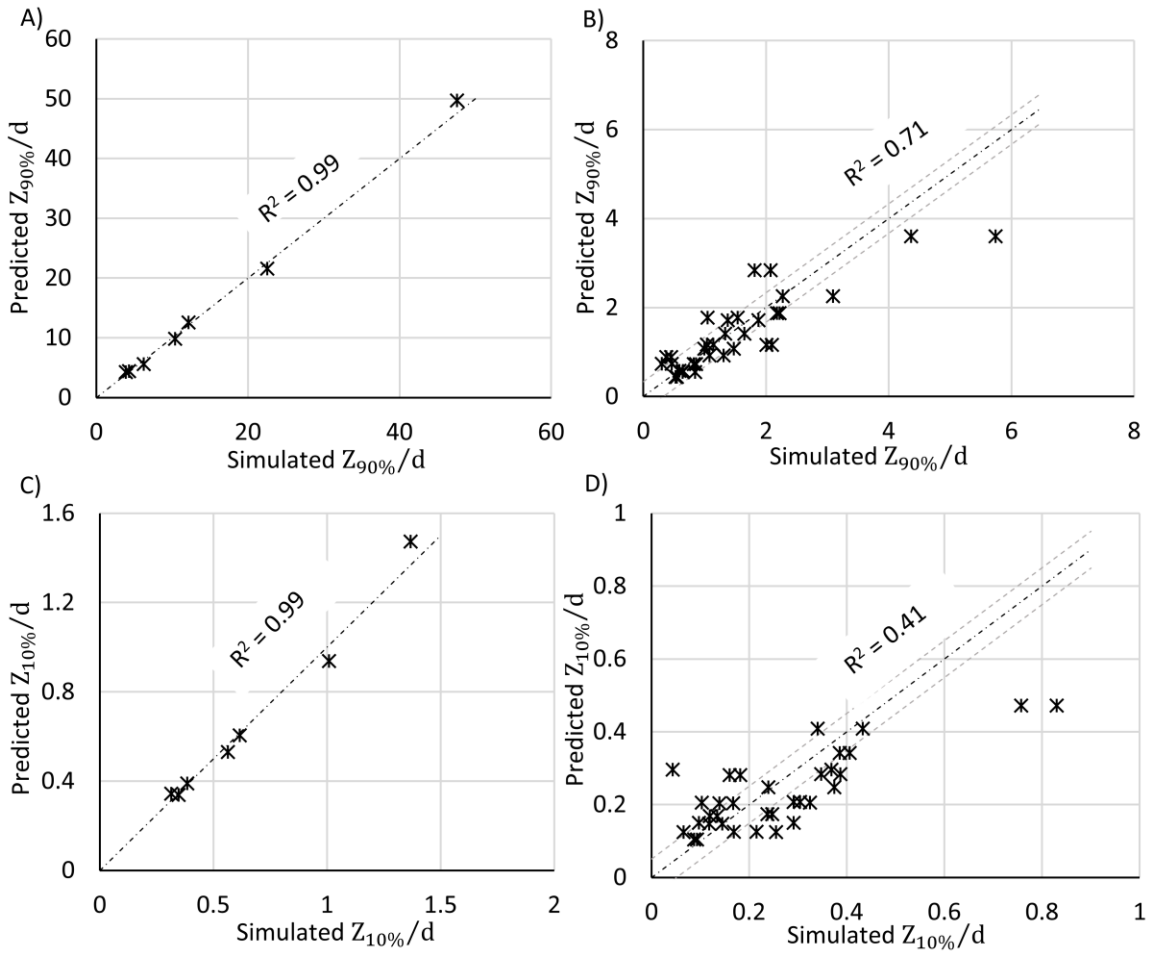

Figure 2.12: Comparison between simulated values of deep and shallow HZ dimensionless residence times $Z_{90\%}/d$ and $Z_{10\%}/d$, and the predicted values by Eqs. (2.7) and (2.8) the simulations ones; A and C are in neutral condition (Eq. (2.7)), and B and D are in gaining/losing conditions (Eq. (2.8)).

2.4 Concluding Remarks.

The effect of streamflow, bar submergence, and isotropic variations were analyzed in this study. Although the hyporheic exchange area increases with higher submergence, the total hyporheic flow decreases due to the decrease in hyporheic flux per unit streambed area. The hyporheic zone is divided into two zones: a shallow zone with quasi-lateral flow paths underneath the pools-riffles sequence, and a deep zone with longitudinal flow paths under the bar's peaks. The presence of these two hyporheic zones having different flow directions and penetration depth is a peculiarity of the hyporheic flow field below bars, as they cannot found in the case of hyporheic exchange below dunes. The residence times

distribution is bimodal, which is more emphasized in anisotropic conditions. This bimodality supports the existence of two hyporheic zones with different characteristics. The residence times within the shallow zone become longer at a higher bar submergence ratio, while in the deep one, they are less sensitive to streamflow variations. The hyporheic zone extent becomes shallower with an increasing bar submergence ratio due to less pressure variation on the sediment bed. The presence of ambient groundwater flux reduces the hyporheic exchange flow, residence times, and hyporheic zone extent, especially within the deep zone. The hyporheic zone characteristics are significantly affected by sediment anisotropy; the hyporheic flow and hyporheic zone extent are enhanced considerably in isotropic sediment (higher vertical conductivity) compared to the anisotropic conditions. However, the residence times follow different trends for the shallow and deep zones. A set of the predictive formulae was introduced to predict hyporheic flux, residence times, and hyporheic depths and quantify the influence of the three factors discussed in this study (streamflow value (bar submergence ratio), ambient groundwater, and sediment anisotropy). Further investigations need to be carried out with different alternate bars geometry to determine its effect on the hyporheic zone characteristics and to expand the introduced predictive model. Finally, the division of the hyporheic zones into two zones with different traits is likely to influence the biogeochemical conditions and reactions, which needs deeper investigations.

Table 2.10: Regression coefficients for Eq. (2.7) (Neutral Condition).

$F^{Neutral}$	Regression Coefficients								Model performance			
	a	SE_a	$P.Val_a$	b	SE_b	$P.Val_b$	c	SE_c	$P.Val_c$	R^2	AIC	$RMSE$
q_h/V	1.71	0.69	0.07	-1.25	0.11	4.00E-04	0.71	0.06	3.00E-04	0.99	-7.12	0.071
Q_h/Q_{surf}	7.42	1.08	0.002	-1.85	0.18	5.00E-04	0.64	0.09	0.002	0.98	-0.95	0.11
$T_{90\%}K_v/d$	1.7	0.08	3.00E-05	-0.45	0.01	4.70E-06	0.98	0.007	1.50E-08	0.93	-37.1	0.08
$T_{80\%}K_v/d$	1.52	0.17	8.00E-04	-0.43	0.03	9.00E-05	0.98	0.01	3.00E-07	0.999	-27.1	0.02
$T_{50\%}K_v/d$	1.05	0.91	0.31	-0.4	0.15	0.06	1.07	0.08	2.00E-04	0.98	-3.3	0.09
$T_{20\%}K_v/d$	-3.06	0.6	0.007	0.21	0.1	0.09	1.31	0.05	1.00E-05	0.99	-9.2	0.06
$T_{10\%}K_v/d$	-3.69	0.6	0.004	0.27	0.1	0.05	1.15	0.05	2.00E-05	0.99	-9.1	0.06
$T_{mean}K_v/d$	1.17	0.6	0.12	-0.41	0.1	0.02	0.93	0.05	6.00E-05	0.99	-9.1	0.06
$Z_{90\%}/d$	6.3	0.38	7.00E-05	-0.8	0.06	2.00E-04	0.7	0.03	3.00E-05	0.99	-15.6	0.04
$Z_{80\%}/d$	6.3	0.3	3.00E-05	-0.8	0.05	8.00E-05	0.74	0.03	8.00E-06	0.99	-19.06	0.03
$Z_{50\%}/d$	5.9	0.72	0.001	-0.8	0.12	0.003	0.9	0.06	1.00E-04	0.98	-6.63	0.04
$Z_{20\%}/d$	4.03	0.29	2.00E-04	-0.56	0.05	3.00E-04	0.83	0.02	5.00E-06	0.997	-19.5	0.03
$Z_{10\%}/d$	2.68	0.33	0.001	-0.43	0.05	0.001	0.44	0.03	9.00E-05	0.99	-17.7	0.03
Z_{mean}/d	6.77	0.5	1.00E-04	-0.93	0.08	3.00E-04	0.65	0.04	1.00E-04	0.99	-11.8	0.05

Table 2.11: Regression coefficients for Eq. (4.8) (Gaining/ Losing Conditions).

$F^{gain/loss}$	Regression Coefficients								Model performance			
	a	SE_a	$P.Val_a$	b	SE_b	$P.Val_b$	c	SE_c	$P.Val_c$	R^2	AIC	$RMSE$
q_h/V	0.81	0.8	0.31	-1.02	0.19	7.00E-07	0.21	0.11	7.00E-02	0.77	-19.7	0.11
Q_h/Q_{surf}	6.02	1.443	2.00E-04	-3.16	0.34	1.80E-10	-1.22	0.2	8.00E-07	0.74	20.4	0.31
$T_{90\%}K_v/d$	-0.59	0.38	1.30E-01	-1.22	0.09	1.00E-14	-0.84	0.05	2.00E-16	0.9	-70.4	0.08
$T_{80\%}K_v/d$	-1.48	0.44	2.00E-03	-1.06	0.11	2.00E-11	-0.81	0.06	3.00E-14	0.85	-59.8	0.1
$T_{50\%}K_v/d$	-3.07	0.45	1.00E-07	-0.62	0.11	2.00E-06	-0.6	0.06	1.00E-10	0.75	-59	0.1
$T_{20\%}K_v/d$	-3.61	0.6	2.00E-07	-0.52	0.13	4.00E-04	-0.53	0.08	7.00E-08	0.63	-45.2	0.11
$T_{10\%}K_v/d$	-3.33	0.73	8.00E-05	-0.66	0.17	7.00E-04	-0.6	0.1	2.00E-06	0.53	-25.5	0.16
$T_{mean}K_v/d$	-1.63	0.38	2.00E-04	-0.7	0.09	7.00E-09	-0.5	0.05	8.00E-11	0.75	-70.7	0.08
$Z_{90\%}/d$	5.48	0.77	6.00E-08	-1.61	0.18	7.00E-10	-0.68	0.11	5.00E-07	0.71	-21.6	0.17
$Z_{80\%}/d$	4.68	0.72	3.00E-07	-1.42	0.17	2.00E-09	-0.6	0.1	1.00E-06	0.69	-27.8	0.15
$Z_{50\%}/d$	3.9	0.64	9.00E-07	-1.15	0.15	2.00E-08	-0.4	0.09	4.00E-05	0.65	-34.5	0.14
$Z_{20\%}/d$	3.23	0.9	1.00E-03	-1.03	0.21	4.00E-05	-0.38	0.13	5.00E-03	0.43	-11.2	0.19
$Z_{10\%}/d$	3.44	1.07	0.003	-1.17	0.25	7.00E-05	-0.46	0.15	4.00E-03	0.41	0.28	0.23
Z_{mean}/d	5.48	0.77	6.00E-08	-1.61	0.18	7.00E-10	-0.68	0.11	5.00E-07	0.71	-21.6	0.17

Chapter 3
The Effect of Sediment Depth and Groundwater Underflow on Hyporheic Residence Times Distribution in Dune-Like Bedform

3.1 Introduction

Experimental and modeling studies support the conclusion that bedforms, such as ripples and dunes, play a dominant role in the mixing of water across the sediment-water interface and through the hyporheic zone (Gomez-Velez et al., 2015). A key characteristic of the exchange process is the distribution of travel times over which water parcels cycle from the stream, through the hyporheic zone, and back, i.e., the hyporheic residence times distribution (RTDs). RTDs and their statistical moments are key controls on hyporheic metabolism in the streambed (Gomez et al., 2012; Harvey & Gooseff, 2015). For instance, the Damköhler number, a dimensionless number that compares the median hyporheic residence time and the characteristic biogeochemical reaction time, is a key predictor of nitrogen removal in streams by denitrification (Azizian et al., 2015; Grant et al., 2018; Zarnetske et al., 2012), and the emission of the potent greenhouse gas nitrous oxide (N_2O) (Marzadri et al., 2014, 2017). Gomez-Velez et al. (2015) included the Damköhler number in their analysis of N-cycling in the Mississippi River Basin.

Many studies employ RTDs to analyze the influence of hyporheic exchange on nutrient and contaminant transport in the stream corridor. Recently, Grant et al. (2020b) unified two different descriptions for the unsteady transport of mass through the hyporheic zone by exchange across bedforms, namely, an advective pumping model (introduced by Elliott and Brooks (1997b)) and a one-dimensional dispersion model for which the dispersion coefficient decays exponentially with depth. In both cases, key quantities for water quality (e.g., the temporal evolution of mass concentration in the water column and interstitial fluids of the sediment bed, as well as the mass flux across SWI) can be obtained by convolving the time history of solute mass in the water column with either an RTD

(advective model) or Green's Function (dispersion model) that describe transport and mixing in the streambed.

Various studies have been performed to investigate the RTD of water undergoing hyporheic exchange through ripples and dunes. Boano et al. (2007) utilized the continuous random waking theory (CTRW) to represent the interactions between in-stream solute transport and the hyporheic exchange RTDs in an infinite sediment bed. In such systems, and in the absence of an imposed groundwater flow, hyporheic exchange across dunes results in a strongly and positively skewed (or "heavy tailed") RTD. This indicates that most water parcels transport through the hyporheic zone relatively quickly, while a minority of water parcels linger for a very long time. Horizontal groundwater flow induced by longitudinal pressure gradients (so-called underflow) can reduce the RTD's positive skewness and heavy tail (Bottacin-Busolin & Marion, 2010; Marzadri et al., 2016). Likewise, experimental (e.g., Fox et al., 2014) and modeling (Azizian et al., 2017; Cardenas & Wilson, 2006; Hester et al., 2013, 2019; Marzadri et al., 2016) studies indicate that vertical groundwater flow (in either gaining or losing configurations) can reduce hyporheic exchange flux and residence times in the hyporheic zone, and thereby diminish key ecological functions (such as respiration and nitrogen cycling) in streambed sediments (Gomez-Velez et al., 2014). Moreover, Tonina et al. (2016) demonstrated that sediment heterogeneity decreases the mean residence time, increases its median value, and increases the positive skewness of the RTD.

The existence of a shallow confining layer can limit the extent of the hyporheic zone, as well as alter the hyporheic RTD characteristics (e.g., Morén et al., 2017). Similarly, groundwater underflow affects the extend of the hyporheic zone and its RTD (Bottacin-Busolin & Marion, 2010; Marzadri et al., 2016), and the underflow velocity can also be used to represent the velocity of bedform migration (Bottacin-Busolin & Marion, 2010). Although a finite streambed depth has been considered in previous studies (e.g., Packman et al., 2000a), a systematic assessment of the relative alluvium depth to dune wavelength effect combined with variations in groundwater underflow on RTDs in the hyporheic zone of dune-covered streambeds has not been evaluated yet. On one hand, most hyporheic studies included either the presence of streambed depth (Marzadri et al., 2016) or underflow velocity (Boano et al., 2009; Cardenas & Wilson, 2006). The aim of this chapter is to address this knowledge gap by identifying appropriate analytical representations of the hyporheic zone RTD for various combinations of dimensionless streambed depths and underflow values.

The widely deployed Transient Storage model (TSM) (Bencala, 1983) implemented in the USGS OTIS package (Runkel, 1998), for example, assumes that the hyporheic zone

RTD can be represented by an exponential (EXP) distribution (Harvey & Gooseff, 2015). Although the applicability of an EXP distribution for the hyporheic zone RTD has been questioned (Knapp & Kelleher, 2020), Zaramella et al. (2003) claimed that it is a reasonable approximation for shallow beds. Other studies found that the RTD follows a power law tail (Cardenas, 2007; Haggerty et al., 2002; Kirchner et al., 2000; McGuire et al., 2005) for both homogeneous and heterogeneous sediment (Sawyer & Cardenas, 2009), and that this tailing behaviour is more persistent in regional and subregional flow systems (Cardenas, 2007). Over the years, other analytical distributions have been suggested for the hyporheic zone RTD, including the Gamma (GAM) (Kirchner et al., 2000), Lognormal (LN) (Marzadri et al., 2016; Wörman et al., 2002), and Fréchet (FR) (Grant et al., 2020b) distributions. In this study, we systematically evaluate the effect on RTDs of dimensionless sediment depth (i.e., sediment depth normalized by dune wavelength) combined with various groundwater underflow values, for hyporheic exchange induced by dune-like bedform. We investigate the conditions (combination of relative sediment depth and groundwater underflow) for which these four distributions (EXP, GAM, LN, and FR) apply, and we analyze the values of the distribution parameters that can be useful for different applications.

3.2 Methodology

Candidate analytical RTDs were evaluated for different sediment bed depths and underflow values in three steps. First, a particle tracking technique was used to generate empirical RTDs associated with bedform pumping through the hyporheic zone for 832 combinations of sediment bed depths and underflow values. Second, each of the four candidate analytical distributions (EXP, GAM, LN, and FR) were fitted to the empirical RTDs, and sets of RTD parameter values were inferred. Finally, for each considered combination used to generate, the four candidate analytical distributions were ranked in terms of their goodness of fit to the empirical RTDs using an Anderson-Darling test. Details for these three steps are described below.

3.2.1 Numerical Generation of Empirical RTDs

To simulate the advective flow field associated with hyporheic exchange through stationary bedforms, we adopted the analytical 2-D laminar flow model published by Packman et al. (2000a) and generalized by Boano et al. (2009), which is based on earlier analytical solutions of hyporheic exchange through streambeds by Elliott and Brooks (1997b) and Vaux (1968). These models posit a sinusoidal pressure variation over the sediment-water interface mimicking the static and dynamic pressure variations that develop on the surface of streambeds in a turbulent overlying flow (Cardenas et al., 2008), and assume isotropic and homogeneous hydraulic conductivity, constant sediment porosity and fluid density. A

so-called "Tóth domain" (Figure 3.1) (Frei et al., 2019; Tóth, 1962) was used here, including an impermeable lower boundary at depth d_b below the surface with underflow u_b and upwelling/downwelling groundwater velocity ($\pm v_g$, where $+$ indicates upwelling and $-$ refers to downwelling). The model in dimensionless form is written as:

$$u_d^* = -cos(x^*)\,[tanh(d_b^*)\,sinh(y^*)+cosh(y^*)] + u_b^*, \quad (3.1)$$

$$v_d^* = -sin(x^*)\,[tanh(d_b^*)\,cosh(y^*)+sinh(y^*)] \pm v_g^* \quad (3.2)$$

$$h_m = 0.28\,\frac{U^2}{2g} \begin{cases} \left(\frac{h_b/d}{0.34}\right)^{3/8} & H/d \le 0.34 \\ \left(\frac{h_b/d}{0.34}\right)^{3/2} & H/d \ge 0.34 \end{cases} \quad (3.3)$$

$$u_m = k\,K_c h_m\,tanh(db^*) \quad (3.4)$$

$$u_d^* = \frac{u_d}{u_m}, \quad (3.5)$$

$$v_d^* = \frac{v_d}{u_m}, \quad (3.6)$$

$$u_b^* = \frac{u_b}{u_m}, \quad (3.7)$$

$$v_g^* = \frac{v_g}{u_m}, \quad (3.8)$$

$$k = \frac{2\pi}{\lambda}, \quad (3.9)$$

$$x^* = k\,X, \quad (3.10)$$

$$y^* = k\,Y, \quad (3.11)$$

$$d_b^* = k\,d_b, \quad (3.12)$$

$$t^* = \frac{k u_m t}{\theta}, \quad (3.13)$$

where u_d and v_d are the horizontal and vertical Darcy fluxes, respectively, h_b is the bedform height, d is the stream depth, K_c is the hydraulic conductivity, u_m is the maximum Darcy flux at the sediment water interface (SWI), X and Y are the horizontal and vertical coordinates, d_b^* is the dimensionless sediment depth, λ is the bedform wavelength, k is the wavenumber of the bedforms, and θ is the sediment porosity. The vertical coordinate, Y, is centred at the SWI ($Y = 0$) and oriented upward, i.e., depth into the bed corresponds to negative values of Y. The range of d_b^* was chosen between 0.2 and 6.4 (deep enough to avoid affecting the hyporheic zone extent) consistently with published experimental studies performed with dune-like bedforms (Elliott & Brooks, 1997a; Marion et al., 2002;

Packman et al., 2000b, 2004; Packman & MacKay, 2003; Rehg et al., 2005; Ren & Packman, 2004). Similarly to Boano et al. (2009), the investigated range of u_b^* was between 0 (no underflow) to 5 (very large underflow) with intervals of 0.1 at $u_b^* < 1$, 0.2 for $1 > u_b^* > 3$, and 0.5 at $u_b^* > 3$. Due to the presence of the impervious sediment bottom at $Y = -d_b$, the effect of upwelling and downwelling groundwater was neglected ($v_g = 0$).

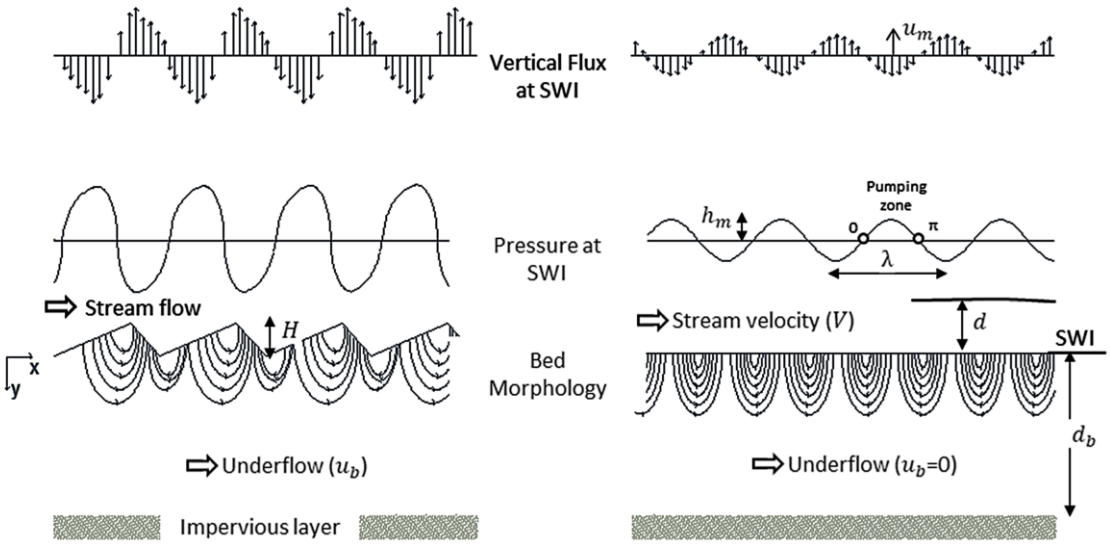

Figure 3.1: A) Representative diagram of a conceptual model representing hyporheic exchange below a dune-like bedform, with pressure head distribution and consequent upwelling and downwelling zones due to the dune morphology. B) Simplified analytical model represented by a Tòth domain with a sinusoidal pressure variation creating upwelling and downwelling zones.

The volumetric water flux predicted by Eq. (3.2) varies sinusoidally with horizontal distance along the SWI, forming well-defined upwelling and downwelling regions that are fully characterized by repeating unit cells (Elliott & Brooks, 1997b) (see Figure 3.1B). Thus, the RTD associated with the hyporheic flow field can be determined by tracking the arrival times of particles released in the downwelling zone of a single unit cell. Accordingly, we released 10000 particles in the downwelling zone ($0 \leq x^* \leq \pi$) with a flux-weighting scheme that generated a number of particles proportional to the local downwelling flux. The RTD for each combination of d_b^* and u_b^* was obtained by fixing the length of each particle step within the sediment domain ($\Delta s^* = k\Delta s = 2 * 10^{-3}$). Then, the *i*-th time step (Δt^*) was calculated as:

$$\Delta t_i^* = \frac{\Delta s^*}{\sqrt{u_{d_i}^{*2} + v_{d_i}^{*2}}}, \quad (3.14)$$

where $u_{d_i}^*$ and $v_{d_i}^*$ denote the velocity components at the particle location at the end of *i*-th step. For each particle, the time at the end of the *i*-th step (t_i^*) within the sediment bed domain ($y^* < 0$) is:

$$t_i^* = t_{i-1}^* + \Delta t_i^*, \ \ i = 1, \dots, N, \quad (3.15)$$

where $t_0^* = 0$, N is the number of steps undertaken by each particle, and the corresponding horizontal and vertical particle displacements (Δx_i^* and Δy_i^*, respectively) of the i-th step are:

$$\Delta x_i^* = u_{d_i}^* \Delta t_i^* \quad (3.16)$$

$$\Delta y_i^* = v_{d_i}^* \Delta t_i^* \quad (3.17)$$

For each combination of d_b^* and u_b^*, Cumulative Distribution Function (CDF) and probability density function (pdf) forms of the RTD were calculated from the observed residence times of the 10000 particles.

3.2.2 The Inference of the Analytical Distribution Parameters

Separate particle tracking RTDs were generated for 832 combinations of d_b^* and u_b^* over their previously mentioned ranges. Each of these RTDs was fitted to the four analytical distributions (EXP, GAM, LN, and FR, see Table 3.1 described earlier, using MLE method encoded in the Mathematica (Wolfram) software). EXP is characterized by a decreasing monotonic function and parametrized by a single parameter (ρ). The parameters for the GAM distribution, α and β, control the shape and scale characteristics of the distribution, respectively. The parameters of LN, μ and σ, determine the mean value and the standard deviation of the log-transformed random variable, respectively. Even though the FR distribution is a three-parameter distribution (shape parameter s, scale parameter q, and location parameter m), for the sake of parsimony and for consistency with the other distributions considered in this study, which have no more than 2 parameters, the FR distribution with two parameters was chosen by fixing the shape parameter ($s = 1$) as assumed by Grant et al. (2020b). To determine the ranking of these distributions according to their closeness to the empirical RTD from each particle tracking simulation, the candidate analytical distributions were ranked using the Anderson-Darling (AD) test (Anderson & Darling, 1952) that was created to detect sample distributions' departure from normality. The AD test was chosen because its precision in comparing distributions is superior to other goodness-of-fit tests (Engmann & Cousineau, 2011). This deviation between the empirical RTD and the tested distribution is denoted here as AD (lower AD value means closer analytical distribution to the empirical one), and it was calculated as follows:

$$AD = -n - {}^{1}/_{n} \sum_{i=1}^{n} (2i-1)[\ln F(X_i) + \ln(1 - F(X_{n+1-i}))] \quad (3.18)$$

where $(X_1 < \ldots < X_n)$ is the ordered (from smallest to largest) element sample of size n, and $F(X)$ is the tested analytical cumulative distribution to which the sample is compared. Then, the parameters of the analytical distributions were inferred for all d_b^* and u_b^* combinations.

The efficiency of each analytical distribution was tested through the AD criterion by calculating the relative error (RE) associated with estimating different percentiles of the RTD. Here, we used t^* corresponding to 20% ($t_{20\%}^*$), 50% ($t_{50\%}^*$), and 80% ($t_{80\%}^*$) of the flow paths have passed. Hence, RE is calculated as following:

$$RE_i = \frac{\left|t_{i_A}^* - t_{i_E}^*\right|}{t_{i_E}^*} \quad (3.19)$$

where i corresponds to different percentiles (20%, 50%, and 80%), A denotes the analytical distribution, while E is used to represent empirical distribution.

Table 3.1: A list of the adopted analytical distributions in this study with their associated pdf formulae and parameters.

Distribution	pdf	parameters
Gamma	$\frac{e^{-\frac{t^*}{\beta}} t^{*-1+\alpha} \beta^{-\alpha}}{\text{Gamma}[\alpha]} \quad t^* > 0$	α, β
Lognormal	$\frac{e^{-\frac{(-\mu+\text{Log}[t^*])^2}{2\sigma^2}}}{\sqrt{2\pi} t^* \sigma} \quad t^* > 0$	μ, σ
Fréchet	$\frac{e^{-\frac{q}{t^*-m}} q}{(t^*-m)^2} \quad t^* > m$	$s = 1, q, m$
Exponential	$\rho e^{-t^* \rho} \quad t^* \geq 0$	ρ

3.3 Results

3.3.1 Hyporheic Flow Paths

The results of the particle tracking simulations show that in case of semi-infinite bed with no underflow ($d_b^* \longrightarrow \infty, u_b^* = 0$), the exchanged water parcels infiltrate through the downwelling zone into the sediment forming two identical and symmetrical flow cells

(Figure 3.2A). The presence of underflow ($u_b^* > 0$) distorts the flow cells (Figure 3.2B), as u_b^* tends to displace the water parcels from the downwelling zone to the zone where $v^*$is positive (Boano et al., 2009). In addition, the existence of a confining layer (shallow d_b^*) reduces the extent of the hyporheic zone (Figure 3.2C), while the combined presence of both d_b^* and u_b^* results in shallow hyporheic zone with asymmetrical flow cells (Figure 3.2D). This hyporheic depth confinement was also observed when introducing groundwater gaining/losing conditions as well as sediment heterogeneity (Hester et al., 2013, 2019).

The hyporheic RTDs generated by the particle tracking algorithm (i.e., the empirical RTDs, see Methods) become progressively heavy tailed as the dimensionless depth increases from d_b^* = 0.2 to 6.4 (Figure 3.3A, direction of the black arrow). Increasing u_b^* has a similar effect to decreasing d_b^* (Figure 3.3B), especially for RTDs tails that represent the deep flow paths. Instead, the short residence times are more affected by u_b^* than d_b^* because underflow modifies the shape of the shallow flow paths, as explained before (Figure 3.2). For large values of d_b^*, the shape of the empirical RTD converges to the one of an infinitely deep bed (see RTDs for $d_b^* = 4, 5,$ and 6.4 in Figure 3.3A), consistently with previous results (Boano et al., 2009; Fox et al., 2014; Wörman et al., 2002).

3.3.2 Analytical Representation of the Empirical RTDs.

Figure 3.4 was produced based on the AD values and reports the distributions that fit better the empirical RTDs over the considered ranges of d_b^* and u_b^*. Because the RTD becomes progressively heavy tailed with increasing d_b^* and its shape changes over the range of u_b^*, no single analytical distribution can represent the empirical RTDs over the full ranges of d_b^* and u_b^* tested here (Figure 3.4A). According to the AD criterion, in case of negligible underflow ($u_b^* \leq 0.1$), the empirical RTD is best approximated by different analytical distributions over different sediment depth ranges, including: (1) GAM for shallow streambeds ($0 \leq d_b^* \leq 1.2$, Figure 3.4A); (2) LN for streambeds of intermediate depth ($1.2 < d_b^* < 3.2$, Figure 3.4A); and (3) FR for deep streambeds ($d_b^* > 3.2$, Figure 3.4A). On the other hand, for $u_b^* > 0.1$ the best fitting analytical distribution switches between GAM and LN (Figure 3.4A). Specifically, for $0.1 < u_b^* < 0.8$, LN is identified as the best fitting distribution for nearly all d_b^* cases, as LN better fits the heavy tail of the empirical distribution. However, at $u_b^* > 0.8$ the heavy tail progressively disappears (see examples in Figure 3.3), and GAM becomes the best fitting distribution (Figure 3.4A).

In some cases, the second-best fitting distribution can also provide a reliable representation of the empirical RTD. Therefore, the map of surrogates for the best fitting

distribution (i.e., the second-best fitting distribution according to AD criterion) is presented in Figure 3.4B. Overall, these surrogates vary between GAM and LN based on the specific values of d_b^* and u_b^*, except for $u_b^* \leq 0.2$ and in relatively deep streambeds ($d_b^* \geq 2.2$) when LN and FR switch roles between the best fitting distribution and the second best (surrogate) (Figure 3.4). Finally, for $u_b^* = 0.3$, EXP behaves as a better surrogate than GAM, which is classified as the third-best fitting distribution with minimal difference with EXP according to the AD criterion.

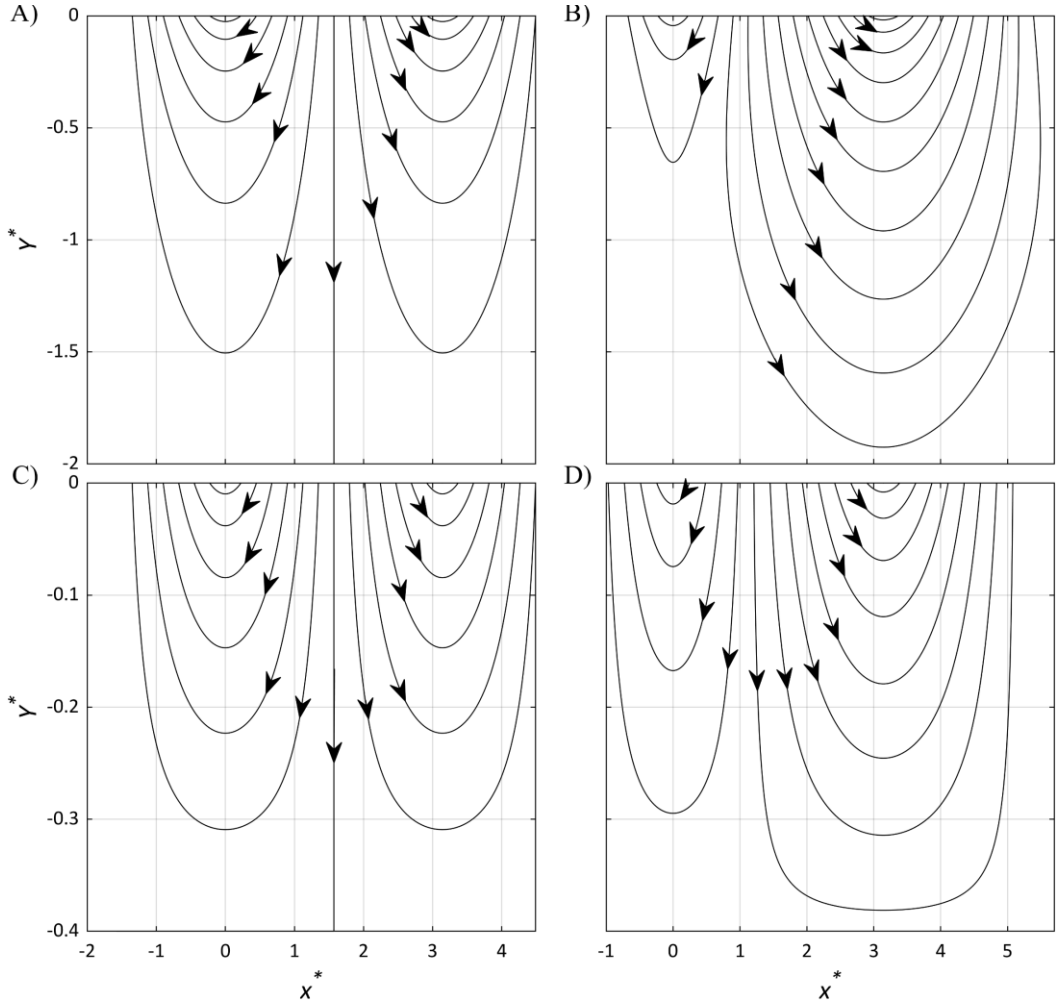

Figure 3.2: Pathlines induced by dune morphology in different combinations of d_b^* and u_b^*;(A) $d_b^* \to \infty$ and $u_b^* = 0$, (B) $d_b^* \to \infty$ and $u_b^* = 0.4$, (C) $d_b^* = 0.4$ and $u_b^* = 0$, (D) $d_b^* = 0.4$ and $u_b^* = 0.4$.

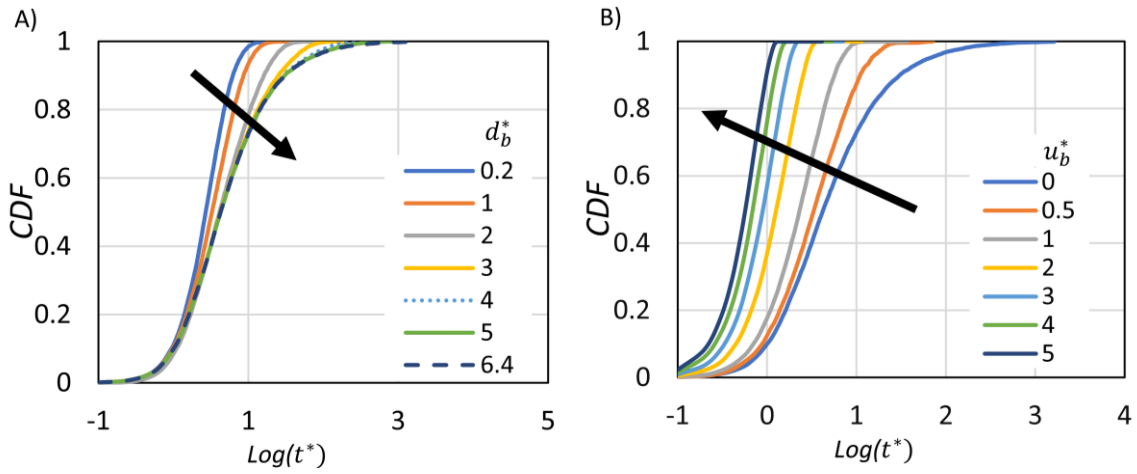

Figure 3.3: The effect of different values of (A) d_b^* and (B) u_b^* on empirical CDF. The black arrow shows the direction of d_b^* increase (A) and u_b^* increase (B). The black arrows in (A) and (B) indicate the increase in d_b^* and u_b^*, respectively.

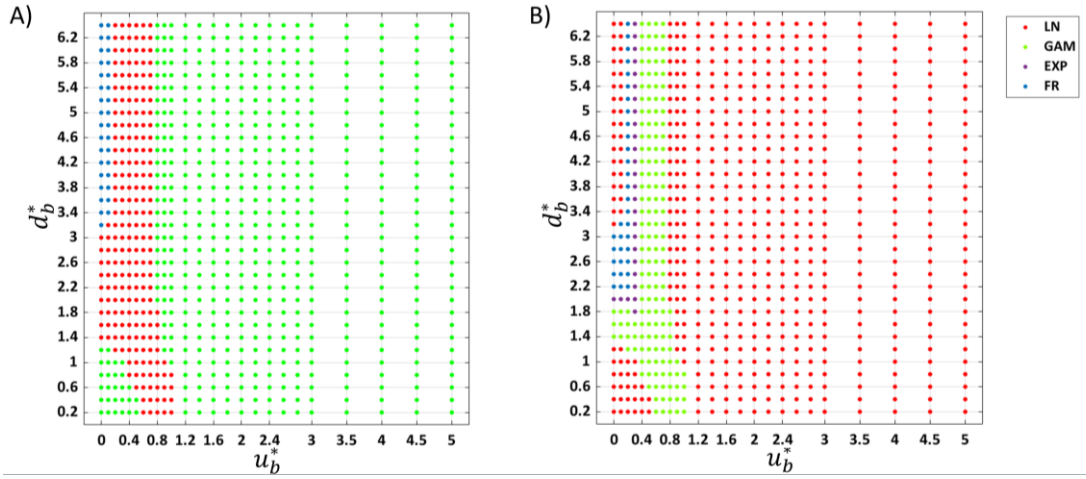

Figure 3.4: Maps of (A) best and (B) second best analytical representative at different combinations of d_b^* and u_b^*.

Figure 3.5 shows that the best fitting analytical distributions reproduce remarkably well the empirical distributions for different combinations of d_b^* and u_b^*. The relative errors (RE) for different CDF percentiles ($t_{20\%}^*$ in Figure 3.5A, $t_{50\%}^*$ in Figure 3.5B, and $t_{80\%}^*$ in Figure 3.5C) are always less than 10%. Similarly, the second-best fitting distribution can fit the empirical CDFs reasonably good, as the RE is very low for $t_{20\%}^*$ (less than 12%, Figure 3.6A), and low ($< 21\%$) for the other two percentile ($t_{50\%}^*$ and $t_{80\%}^*$).

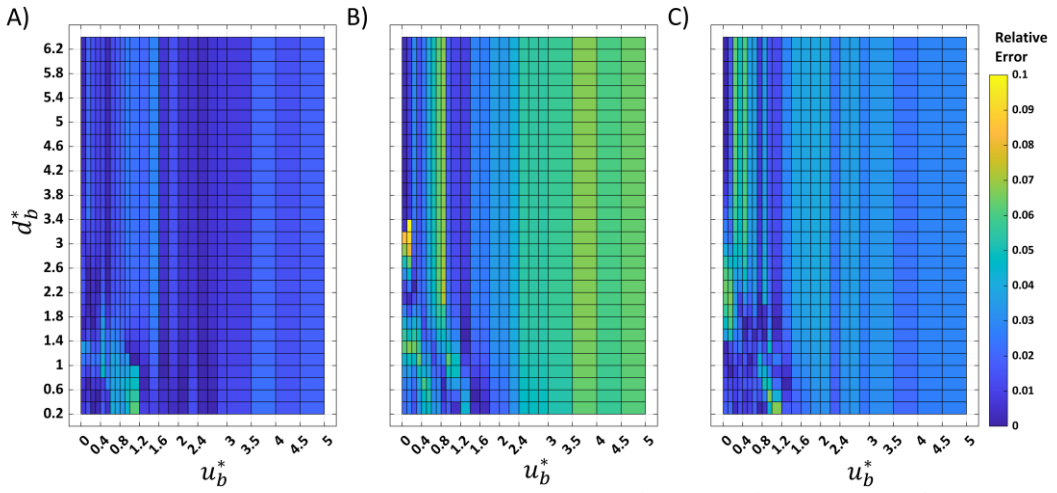

Figure 3.5: The relative error associated with estimating (A) $t^*_{20\%}$, (B) $t^*_{50\%}$, and (C) $t^*_{80\%}$ by applying Eq. (3.19) on the best analytical distributions to represent the empirical CDF (Figure 3.4A).

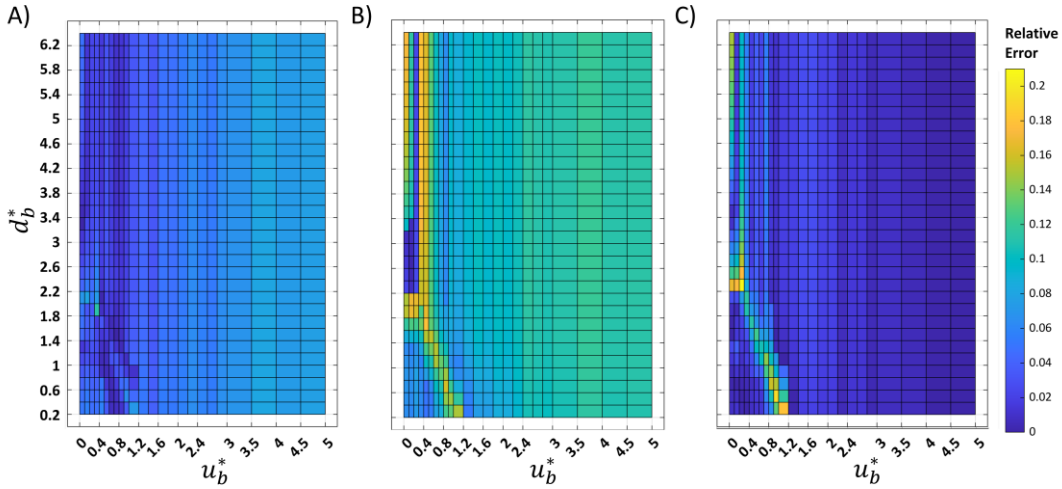

Figure 3.6: The relative error associated with estimating (A) $t^*_{20\%}$, (B) $t^*_{50\%}$, and (C) $t^*_{80\%}$ by applying Eq. (3.19) on the second-best analytical distributions to represent the empirical CDF (Figure 3.4B).

3.3.3 Inferring the Parameters of the Analytical distributions

The parameter values fitted for each distribution vary with d_b^* and u_b^* (Figure 3.7). For EXP, ρ slightly decreases with d_b^* and increases with increasing u_b^* (Figure 3.7A). For GAM, α decreases and β increases with higher d_b^* and lower u_b^* (Figure 3.7B), as the distribution shape shifts from unimodal to monotonically decreasing. For LN, both μ and σ increase as the thickness of the tail increases to describe longer t^* at higher d_b^* and lower u_b^* values (Figure 3.7C) Lastly, for FR, q increases and m decreases (Figure 3.7D) for higher d_b^* and lower u_b^*, as the distribution flattens and its peak shifts towards longer t^*. For all distributions, the parameters attain constant values for deep streambeds as well as for strong underflow.

3.4 Application for Estimating the Damkhöler Number.

The wide spatial and temporal scales of the hyporheic zone affect its associated characteristics (residence times, reaction times, and exchange rate) that affect its ability to process nutrients (Harvey et al., 2013) . Gomez-Velez et al. (2015) used a quantity called Reaction Significance Factor (RSF) (Harvey et al., 2013) to evaluate the residence time/exchange rate trade‐off for aerobic respiration and denitrification in the Mississippi River Network. In this framework, more nutrients are removed from the hyporheic zone when the residence time is comparable to the reaction time and the uptake length is shorter than the reach length so the water parcel can circulate many times through the reach. The component that compares the residence time to the reaction time in this framework is called the Damköhler number (Da), which is utilized by different models to delineate the boundary between aerobic and anerobic conditions that define the hyporheic zoen as either a source or sink for the nutrients (Zarnetske et al., 2012). It is defined as the ratio between the median hyporheic residence time ($t^*_{50\%}$) and the characteristic time necessary for oxygen consumption that was used in unidimensional form by applying Eq. (3.13) ($\tau^*_{rp} = ku_m\tau_{rp}/\Theta$). At $Da_{rp} = t^*_{50}/\tau^*_{rp} < 1$, the residence times of water parcels are less than the reaction time needed for oxygen consumption, aerobic conditions are dominant and denitrification is inhibited, while at $Da_{rp} >> 1$, oppositely, anaerobic conditions prevail and denitrification is likely (i.e., provided that the other two requirements; the presence of nitrate and labile organic matter, are satisfied) (Zarnetske et al., 2012). When flow paths exhibit residence times longer than a characteristic denitrification timescale used in unidimensional form ($\tau^*_{dn} = u_m\tau_{dn}/\theta$), they tend to be fully anaerobic, and all or most of the nitrate is removed ($Da_{dn} = t^*_{50}/\tau^*_{dn} >> 1$). Gomez-Velez et al. (2015) utilized a limited number of reported measurements in literature for different streams with different morphological and geometrical characteristics to proposed reasonable values for τ_{rp} and τ_{dn}. They found that τ_{rp} typically varies from 0.5 h to 10 h with median of 1 h, and τ_{dn} typically varies from 0.5 h to 100 h with median of 10 h. For simplicity, as determining τ_{rp} and τ_{dn} is not the main focus of this study, these median values for τ_{rp} and τ_{dn} were used in determining Da_{rp} and Da_{dn}, respectively. Correctly representing the residence timescales in the hyporheic zone can help in accurately determining the Damköhler numbers for aerobic respiration and denitrification. This leads to more accurate assessments of the link between the hyporheic zone RTD and key ecological functions, such as stream metabolism, generally, and denitrification, in particular (Mulholland et al., 2009).

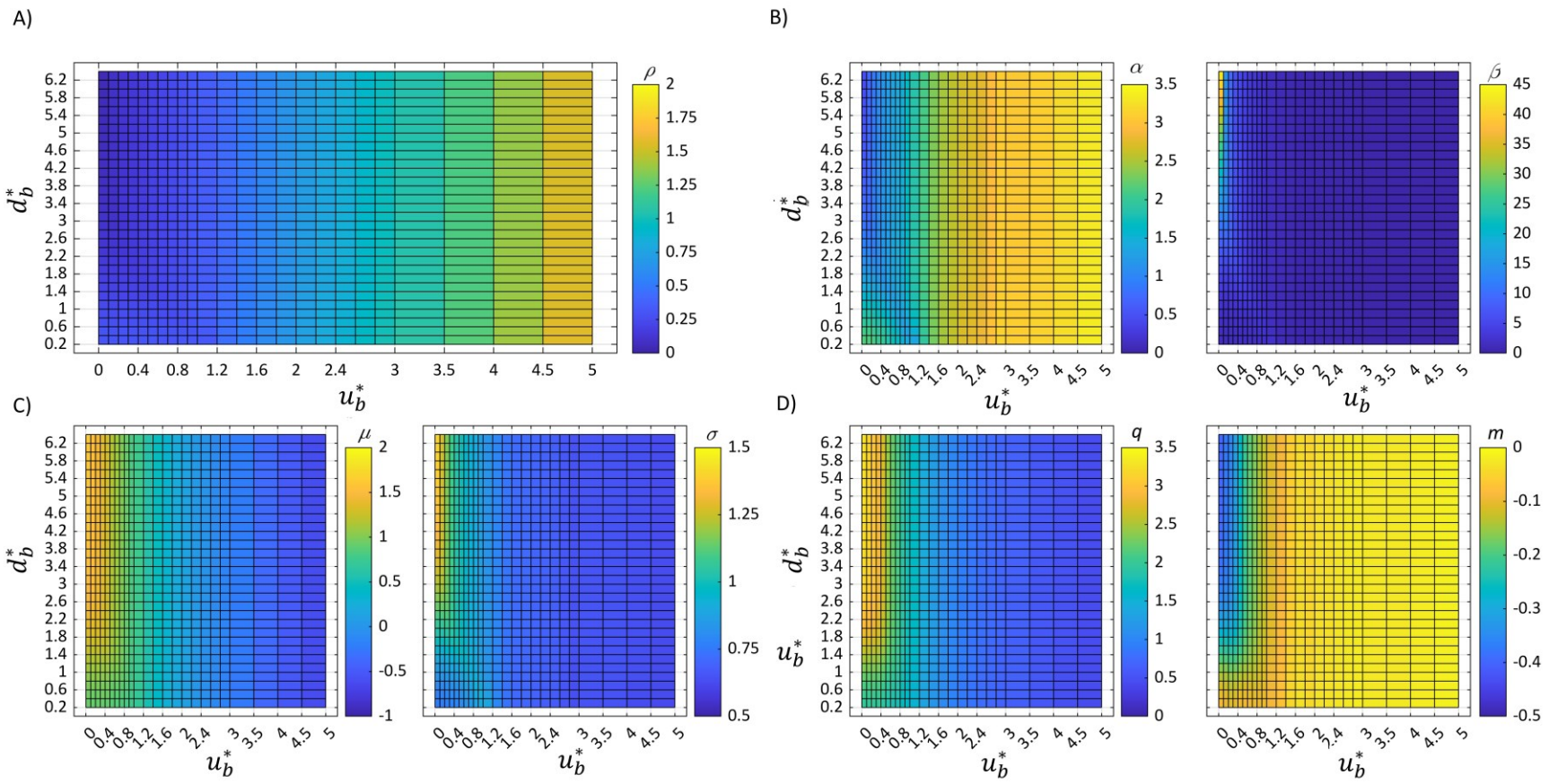

Figure 3.7: Maps showing the parameters values for the four analytical distributions tested in this study ((A) EXP, (B) GAM, (C) LN, and (D) FR) at different combinations of d_b^* and u_b^*.

The hydraulic and morphological properties of the Embarras River (Table 3.2) located 15 km south of Urbana-Champaign, east-central Illinois, USA (Sukhodolov et al., 2006) was adopted here. This river was chosen because dune-like bedforms are its predominant morphology. It is used only as an application to show how the analytical distributions resulted from the comparison between the empirical RTDs and the four tested analytical distributions (EXP, GAM, LN and FR) (see section 3.3.2) can be applied for predicting Da, and consequently, the nitrification-denitrification zones. Therefore, Da_{rp} and Da_{dn} where calculated using $t^*_{50\%_E}$ ($t^*_{50\%}$ based on the empirical CDF), and then compared to $t^*_{50\%_A}$ ($t^*_{50\%}$ based on the analytical distributions (EXP, GAM, LN and FR)). The properties of the Embarras River were used to normalize the respiration and denitrification time scales (τ_{rp}~1h and τ_{dn}~10h, respectively).

Table 3.2: Embarras River properties used for normalizing the respiration and denitrification time scales. † Porosity was obtained from Figure 5 in Urumović and Urumović Sr (2014) by considering the referential grain size = D_m. ‡ The hydraulic conductivity was calculated with the Kozeny–Carman equation.

Embarras River Properties

mean grain size (D_m)	$1\ mm$
stream depth (d)	$0.35\ m$
mean stream Velocity (U_{mean})	$0.44\ m/s$
Dune wavelength (λ)	$1\ m$
Dune height (H)	$0.1\ m$
Dune roughness (H/d)	0.29
Porosity (θ) †	0.32
Hydraulic conductivity (K_c) ‡	$4.4 * 10^{-3}\ m/s$

For different d^*_b and $u^*_b = 0$, the empirical Da_{rp} and Da_{dn} (Da_{EMP}, asterisks in Figure 3.8) were calculated as the ratio between the empirical $t^*_{50\%_E}$ and the normalized respiration and the denitrification time scales τ^*_{rp} and τ^*_{dn}. The corresponding Da_{rp} and Da_{dn} were calculated for each one of the four analytical distributions (Da_{EXP}, Da_{GAM}, Da_{LN}, Da_{FR}), and then compared to Da_{EMP} that is estimated using the empirical RTD (Figure 3.8). It should be noticed that Da_{rp} and Da_{dn} are simply proportional to each other by one order of magnitude (see vertical axes in Figure 3.8), as they differ only by the reaction timescales. Therefore, the comparison between empirical and analytical representations of Da does not depend on the specific reaction considered.

Damkhöler numbers generated from the empirical RTD (Figure 3.8) decline more-or-less monotonically with increasing dimensionless streambed depth. This pattern is best represented by GAM for $d_b^* < 1.2$, and by FR over the full range of d_b^* evaluated here. The LN and EXP distributions under- and over-estimate Da for dimensionless depths $d_b^* < 1.0$ and $d_b^* > 1.0$, respectively. This result-that FR provides the best estimate of the Damkohler Number over the two-order of magnitude change in dimensionless sediment bed depth evaluated here-is surprising given that this analytical distribution is not the best representation of the empirical RTD for $d_b^* < 3.2$ (see above). The explanation is that, even for shallow depths, the optimized CDF of FR intersects the empirical CDF at the 50% percentile across all dimensionless depth ranges evaluated here. Hence, the analytical distribution's estimate for $t_{50\%}^*$, and hence the Damköhler number, is accurate, even for shallow bed depths, where FR is a relatively poor representation of the empirical RTD.

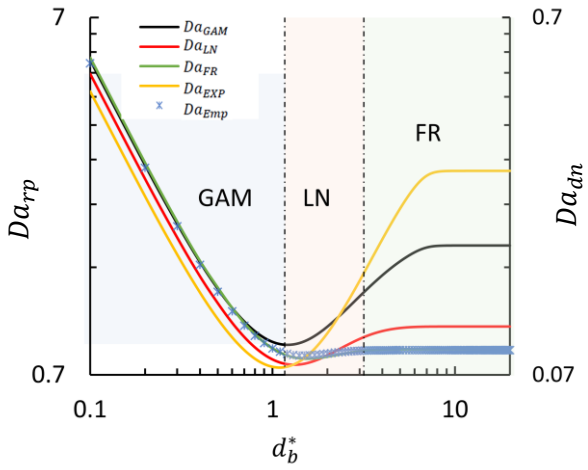

Figure 3.8: Comparison between the Damköhler number of respiration and denitrification (Da_{rp} and Da_{dn}, respectively) calculated at different d_b^* from the empirical RTD (Da_{Emp}), and the ones calculated by different analytical representations (Da_{GAM}, Da_{LN}, Da_{FR}, and Da_{EXP}).

3.5 Discussions

The hyporheic flow paths tend to extend vertically below dune-like bedforms to an extent comparable to dune wavelength (e.g., Boano et al., 2009; Fox et al., 2014; Marzadri et al., 2016). They form two symmetric cells in which the flow paths infiltrate in the pumping zone and exfiltrate in zones of low-pressure head (Figure 3.1). When flow paths infiltrate freely into the sediment, their RTDs are characterized by a heavy tail which accounts for the very deep flow paths which stay for longer RTs within the sediment. Introducing a

confining effect to the extent of the hyporheic zone prevents some of the flow paths from infiltrating deeper in the sediment. Therefore, the heavy tail of the RTD is partially cut off. The groundwater underflow affects not only the deep flow paths but also it deforms the shallow ones (compare different panels in Figure 3.2). This horizontal groundwater flow that is mathematically equivalent to the effect of a bedform migrating with velocity u_b^* limits the thickness of the hyporheic zone. Consequently, it reduces the RTD's positive skewness and heavy tail (Bottacin-Busolin & Marion, 2010).

Both the best and second-best analytical representatives of the empirical RTD perform relatively well (Figures 3.53.6 and 3.6), and the difference between them is small (<20% in general, and <10% in most cases) (Figure 3.9). Therefore, in general, over the whole range of d_b^* and u_b^*, LN can be used to represent the RTD, as it is always either the best or the second-best representative (Figure 3.4) and it performs considerably well in fitting the empirical RTD in different cases. This finding is in agreement with many of previous studies (e.g., Cardenas et al., 2008; Marzadri et al., 2016; Wörman et al., 2002) which suggested that LN can be used to represent RTD in dune-like bedforms. In addition, and in agreement with (Kirchner et al., 2000), GAM also appears to be a good surrogate for most of the cases (Figure 3.4) as it represents very well the RTD compared to FR and EXP and in some cases even to LN. This good performance is found, especially, when the hyporheic zone is confined by either streambed depth (shallow d_b^*) or strong underflow/fast moving bedform (high u_b^*). On the other hand, when the hyporheic zone extends more deeply in the sediment (deep d_b^* or low u_b^*), FR is identified as a better representative for the RTDs than GAM. FR works relatively well for deep d_b^* and low u_b^* (Figure 3.4), as this distribution is usually used to represent extreme events (Ramos et al., 2017) whose distributions are usually characterized by a very long tail after a relatively flat peak. This agrees with the findings of (Grant et al., 2020b), who also pointed out that LN cannot be used in their coupled advective-dispersive model framework because it cannot be Laplace transformed. For this purpose, GAM and FR, which can both be Laplace transformed, can be used as an alternative to LN depending on the combination of d_b^* and u_b^* (Figure 3.4).

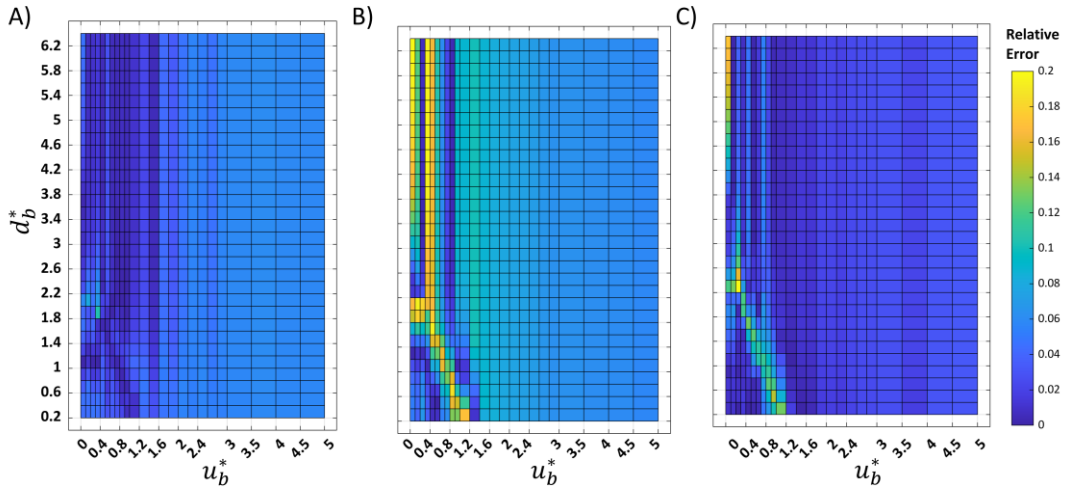

Figure 3.9: Difference between relative errors associated with the best analytical representation (Figure 3.5) and the second-best one (Figure 3.6) for (A) $t^*_{20\%}$, (B) $t^*_{50\%}$, and (C) $t^*_{80\%}$.

Contrary to previous reports (e.g., Zaramella et al., 2003), the EXP distribution appears to be a poor representation of the empirical RTD across most of the cases tested in this study. It can acceptably simulate the RTD tails in some cases for low u_b^* values (Figure 3.4B). However, for higher values of u_b^*, EXP does not accurately describe neither the short residence times (because of the RTD skewness) nor the long residence times (because it is characterized by a longer tail).

An application of the results of our study is the prediction of the Damkölher number using the predicted residence time form the best analytical RTD. This approach allows analytical distributions to be employed in modeling frameworks such as the advective-diffusive model introduced by Grant et al. (2020b), for which the ranking we provide here is important to choose a representative RTD that can be Laplace transformed. In general, the availability of an analytical expression of RTDs for different combinations of d_b^* and u_b^* can foster the future modeling studies of the hyporheic zone.

3.6 Conclusion Remarks

The hyporheic zone RTD associated with bedform pumping below dune-like bedforms is well represented by specific analytical distributions depending on the values of dimensionless streambed depth (d_b^*) and underflow velocity (u_b^*). From an Anderson-Darling (AD) ranking of these distributions we found that the empirical RTD is generally well represented by Lognormal and Gamma distributions, except for some cases in which Fréchet distribution performs better. Usually, the Fréchet distribution is more accurate for

deep $d_b^* > 3.2$ with very low underflow ($u_b^* \leq 0.1$), while LN, generally, works better for low u_b^* values ($0.1 < u_b^* < 0.8$) and Gamma performs better for large u_b^* values (> 0.8). Even though Fréchet cannot capture the whole shape of the RTD in shallow beds with no underflow, it accurately represents the median residence time, $t_{50\%}^*$, and it therefore provides the best representation of the Damköhler number over > 2 orders of magnitude of streambed depths even when $u_b^* = 0$. In most cases, Lognormal and Gamma can be equivalently employed as they are classified as either the best or the second-best representations of the empirical RTD. The availability of analytical distributions can be useful for modeling studies of nutrient dynamics to avoid the necessity of numerical simulations of hyporheic flow. Therefore, the results presented in this study can prove useful for modelling hyporheic exchange in dune-like bedforms and assessing nutrient processing in the hyporheic zone.

Chapter 4
Diffusive Description of Vertical Mixing in the Benthic Biolayer for Different Stream Morphology.

4.1 Introduction

Mass transport at the SWI has been investigated for decades, and diffusive approaches have been proposed as an attempt to quantify solute exchange (Grant et al., 2012; Grant et al., 2020a, 2020b; O'Connor & Harvey, 2008). A seminal model based on the concept of diffusive boundary layer (DBL), a thin layer close to the wall where molecular diffusion is dominant, was used to explain the transport process. However, this model has been developed assuming a smooth boundary layer, and therefore, its applicability to rough boundaries is questionable (Jørgensen & des Marais, 1990). Moreover, this model does not seem to fully represent mass transport through the SWI, as the exchange rates are large and cannot be explained only by molecular diffusion, also these exchange rates demonstrate a strong dependence on the turbulence structures (Hondzo et al., 2005; Lorke et al., 2003; O'Connor & Harvey, 2008). Since then, many empirical formulae were introduced to unravel the correlation between the controlling parameters of the transport process, and sediment characteristics and the hydrodynamics of the overlying flow. Elliott and Brooks (1997b) suggested that the effective diffusion from the water column into sediment with ripples and dunes (D_{eff}) is controlled by sediment porosity, hydraulic conductivity, and the half amplitude of the hydraulic head variations at the SWI, that in turn depends on the water column depth and velocity as well as on the bedform height. Instead, Packman and Salehin (2003) found a scaling relationship between D_{eff} and Reynolds number and the mean sediment diameter. Furthermore, based on meta-analysis including many laboratory experiments with different morphologies, O'Connor and Harvey (2008) proposed a formula to estimate D_{eff} depending on the shear Reynolds number and the permeability based Péclet number. Grant et al. (2012) later replaced this formula with a new one that

considers the effect of sediment porosity, sediment bed depth, and permeability Reynolds number. Moreover, Voermans et al. (2018) also proved experimentally that the permeability Reynolds number plays a significant role in defining the exchange process at the SWI. In addition, different experimental studies (Hester et al., 2021; Santizo et al., 2020) have been performed to investigate different hydraulic (infer also morphological) factors effect on the mixing (benthic) layer characteristics (e.g., thickness).

All of the above-mentioned empirical formulae were based on assumptions that (1) the diffusivity is constant over the whole sediment depth and (2) simplifying exchange between the water column and the interstitial fluid as a one-way coupling, i.e., the variations of interstitial concentration do not affect the water column concentration. Grant et al. (2020a) relaxed both these assumptions by (1) trying different diffusivity profiles to represent the decay of diffusion within the sediment domain and (2) building a one-dimensional model that fully couples the water column with the sediment domain. Grant et al. (2020a, 2020b) tested this model with the data from a stirred tank experiment (Chandler et al., 2016) and to bedform experiments (Elliott & Brooks, 1997a). The results showed that considering an exponentially decaying diffusion coefficient with depth better represents the transport process through the SWI and within the sediment than a constant diffusion coefficient. Testing the applicability of this model to different experimental configurations with different morphologies is necessary for its validation.

In this chapter, we performed a meta-analysis by applying the model of Grant et al. (2020a,, 2020b) for flat beds and dunes to a set of 127 published experiments for different morphologies. For each experiment, the effective diffusion at the SWI ($D_{eff,0}$) and the inverse mixing depth (decay coefficient of the exponential profile, α) were calculated for the exponential diffusivity profile. A machine learning algorithm (CART) and multiple linear regression technique (MLR) were then applied to develop robust predictive formulae to estimate dependence of $D_{eff,0}$ and α on the water column, sediment, and morphological characteristics. Also, the effect of different morphological configurations on the transport process is discussed.

4.2 Methodology

4.2.1 The Diffusivity Model Framework

The derivation of the mathematical framework of the diffusivity model is provided in APPENDIX A. This framework was introduced, first, by Grant et al. (2020a) for a flat bed

and extended to be coupled with the advective model for bedforms in Grant et al. (2020b). The novelty of this framework lies in accounting for the two-way feedback between solute concentration in the sediment and in the water column (Eq. (A.16a) in APPENDIX A). This means that the variation in solute concentration in the water column influences the concentration in the sediment and vice versa. In addition, different concentration profiles can be plugged into the model to simulate the concentration variation over the sediment depth. In this study, we adopted the constant profile (C profile; the solute concentration is constant over the sediment depth (d_b)) and the exponential profile (E profile; The solute concentration decays exponentially over the sediment depth). The constant profile function is represented as $f(\overline{y}) = 1$, while for the exponential profile, $f(\overline{y}) = e^{-\overline{y}}$, where $\overline{y} = ay$, as a is the inverse-decay coefficient of the exponential function ($a = 0$ for C profile), and y is the vertical axis in the sediment domain ranges from 0 to d_b. The profile functions were Laplace transformed for C profile (Eq. (4.1)) and for E profile (Eq. (4.2)) in order to be plugged into the governing equations of solute concentration variation in the water column (Eq. (4.3)) and in the sediment (Eq. (4.4)) as a Green function G.

$$G(\overline{y}, \overline{s}) = e^{-\overline{y}\sqrt{\overline{s}}} \quad (4.1)$$

$$G(\overline{y}, \overline{s}) = \frac{\sqrt{e^{\overline{y}}}\, K_1(2\sqrt{\overline{s}e^{\overline{y}}})}{K_1(2\sqrt{\overline{s}})} \quad (4.2)$$

$$C_w(\bar{t}) = (C_{w0} - C_{s0})\mathcal{L}^{-1}\left[\frac{1/\bar{s}}{1 - \frac{1}{\bar{s}\overline{h_w}(\frac{\partial G}{\partial \overline{y}})_{\overline{y}=0,\bar{s}}}}\right] + C_{s0} \quad (4.3)$$

$$C_s(\bar{y}, \bar{t}) = (C_{w0} - C_{s0})\mathcal{L}^{-1}\left[\frac{G(\bar{y},\bar{s})/\bar{s}}{1 - \frac{1}{\bar{s}\overline{h_w}(\frac{\partial G}{\partial \overline{y}})_{\overline{y}=0,\bar{s}}}}\right] + C_{s0} \quad (4.4)$$

where $\mathcal{L}^{-1}$ is the inverse Laplace transform operator, $\bar{s} = s\, t_T$ is the dimensionless Laplace variable, $\bar{t} = t/t_T$ is the normalized timescale, and $t_T = 1/D_{eff,0}a^2$ is a characteristic transport timescale, $\overline{h_w} = a\, h_w/\theta$ is the dimensionless water column depth, h_w is the water column depth, and θ is the sediment porosity.

The temporal dimensional flux at the SWI per unit bed area ($J(t)$) can be derived from Fick's law for both the C profile (Eq. (4.5) and the E profile (Eq. (4.6)).

$$J(t) = -\theta\, D_{eff,0} \frac{\partial}{\partial y} c_s(y,t)\Big|_{y=0} = -\theta C_{S0} \sqrt{\frac{D_{eff,0}}{\pi\, t}} \quad (4.5)$$

$$J(t) = -\theta\, D_{eff,0} e^{-ay} \frac{\partial}{\partial y} c_s(y,t)\Big|_{y=0} = -\theta\, D_{eff,0}\, \frac{a\, C_{s0}}{2} \left(1 + \mathcal{L}^{-1}\left[\frac{K_0(2\sqrt{\bar{s}}) + K_2(2\sqrt{\bar{s}})}{\sqrt{\bar{s}}\, K_1(2\sqrt{\bar{s}})}, \bar{s}, t\, D_{eff,0}\, a^2\right]\right) \quad (4.6)$$

Where K_0, K_1 and K_2 are the modified Bessel function of first, second and third kind, respectively.

For the C profile (Figure 4.1A), the experimental data are used to infer only one parameter ($D^C_{eff,0}$); however, for the E profile (Figure 4.1B) two parameters ($D^E_{eff,0}$ and a) are needed to fit the data.

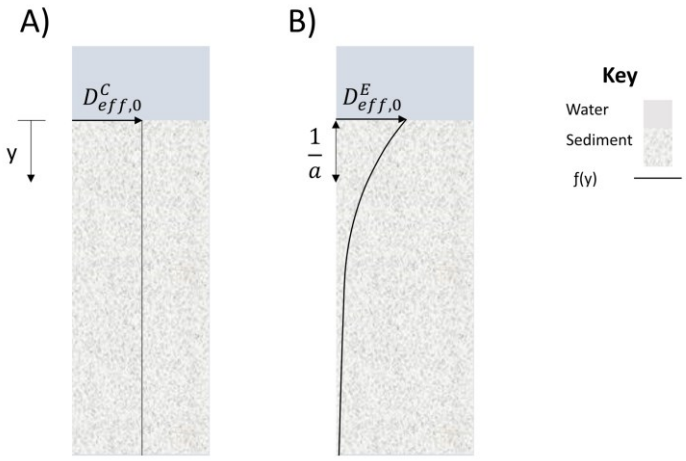

Figure 4.1: The constant profile (A) vs the exponential profile (B). y is the vertical axis into the sediment domain, $D^C_{eff,0}$ and $D^E_{eff,0}$ are the effective diffusivity at the SWI for Constant and exponential profile, respectively. a is the decay coefficient of the exponential profile.

4.2.2 Dataset Description

The developed model was applied to measurements obtained from 11 studies in the literature (Table 4.1), which conducted many laboratory experiments (127 experiments). These studies were conducted in various bed morphology configurations; flat beds (76 experiments), ripples and dunes (39 experiments), and alternate bars (12 experiments). All experiment were performed in flumes except for Chandler's who investigated the mixing using a stirring tank technique. In some experiments, a conservative tracer was added first to the water column ($C_{w0} > 0$ and $C_{s0} = 0$) till it mixes and then diffuses to the sediment domain (Chandler et al., 2012), in others, the tracer was added first to the sediment domain

($C_{s0} > 0$ and $C_{w0} = 0$). Different measurements were recorded in these experiments: the temporal variations of concentration in the water column $C_w(t)$, or the temporal variation of flux out of SWI $J(t)$ (Table 4.1).

Table 4.1: The list of considered experiments in this study with their morphology types and initial conditions of solute concentration in the water column and. The initial conditions in these experiments differ by either introducing the solute tracer in the water column ($C_{w0} > 0$) or in the sediment ($C_{s0} > 0$). Experiment technique indicates wether the expreriment was conducted using a recirculating flume or a strirring tank. Some studies reported the temporal variation of solute flux out of the sedimentbed ($J(t)$), others reported either the temporal variation of solute concentration in the water column ($C_w(t)$) or in the sediment ($C_s(t)$).

Study	*Morphology Type*	*Initial conditions*	*Experiment technique*	*Reported results*
(Richardson & Parr, 1988)	Flat bed	$C_{s0} > 0, C_{w0} = 0$	Recirculating Flume	$J(t)$
(Chandler et al., 2016)	Flat bed	$C_{s0} > 0, C_{w0} = 0$	Stirring Tank	$C_s(t)$
(Lai et al., 1994)	Flat bed	$C_{s0} > 0, C_{w0} = 0$	Recirculating Flume	$J(t)$
(Packman et al., 2004)	Flat bed & Bedforms	$C_{s0} = 0, C_{w0} > 0$	Recirculating Flume	$C_w(t)$
(Elliott & Brooks, 1997a)	Bedforms	$C_{s0} = 0, C_{w0} > 0$	Recirculating Flume	$C_w(t)$
(Packman et al., 2000b)	Bedforms	$C_{s0} = 0, C_{w0} > 0$	Recirculating Flume	$C_w(t)$
(Packman & MacKay, 2003)	Bedforms	$C_{s0} = 0, C_{w0} > 0$	Recirculating Flume	$C_w(t)$
(Ren & Packman, 2004)	Bedforms	$C_{s0} = 0, C_{w0} > 0$	Recirculating Flume	$C_w(t)$
(Rehg et al., 2005)	Bedforms	$C_{s0} = 0, C_{w0} > 0$	Recirculating Flume	$C_w(t)$
(Eylers, 1994)	Bedforms	$C_{s0} = 0, C_{w0} > 0$	Recirculating Flume	$C_w(t)$
(Tonina & Buffington, 2007)	Alternate bars	$C_{s0} = 0, C_{w0} > 0$	Recirculating Flume	$C_w(t)$

4.2.3 Classification and Regression Tree (CART) Analysis

CART algorithm is a robust machine learning method to build predictive models using a dataset (Loh, 2011). This technique was used here to correlate the controlling parameters (D_{eff0} and a for E profile) to the stream and sediment characteristics and the morphology type.

All the parameters considered to construct this correlation are presented in Figure 4.2. For the flat bed experiments, the bedform height h_b was assumed to the geometric mean of the sediment particle size (d_g), as both parameters represent the bed roughness. While the bedform wavenumber ($W_n = 2\pi/\lambda$, where λ indicates bedform length) was assigned as zero for flat bed experiments, as $\lambda \longrightarrow \infty$ for flat bed. All the included parameters in the CART were first log transformed, as they differ between them in many orders of magnitude. The RPART package in R was used with implementing the ANOVA method with Gini index to measure nodes impurity. The dataset was divided into 10 subsets to perform the training and cross-validation on the same dataset. To avoid overfitting of our data, the trees were pruned using a complexity parameter (CP) that compares the tree complexity, based on the number of splits, versus the cross-validation error (x-val). For the sake of parsimony, the smallest tree with high accuracy and acceptable error (minimum of x-val + standard error) was adopted here rather than using the best fitting tree at the lowest x-val.

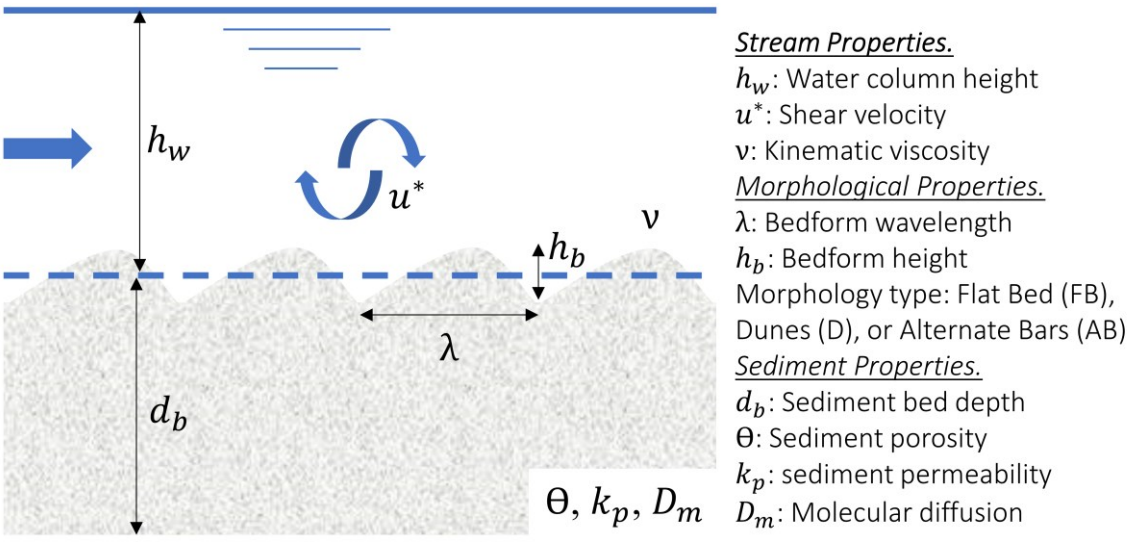

Figure 4.2: The stream, morphological, and sediment properties included in the CART analysis.

This technique was used in our study as a preparation to construct predictive equations for D_{eff0} and a by using the Multiple Linear Regression (MLR) technique on the parameters resulting from the smallest regression trees.

4.2.4 Multiple Linear Regression (MLR)

The MLR correlates the dependent variables (Y_i) to the independent variables (X_i) in a general form:

$$Y_i = f(X_1, X_2, X_3, \dots), \qquad (4.7)$$

where Y_i and X_i could be in either dimensional or dimensionless form.

When a power law correlation is assumed, Eq. (4.7) takes on the following form after being log transformed:

$$\log(Y_i) = A + B\ log(X_1) + C\ log(X_2) + D \log(X_3) + \cdots \quad (4.8)$$

The parameters resulted from the CART analysis that correlate the dependent variables (D_{eff0} and a) to the stream and sediment characteristics presented in Figure 4.2 (independent variables), were used to build predictive formulae using the MLR technique. The data points of D_{eff0} and a resulted from fitting the diffusivity model to the measurements from the laboratory experiments. The standard error (SE) associated with each fitting value for D_{eff0} and a was used to estimate the weight of each data point ($w_i = 1/SE^2$) to be used in building the predictive model using the weighted sample mean estimator.

The package "gmulti" in R was used to introduce various models to correlate between the dependent and independent variable, as well as ranking them based on the Bayesian Information Criterion (BIC) (Schwarz & others, 1978). This criteria compromises between the number of the independent parameters included in the model and its parsimony to give the most parsimonious model with high goodness of fitting. Therefore, MLR was run on the top ranked model resulted from the gmulti function R to build predictive formulae for D_{eff0} and a. For each predictive formula, the coefficient of determination (R^2) and the Root Mean Square Error (RMSE) were introduced to show the quality of the predictive formula to the dataset. While for model validation, the cross-validation technique in R ($cv.glm$) was used to evaluate the cross-validation prediction error ($CV.Err$) by dividing

the dataset into subsets (10 folds) in which the model switches between them as training (9 folds) and validation data (1 fold).

4.3 Results

4.3.1 C Profile versus E Profile Performance

In the flat bed and alternat bars experiments, the E profile was found to better fit the measured data than the C profile, as shown, for example, for experiment B1 (flat bed) in Richardson and Parr (1988) study (Figure 4.3A) and experiment 12 (alternate bars) in Tonina and Buffington (2007) study (Figure 4.3B). Grant et al. (2020b) showed that the E profile is always better in the case of ripples and dunes.

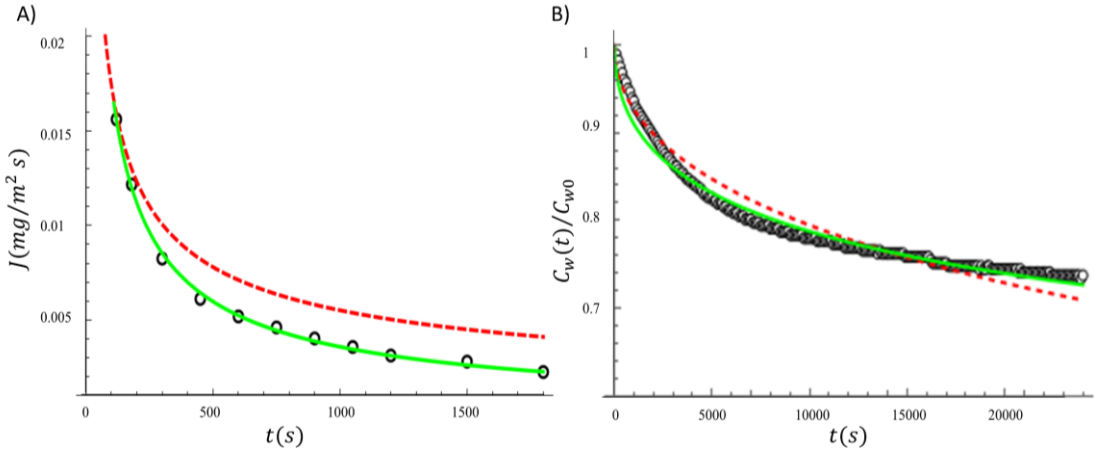

Figure 4.3: Fitting the C profile (dashed red line) and E profile (green line) to the flux out of the bed data (open black circles in (A)) of experiment B1 in Richardson and Parr (1988) study (A), and the dimensionless concentration in the water column (open black circles in (B)) of experiment 12 in Tonina and Buffington (2007) study (B).

For each experimental dataset, the diffusivity model (the set of equations in section 4.2) was applied, and the corrected Akaike Information Criterion (AICc (Akaike, 1974)) and coefficient of determination (R^2) values were obtained. According to AICc, the E profile is more parsimonious, even though it requires one extra parameter to be estimated compared to the constant profile, the improvement in the fit performance is high enough to compensate for the risk of over parameterization for most experiments (Figure 4.4A). As expected, the E profile also provides higher R^2 (Figure 4.4B) compared to the C profile. This superiority of the E profile over the C profile is in line with Grant et al. (2020a) results for flat bed experiments in stirring tanks (Chandler et al., 2016), and with Grant et al.

(2020b) results for ripples and dunes experiments (Elliott & Brooks, 1997a). In addition, many studies have shown that turbulent mixing intensity decays exponentially with the sediment depth (Chandler et al., 2016; Nagaoka & Ohgaki, 1990; Roche et al., 2019). Moreover, the E Profile can well represent the breakthrough curve of a tracer in either the laboratory or in the field (Bottacin-Busolin, 2019).

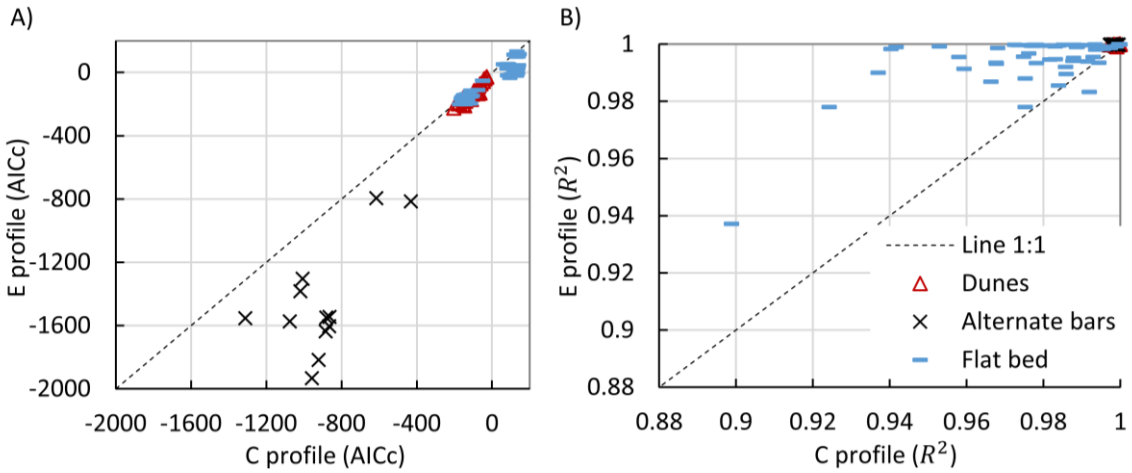

Figure 4.4: Comparison between the fitting criteria of C profile (horizontal axis) vs E profile (vertical axis) in terms of AICc (A) and R^2 (B) for the whole dataset considered in this study including flat bed, dunes, and alternate bars.

4.3.2 The Magnitude and Extent of the Mixing Processes.

The mixing processes magnitude differs between different morphologies. In the flat bed experiments, the mixing at the SWI (D_{eff0}) and the penetration into the sediment ($1/a$) extend over a wide range because many experiments were included in the analysis with different flow and sediment characteristics that influence the mixing process. The existence of an extra bed configuration (bedforms; ripples and dunes) creates, on average, more mixing at the SWI (high D_{eff0}) and deeper penetration in the sediment (low a), as an effect of the bedform pumping (Figure 4.5). In addition, more mixing (more D_{eff0}; Figure 4.5A, and less a; Figure 4.5B) is observed in alternate bars due to the 3-D complexity of its shape that induce lateral and longitudinal exchange across its shape (Monofy & Boano, 2021; Tonina & Buffington, 2007; Trauth et al., 2013) (see Chapter 2 for more details about the alternate bars). In addition, they usually form in gravel bed which has larger bores allowing for more diffusion compared to smaller granular particles (i.e., sand). The values of

log ($D_{eff,0}$) vary over 7 order of magnitude while log (a) values vary over only 3 orders of magnitude.

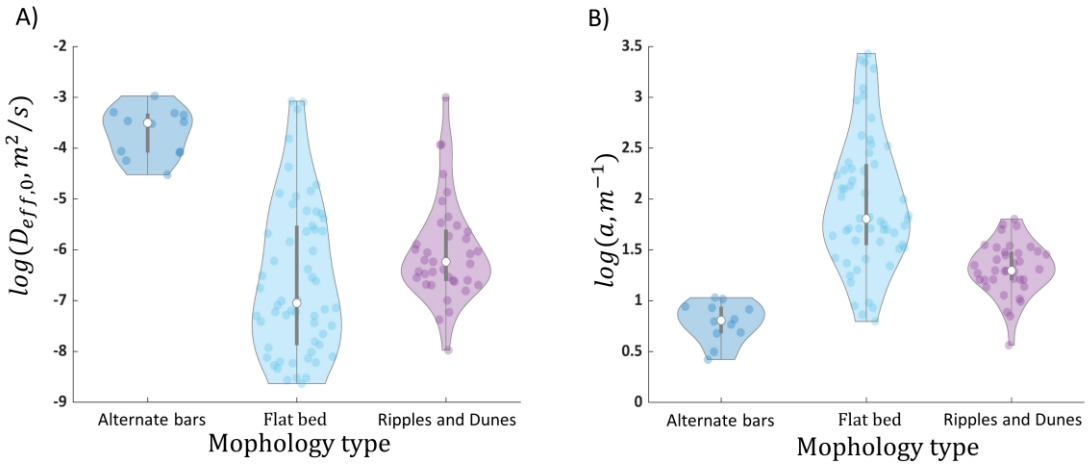

Figure 4.5: The effective diffusion coefficient (A) and the decay coefficient (B) values distribution for different morphologies (alternate bars, flat bed, and ripples and dunes).

4.3.3 CART Analysis Results

As explained in section 4.2, the regression tree was built on the dependent parameters (D_{eff0} and a) and a set of independent parameters shown in Figure 4.2, and the whole set of parameters are in APPENDIX A. The tree was pruned to the smallest tree with acceptable error (red arrows in Figure 4.6A and B). The highest discriminating parameters for log (D_{eff_o}) (Figure 4.6C) and log (a) (Figure 4.6D) are the sediment permeability (k_p) and water column depth (h_w). The morphology type does not appear to be one of the most important parameters for either of the dependent parameters. These regression trees performed well as predictive models with high R^2 and low $RMSE$ (0.78 for log ($D_{eff,0}$), and 0.2 for log (a)) (Figure 4.6).

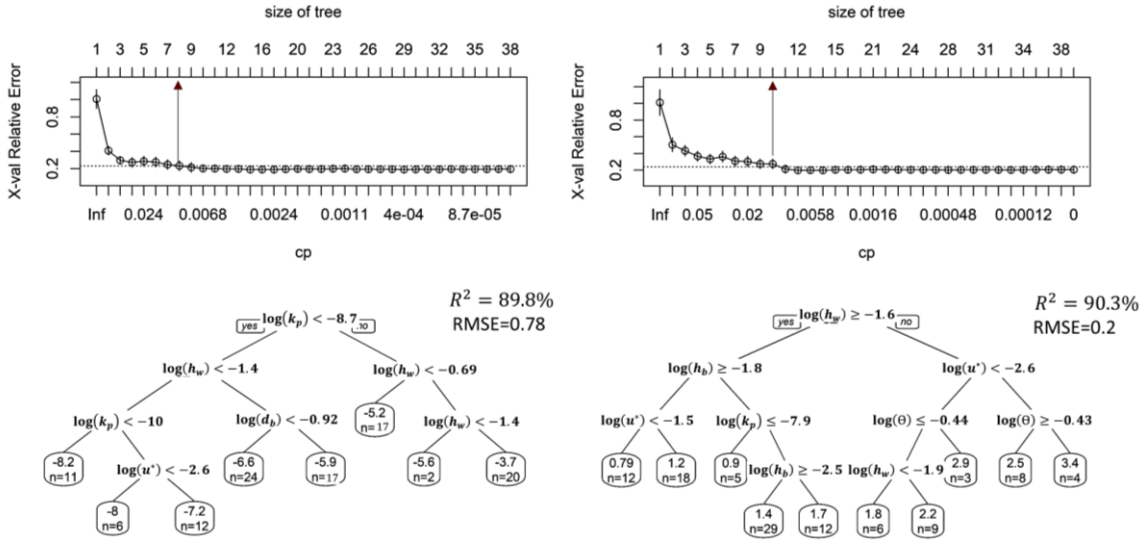

Figure 4.6: The stream, morphological, and sediment properties included in the CART analysis. The cross-validation relative error (X-val relative error) variation with the tree complexity parameter (CP) is shown in A, and B for log ($D_{eff,0}$) and log (a), respectively. The dashed black line in A and B represents the value of acceptable X-val relative error. The red arrows represent the pruning size of the tree. C and D are the pruned tree for log ($D_{eff,0}$) and log (a). n is the number of data points falling in the corresponding branch.

From the regression trees, D_{effo} can be predicted by knowing the values of k_p, h_w, d_b and u^*. While for a, the most important parameters are, in order, h_w, h_b, u^*, k_p and Θ. The results show that, sediment properties and bed configuration (e.g., k_p, u^*, h_b) has the greater influence on mixing processes compared to water column characteristics (e.g., h_w).

4.3.4 MLR Results

- **Dimensional MLR**

Based on the list of the best discriminating variables indicated by the regression trees, $D_{eff,0}$ and a can be expressed as a function of the following dimensional variables:

$$\log(D_{eff,0}) = A + B\ log(K_p) + C\ log(h_w) + D\log(d_b) + E\log(u^*) \quad (4.9)$$

$$Log(a) = X + \mathrm{Y}\log(h_w) + Z\log(h_b) + P\log(u^*) + Q\log(K_p) + M\ log(\Theta) \quad (4.10)$$

Based on Bayesian Information Criterion (BIC) (Schwarz, 1978), Table 4.2 shows the ranking of top three models. The top ranked models for $D_{eff,0}$ and a were chosen, and MLR was applied to determine the coefficient values. The resulting correlation equations are presented in Eqs. (4.11) and (4.12):

$$D_{eff,0} = 10^{6.23\pm0.45} {k_p}^{0.9\pm0.05} {u^*}^{2.6\pm0.11} h_w^{-0.71\pm0.09}, R^2 = 0.94, RMSE = 0.65\,, CV.Err = 0.43 \quad (4.11)$$

$$a = 10^{0.58\pm0.19} {u^*}^{-0.1\pm0.18} h_b^{-0.24\pm0.08}, R^2 = 0.43, RMSE = 0.55, CV.Err = 0.3 \quad (4.12)$$

Eq. (4.11) indicates the dependence of $D_{eff,0}$ on the sediment permeability, the shear stress on the SWI, and the water column height. The model for $D_{eff,0}$ explains 94% of the parameter variance (Figure 4.7A, and Eq. (4.11)) of which k_p accounts for 32%, u^* for 52%, and h_w for 10%. For all variables, the *P-value* is less than $2.8 * 10^{-11}$. The model for a has $R^2 = 43\%$ (Figure 4.7B, and Eq. (4.12)); h_b explains most of the variance (24%) with P-value $= 0.003$, while u^* explains a smaller portion (19%) with P-value $= 0.6$.

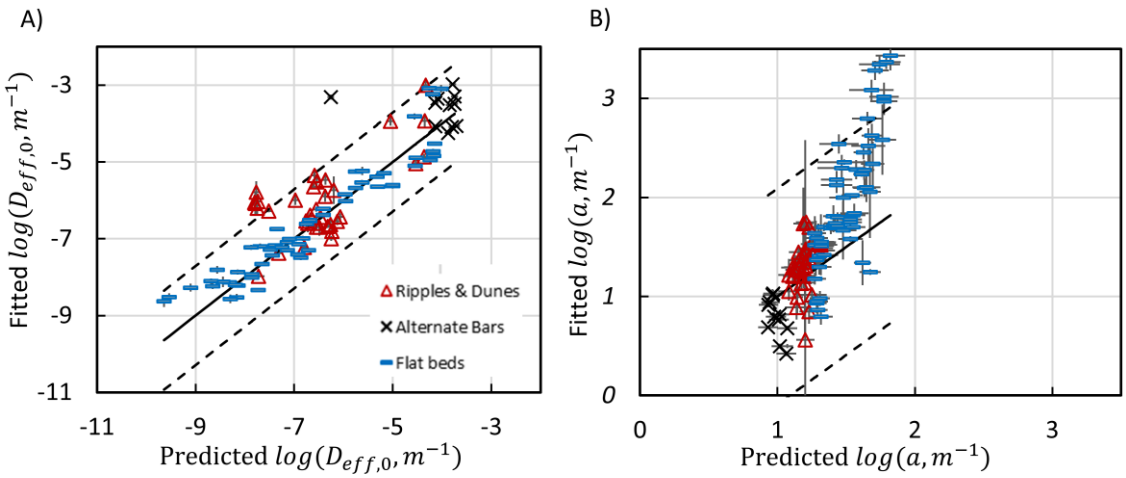

Figure 4.7: Comparison between the fitted values of (A) log ($D_{eff,0}$) and (B) log (a) using the E profile, and the predicted values by Eqs. (4.11) and (4.12), respectively. The solid black line is the 1:1 line while the dashed lines are the 95% prediction interval (PI).

Table 4.2: The list of dimensional predictive models for $D_{eff,0}$ and a, ranked based on BIC criteria.

Ranking	***Dimensional Models***	***BIC***
1	$Log(D_{eff,0}) \sim 1 + Log(k_p) + Log(u^*) + Log(h_w)$	215
2	$Log(D_{eff,0}) \sim 1 + Log(k_p) + Log(u^*)$	219
3	$Log(D_{eff,0}) \sim 1 + Log(u^*)$	289
1	$Log(a) \sim 1 + Log(u^*) + Log(h_b)$	74.03
2	$Log(a) \sim 1 + Log(h_w) + Log(u^*) + Log(h_b)$	77.89

3	$Log(\alpha) \sim 1 + Log(k_p) + Log(u^*) + Log(h_b)$	78.05

- **Dimensionless MLR**

Eqs. (4.11) and (4.12) are not dimensionally homogeneous; therefore, new correlations were developed by introducing dimensionless groups of variables. For $D_{eff,0}$, the variables identified in the top model were considered (k_p, u^*, h_b; Table 4.1). The coefficients of molecular diffusion D_m and kinematic viscosity ν were added to the set of variables for normalizing purposes. Therefore, six primary variables were considered, and according to the Buckingham π theorem, $D_{eff,0}$ can be represented as follows:

$$\frac{D_{eff,0}}{D_m} = f\left(Re_k = \frac{u^*\sqrt{k_p}}{\nu}, Re_b = \frac{u^* h_w}{\nu}, Sc = \frac{\nu}{D_m}\right) \quad (4.13)$$

where Re_k is the permeability Reynolds number that characterizes the transport process at the SWI interface (Grant et al., 2020a; Voermans et al., 2018). Re_b is the Reynolds number based on the shear velocity and water column depth that governs the 'log-law' equation of the wall region (Nakagawa, 2017), and Sc is the Schmidt number, which is related to interfacial mass transport (Bergman et al., 2011). Similarly, for a, the parameters in the top-ranked dimensional model (u^*, h_b; Table 4.2) and kinematic viscosity ν were considered to form the dimensionless groups. After testing different alternatives, the thickness of benthic biolayer (L_b) was used to normalize a. The approximate value (L_b= 2 cm suggested in the literature (Knapp et al., 2017) was employed:

$$a\,L_b = f\left(K_s = \frac{u^* h_b}{\nu}, K_b = \frac{u^* L_b}{\nu}\right) \quad (4.14)$$

where K_s is the dimensionless bed roughness (Nakagawa, 2017) that scales the bed roughness height to the viscous length (ν/u^*), and K_b compares the benthic biolayer thickness and viscous length.

Similar to the dimensional MLR analysis, Eqs. (4.13) and (4.14) were assumed to have a power-law structure. The best predictive formulae for $D_{eff,0}/D_m$ and $a\,L_b$ (Table 4.3) are:

$$\frac{D_{eff,0}}{D_m} = 10^{4.23\pm0.05} Re_k^{2\pm0.06}, R^2 = 92\%, RMSE = 0.59, CV.Err = 0.36 \quad (4.15)$$

$$a\,L_b = 10^{-0.006\pm0.06} K_s^{-0.2\pm0.02}, R^2 = 43\%, RMSE = 0.55, CV.Err = 0.31 \quad (4.16)$$

Eq. (4.15) predicts very well ($R^2 = 92\%$; Figure 4.8A) the value of $D_{eff,0}/D_m$, which is explained only by Re_k with $P\text{-}value < 2 \times 10^{-16}$. On the other hand, Eq. (4.16) explains only a small portion of the variance of $a\,L_b$ values ($R^2 = 43\%$; Figure 4.8B). Considering that the variations in a is not so large for each morphology type (Figure 4.8B), Eq. (4.16) still can explain some of these small variations with $RMSE = 0.55$. The associated $CV.Err$ in both cases, created by dividing the data into 20 folds, is less than 0.31. By looking at Figure 4.7B and Figure 4.8B, the predictive formulae for the decay coefficient in both dimensional (a) or dimensionless form ($a\,L_b$) do not explain the wide variability in the data. This is more pronounced for flat beds, for which the formulae underpredict a values by at least one order of magnitude.

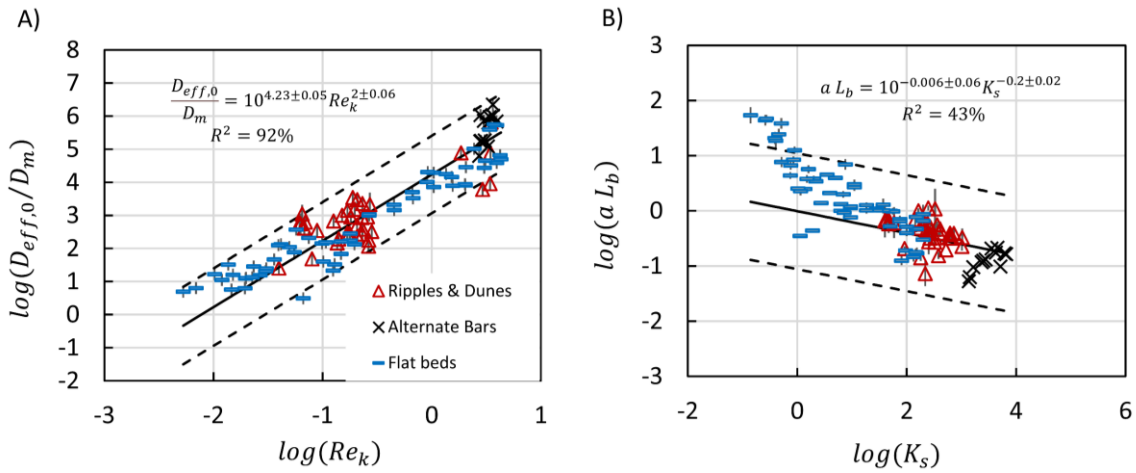

Figure 4.8: Comparison between the fitted values of (A) log ($D_{eff,0}/D_m$) and (B) log ($a\,L_b$) using the E profile, and the predicted values by Eqs. (4.15) and (4.16), respectively. The solid black line is the 1:1 line while the dashed lines are the 95% prediction interval (PI). The vertical black lines associated with each point represents the measurement errors.

Table 4.3: The list of dimensionless predictive models for $D_{eff,0}$ and a, ranked based on BIC criteria.

Ranking	***Dimensionless Models***	***BIC***
1	$Log(D_{eff,0}/D_m) \sim 1 + Log(Re_k)$	191
2	$Log(D_{eff,0}/D_m) \sim 1 + Log(Re_k) + Log(Re_b)$	194
3	$Log(D_{eff,0}/D_m) \sim 1 + Log(Re_b)$	309
1	$Log(a\,L_b) \sim 1 + Log(K_s)$	71.6
2	$Log(a\,L_b) \sim 1 + Log(K_s) + Log(K_b)$	71.7
3	$Log(a\,L_b) \sim 1 + Log(K_b)$	99.8

Given the unsatisfactory performance of the predictive Eq. (4.16) shown in Figure 4.8B, values of $a\,L_b$ were separately analyzed according to the type of streambed morphology. Grant et al. (2020a) provided an empirical formula to predict a values that included a dependence on Re_k those scales differently for $Re_k < 1$ and $Re_k > 1$ due to changes in the prevailing exchange mechanisms.

It should be noticed that this formula was built only from the stirring tank experiments with flat beds of Chandler et al. (2016). Here, in addition to these experiments, other flume experiments with flat beds were considered to account for a wider range of a variations over Re_k (Figure 4.9), and a more accurate predictive formula for $a\,L_b$ was obtained (Eq. (4.17)):

$$a\,L_b = \begin{cases} 10^{-1.36\pm0.39} Re_k^{-1.32\pm0.23}, & Re_k < 0.1,\ R^2 = 59\%, RMSE = 0.37 \\ 0.16 \pm 0.06, & 0.1 < Re_k < 1,\ RMSE = 0.23 \\ 10^{-0.001\pm0.07} Re_k^{-0.79\pm0.21}, & Re_k > 1,\ R^2 = 78\%, RMSE = 0.21 \end{cases} \quad (4.17)$$

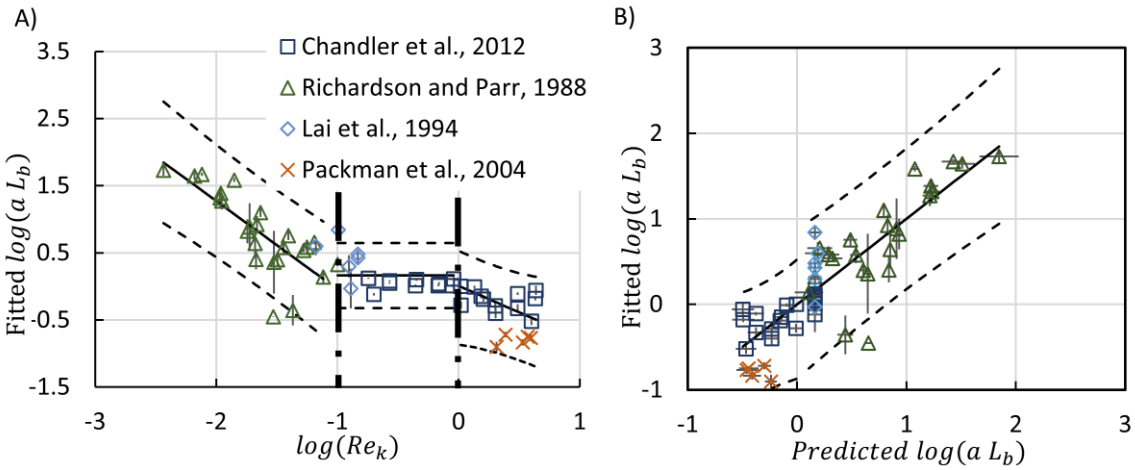

Figure 4.9: The variations of the inverse-decay depth over different ranges of the permeability Reynolds number in flat bed experiments (A) with vertical dash dotted lines represent the log (Re_k) values where log (aL_b) behaviour changes, the dotted black line represents the 95% prediction interval, and the solid line demonstrates the predicted values by Eq. (4.17). A comparison between the predicted values by Eq. (4.13), and the fitted values obtained by applying the diffusivity model on the flat bed experiments (B) with 1: 1 line (black line), and 95% prediction interval (dotted lines). The vertical black lines associated with each point represents the measurement errors. The long dash dots in (A) represents the Re_k values of 0.1 and 1.

The regression tree algorithm was then run separately on the ripples and dunes dataset. The wavenumber emerged as the discriminative variable that explains most of the variance. Therefore, a dimensionless correlation between a and W_n was built (Eq. (4.18)). This predictive formula explains reasonably well the observed variations in a ($R^2 = 81\%$; Figure 4.10). This result is in line with one found by Grant et al. (2020b) (Eq.16b in their paper) over a similar range of λ (8.8 ~ 32 cm), with a varying linearly with $1/\lambda$.

$$a\,L_b = 10^{-0.18\pm0.14}(W_n L_b)^{1.02\pm0.09}, R^2 = 81\%, RMSE = 0.18, CV.Err = 0.035 \qquad (4.18)$$

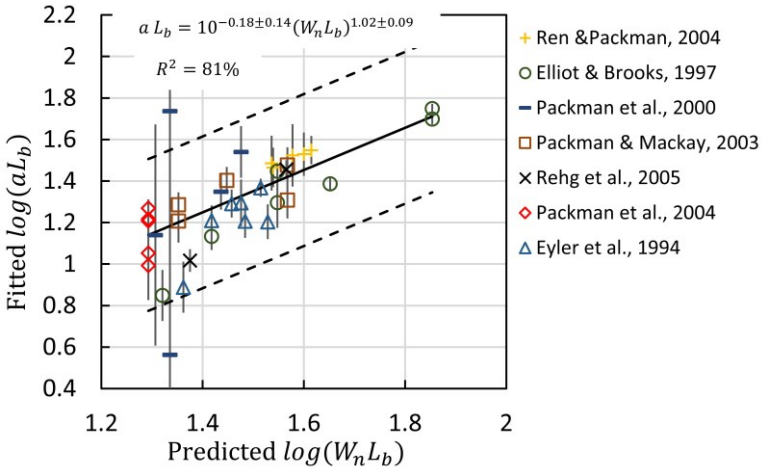

Figure 4.10: The predicted values of a by Eq. (4.18) versus the fitted values by applying the diffusivity model on ripples and dunes experiments. The solid line is the 1: 1 line, while the dotted line is the 95% predition interval.

Finally, the same approach was applied to the experiments with alternate bars. Unfortunately, as very few experiments have been performed on this morphology type, no reliable predictive formula could be obtained for this morphology type.

4.3.5 Bed Configuration effect on the Mass Transport Process

The presence of bedforms on the SWI changes the physics associated with the boundary layer at the SWI and the bed roughness, and these changes can enhance the exchange process (Elliott & Brooks, 1997b; Grant et al., 2012, 2018; Packman et al., 2004). To quantify the additional exchange induced by the bedforms, the flat bed data was used as training data to a predictive model that further used to predict the exchange parameters in ripples and dunes, and alternate bars dataset (test data). The predicted values from the model are compared with the fitted values using the diffusivity model, and the difference indicates the adds-on of each bedform type to the exchange process.

- **Effective Diffusion Coefficient in Flat bed:**

Following the same approach of section 4.2 , a regression tree analysis was first carried out to identify the dimensional parameters that most influence the value of $D_{eff,0}$. Then, MLR was performed on the dimensional and dimensionless parameters, which indicated that $D_{eff,0}$ is strongly correlated to Re_k (Figure 4.11). These results are expressed by the following dimensionless formula:

$$\frac{D_{eff,0}}{D_m} = 10^{3.78\pm0.09} Re_k^{1.58\pm0.09}, R^2 = 85\%, RMSE = 0.47, CV.Err = 0.23 \qquad (4.19)$$

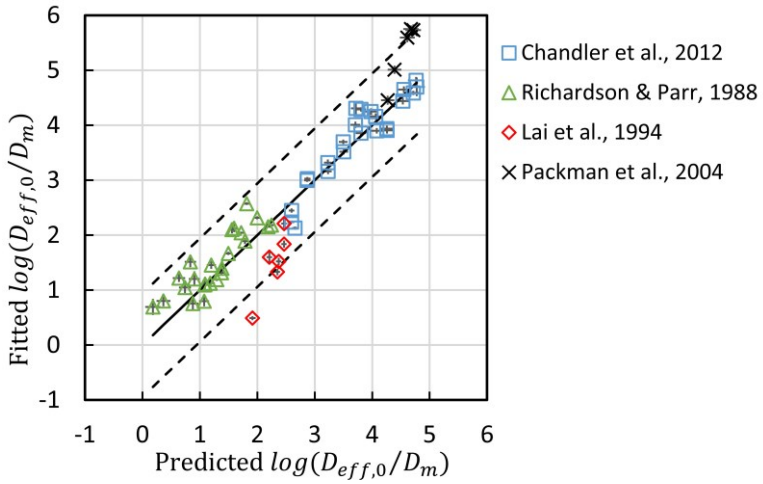

Figure 4.11: The predicted values of $D_{eff,0}/D_m$ by Eq. (4.19) versus the fitted values by running the diffusivity model on the flat bed experiments. The solid line is the 1: 1 line, while the dashed line is the 95% predition interval.

- **Exchange added by Bedforms and Alternate Bars.**

Eq. (4.19) was applied to estimate the value of the diffusion coefficient that is expected in absence of bedforms, while Eq. (4.17) was used to determine the penetration depth. As shown in Figure 4.12, ripples and dunes, as well as alternate bars, strongly increase the exchange process at the SWI as discussed before. Based on median values of $D_{eff,0}$ and a, the presence of dunes increases the surficial exchange and the penetration depth by a factor of 1.9 and 2.9, respectively. The larger 3-D morphologic configuration of the alternate bars

induces much more surficial exchange (16.7 times) and more penetration of the mixing depth (3.2 times) compared to the flat bed.

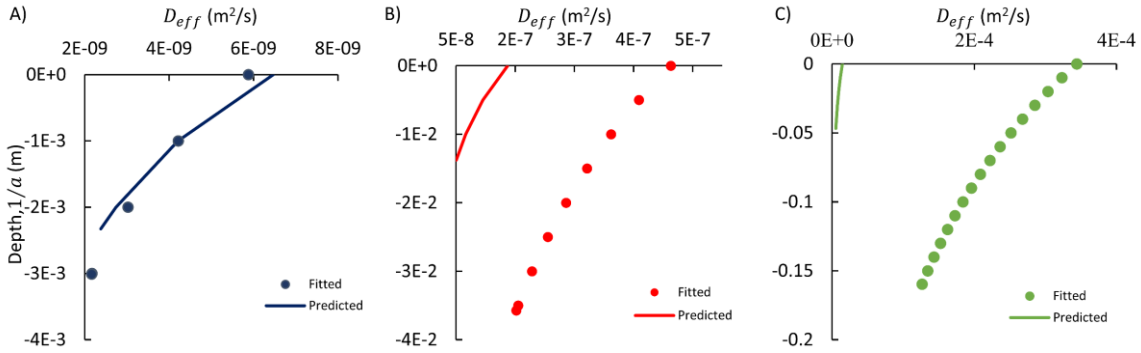

Figure 4.12: The predicted diffusivity profile by Eq. (4.19) for $D_{eff,0}$ and Eq. (4.17) for a (solid lines) vs the fitted ones (filled circles) in (A) (Experiment #B8 in Richardson and Parr (1988), (B) Ripples and dunes (Experiment #E15 Flat bed in Elliott and Brooks (1997a)), and (C) Alternate bars (Experiment #E7 in Tonina and Buffington (2007)).

4.4 Discussions

There are many physical processes that control solute transport across the SWI, e.g., molecular diffusion, turbulent diffusion, dispersion, bedform pumping, and many others (Grant et al., 2020a; Hester et al., 2021; Kleinhans & Vollmer, 2008; O'Connor & Harvey, 2008; Roche et al., 2019; Santos et al., 2012; Voermans et al., 2018). The sediment bed characteristics affect the mixing process significantly. For example, in flat bed experiments, the magnitude of mixing at the SWI is significantly influenced by Re_k that combines the pore length scale ($\sqrt{k_p}$) and the viscous length (ν/u^*). This quantity can delineate the behavior of the sediment layer in relation to the water column, in agreement with Voermans et al. (2018). At very low Re_k (< 0.1), the sediment layer behaves as a blocking wall (quasi-impermeable layer), and the effective diffusion (D_{eff0}) values are close to the molecular diffusion values (Figure 4.8A). Increasing the Re_k implies higher turbulent intensity that weakens the wall-blocking effect, the solutes are rapidly mixed (Roche et al., 2018) and resulting in deeper penetration into the sediment (Voermans et al., 2017; Grant et al., 2020a). At high $Re_k > 1$, more mixing is induced (Figure 4.8) to deeper penetration (Figure 4.9A). Between the low Re_k (<0.1) and its high values (>1), there is a transition zone which, presumably, dominated by dispersion. Within this zone, the penetration depth is almost constant with increasing Re_k. As the data points within this range came from only one experimental campaign (Chandler et al., 2016), it may be an

effect of the experimental setup. Therefore, more experiments within this range are needed to demonstrate wither this mixing behavior stems from experimental setup or it reflects the true mixing between the sediment domain and the overlying water column.

The dependence of D_{eff0} on the Re_k in flat bed see in Eq. (4.19), and Figure 4.11 is in agreement with many of previous studies (e.g., Grant et al., 2012, 2018, 2020a; Voermans et al., 2018). This correlation between D_{eff0} and Re_k (Eq. (4.15) and Figure 4.8) is found also for bedforms (ripples and dunes) and alternate bars. This is consistent with other studies that proved the sediment permeability (k_p) role in stream ecosystem (Battin et al., 2016). In addition, the bed shear stress (correlated to u^*) is an important quantity for sediment-water interaction, as it is correlated to stream water levels, and sediment transport and resuspension (Horritt & Bates, 2002).

The mixing depth in ripples and dunes is significantly correlated to the bedform wavelength (Eq. (4.18)). This is coherent with what was found by Elliott & Brooks (1997b) and Grant et al. (2020b). In comparison with flat bed, this implies the dominance of bed configuration, and its induced advective (bedform) pumping effect in delineating the mixing depth (Hester et al., 2021). This mixing depth is on the order of centimeters, as shown in experimental (e.g., Hester & Gooseff, 2010; Santizo et al., 2020) and modeling (Grant et al., 2020a, 2020b) studies.

For alternate bars, given the small number of available experiments, it was not possible to provide a robust predictive formula for the exchange parameters separately from the other morphology types. Further experimental studies on this morphology type are hence required.

Generally, the presence of bedforms on the streambed causes additional exchange compared to the flat bed configuration. When a depth-invariant effective diffusion coefficient is employed, dunes have been reported to increase it by a factor of 3~6 (Packman et al., 2004) and ~ 3.5 (Grant et al., 2018) compared to flat beds. Our results are in line with these findings; ripples and dunes increase $D_{eff,0}$ and penetration depth by a factor of 1.9 and 2.9, respectively. This increased exchange magnitude is essentially caused by the advective pumping due to the bedform shape (Azizian et al., 2017; Elliott & Brooks, 1997a, 1997b; Grant et al., 2014; Hester et al., 2021). For alternate bars, the lateral and longitudinal pattern of pressure variations (e.g., Monofy & Boano, 2021) induces a significant increase in effective diffusion (16.7 times) and deeper exchange depth into the

sediment (3.2 times) compared to the flat beds. These results agree with the experimental results by Santizo et al. (2020) and Hester and Gooseff (2010) who proved that larger bedforms induce more mixing depth.

Despite the relaxation of some constraints of previous modeling approaches (i.e., accounting for the negative feedback, and the exponential diffusion decay with depth), some simplifications have been made to develop the present model, e.g., assuming that porosity and hydraulic conductivity to be spatially constant over sediment depth. Furthermore, the choice of including the stirring tank experiments by Chandler et al. (2016) forced us to dismiss flow velocity from the analysis, focusing only on u^* to describe the hydrodynamics of surface flow.

4.5 Conclusion Marks and Future research

The novelty of our new mathematical framework lies in its relaxation for some constraints that were considered in previous studies, as well as its parsimony. The model accounts for the two-way feedback between the solute concentration in the interstitial fluid and its concentration in the water column. In addition, different spatial variation of solute concentration within the sediment can be assumed. Sediment characteristics and flow velocity within the shear layer (permeability and shear velocity) are the most influencing parameters in determining the magnitude of the mixing process at the SWI. However, the bed configuration significantly affects solute penetration into the sediment. In general, alternate bars induce more mixing than bedforms (ripples and dunes) and flat bed. In addition, bedforms induces more mixing magnitude and penetration than in flat bed. The surficial effective diffusion varies over 6 orders of magnitudes between different bed configurations, while the mixing (penetration depth) varies over a smaller range (~3 orders of magnitudes). A unique predictive formula can be introduced to estimate the effective diffusion at the SWI over all types of morphology depending on the permeability Reynolds number. While for the mixing depth, it is better predicted separately for different types of morphologies. It depends on the permeability Reynolds number in flat bed and on bedform wavelength in ripples and dunes.

This diffusivity model was applied to flume experiments with stationary bedforms and steady flow that resulted in the predictive formulae introduced in this chapter. The application of this model to stream environments (networks), experiments with bedform turnover, unsteady flow, and sediment beds with reactive solutes (APPENDIX B) is

important to test its validity, and the applicability of its derived predictive formulae for different morphologies on versatile conditions.

Chapter 5
Geostatistical Method Application to Estimate the Response Time to Flow Waves, Salt Concentration and Load in the Occoquan Watershed in Northern Virginia

5.1 Introduction

The freshwater salinization induced by climatic conditions is common in arid and semi-arid areas (Kaushal et al., 2022; Schulz & Cañedo-Argüelles, 2019; Williams, 2001). However, in recent years, this issue is rising in many places with cold weather (i.e., USA and Canada) (Dugan et al., 2017; Kaushal, Likens, et al., 2018). This trend is mainly caused by human activities, including the use of household products, road deicers and many other sources (see section 1.2 for more details). These activities drive the Freshwater Salinity Syndrome (FSS) that can lead to harmful conditions for the environment and human health (Bhide et al., 2021).

This issue of freshwater salinization is evident of the Occoquan watershed, where the recorded data of more than 25 years shows elevated salt concentration and loads, and more frequent spikes, in recent years. The problem of salt load and concentration rise has currently reached the attention of the local authorities who decided to further investigate the problem. The Fairfax water treatment plant is placed just downstream the Occoquan reservoir and provides freshwater for most of the population in northern Virginia (see the study of Bhide et al. (2021) for a thorough discussion of the salt load problem in the Occoquan reservoir). In this chapter, we predict the response time of the Occoquan reservoir due to variations in input water flow, salt concentration and salt load at the

upstream parts of the Occoquan watershed (Occoquan and Bull Run Rivers, see Figure 5.1A). Understanding the salt dynamics and residence times in the reservoir can help the authorities in determining specific operational procedures for the Occoquan reservoir and dam.

5.2 Methodology

5.2.1 Data Collection

The considered study area here is the Occoquan reservoir which is located around 30 km southwest of Washington DC in northern Virginia (USA). It is the main source of fresh water for around 2 million people in its surrounding region (Bhide et al., 2021). This reservoir collects water from two main tributaries: the Occoquan, and the Bull Run Rivers where there is an effluent of a wastewater treatment plant (UOSA) on the later. Just downstream of the Occoquan dam there is the intake for Fairfax water station (see Figure 5.1A). In the present analysis, we employed values of salt concentrations (Figure 5.1B) and load, and the measured flow values that were available from previous monitoring campaigns in the Occoquan reservoir. Samples from the Occoquan River and Bull Run River were collected at ST10, ST45, UOSA and the Fairfax water intake (see Figure 5.1A for the samples locations and B for the data demonstration). ST10 and ST45 measuring stations were considered as input for the Occoquan reservoir. To measure the salt concentration at the reservoir, samples were taken at ST01 which is a station placed downstream of the Occoquan dam at the Fairfax water treatment plant intake. The time series used by Bhide et al. (2021) for the three measuring stations were utilized in this study.

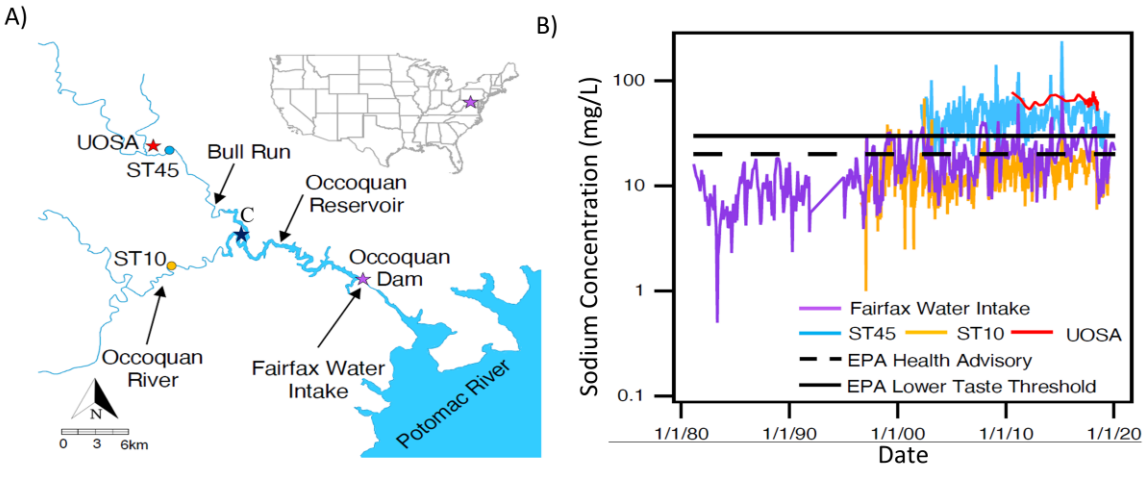

Figure 5.1: (A) the map of the Occoquan reservoir and its tributaries, in addition to the data measurement locations, the purple star is the Fairfax Water intake (ST01), while (B) represents Forty years of sodium concentration measurements at the Fairfax Water intake and the upstream stations (ST10, ST45), and the final reclaimed water discharged by UOSA (Bhide et al., 2021).

5.2.3 The Geostatistical Method

Here, we used the geostatistical method (Boano et al., 2005; Kitanidis, 1995, 1996; Snodgrass & Kitanidis, 1997) to determine the response time distribution of sodium in the Occoquan reservoir, which is denoted as $f(t)$ (the method is described in detail in APPENDIX C). In this approach, a probabilistic description of the involved quantities is adopted. For the problem dealt with here, $f(t)$ is interpreted as a stochastic process and it represents many associated functions (possible distributions of response times). The most probable one is chosen based on the consistence between the predictions and the observations. Here, we adopt the solution of this approach with single measurement point (Boano et al., 2005) with the nonnegativity constraint for $f(t)$.

The data from ST10 and ST45 were combined to form a single source point. According to the geometry of the area (Bull Run and the Occoquan Rivers distances from the reservoir), the flow and load arrive at the confluence C (Figure 5.1A) with difference of 2 hours between them, assuming similar velocity in both reaches. This combination between ST10 and ST45 was considered to build the transfer matrix H (APPENDIX C). ST01 was considered as the output measuring point; therefore, the data from this station was used to build the output vector z. The method was applied to calculate response times of flow $Q(t)$, salt concentration $C(t)$, and salt load $L(t) = Q(t) \cdot C(t)$, as these signals can provide different information on the behavior of the reservoir. Hourly data were used to estimate the transfer matrix for the flow analysis, while daily data were used for the analyses of concentration and load. This difference in temporal resolution is because the concentration and load pulses at the source points (ST10 and ST40) impact the output point (ST01) after a time of an order of magnitude of days. Instead, for flow, the impact is observed from the data after some hours. The events considered for our analysis are listed in Table 5.1 for flow and salt concentration and load. In order to explore the system response time for different events, as in Table 5.1, three different events were considered for the flow data (Figure 5.2), other two events were adopted for the concentration data (Figure 5.3), and five events were chosen for the load data (Figure 5.4). The geostatistical method predicts the output values based on the input values of the input matrix (H), the

error variance of the source measurement, the nonnegativity parameter, and the initial values of the structure parameters (see Boano et al. (2005) and APPENDIX C for more explanation).

Table 5.1: A list of the considered events to estimate the transfer function for flow, load, and concentration.

Flow
Event #1: From 2010/10/22 23:00:00 to 2010/10/30 11:00:00
Event #2: From 2013/01/10 19:00:00 to 2013/01/20 19:00:00
Event #3: From 2016/09/15 02:00:00 to 2016/10/10 02:00:00

Concentration
Event #1: From 2014/08/27 to 2015/06/23
Event #2: From 2015/01/13 to 2015/05/05

Load
Event #1: From 2010/07/02 11:00:00 to 2010/07/23 07:00:00
Event #2: From 2010/11/19 06:00:00 to 2010/12/11 23:00:00
Event #3: From 2012/11/02 15:00:00 to 2012/11/19 07:00:00
Event #4: From 2015/10/17 18:00:00 to 2015/11/01 08:00:00
Event #5: From 2020/09/16 14:00:00 to 2020/10/07 10:00:00

5.3 Results and Discussion

5.3.1 Response Time for Flow

After applying the geostatistical method to the flow events, we can obtain the system response corresponding to each event. We found that the system response time at the output to a flow wave at the input is of the order of a few hours. For event #1, the flow at the reservoir outlet predicted with the response time distribution $f(t)$ is comparable with the observed one (Figure 5.5), which demonstrates the correctness of $f(t)$. The peak response time is 4 hours (hrs) for event #1 (Figure 5.6A), 5 hrs for event #2 (first peak in Figure 5.6B), and 7 hrs for event #3 (Figure 5.6C). For the three events, the distributions of response times range between 10 and 20 hours, indicating that the system outflow reacts to variation in inflow discharge in less than one day.

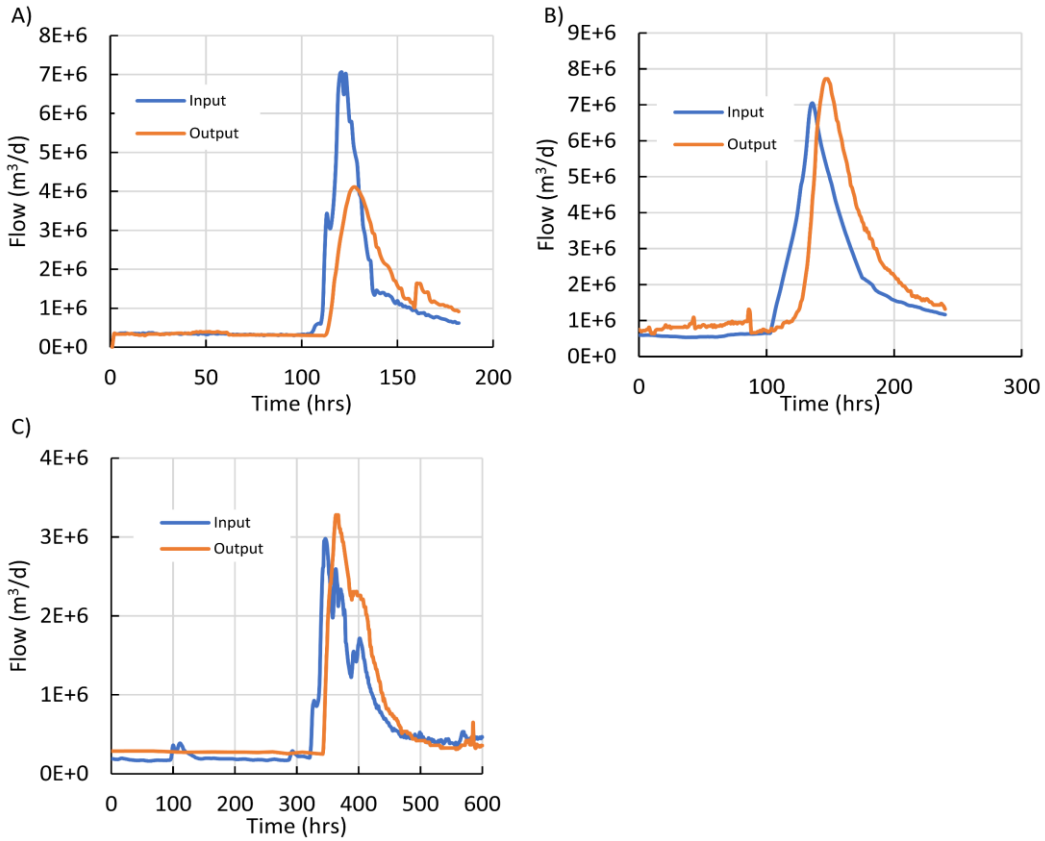

Figure 5.2: The considered events for the water flow data; A) event #1, B) event #2, and C) event #3.

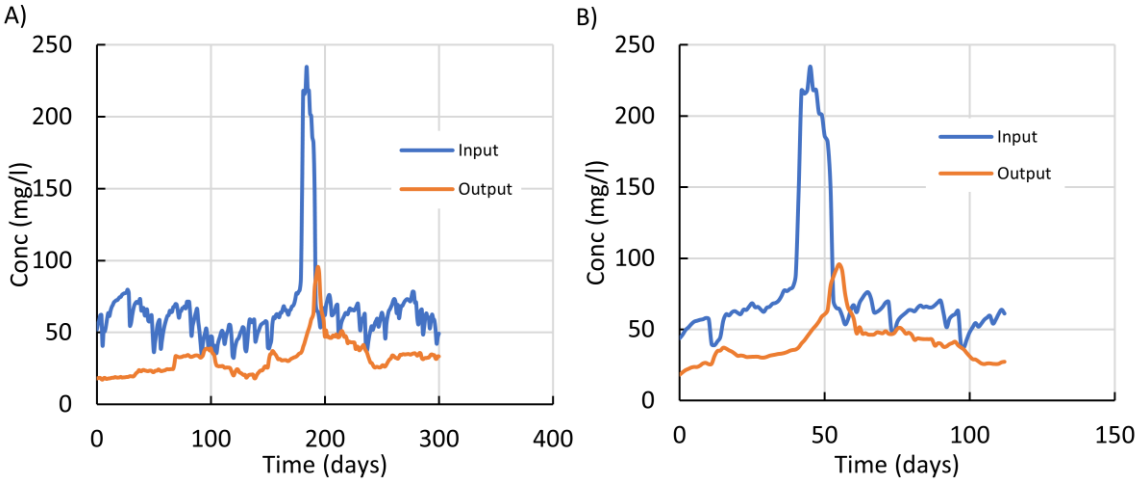

Figure 5.3: The considered events for the salt concentration data; A) event#1, and B) event#2.

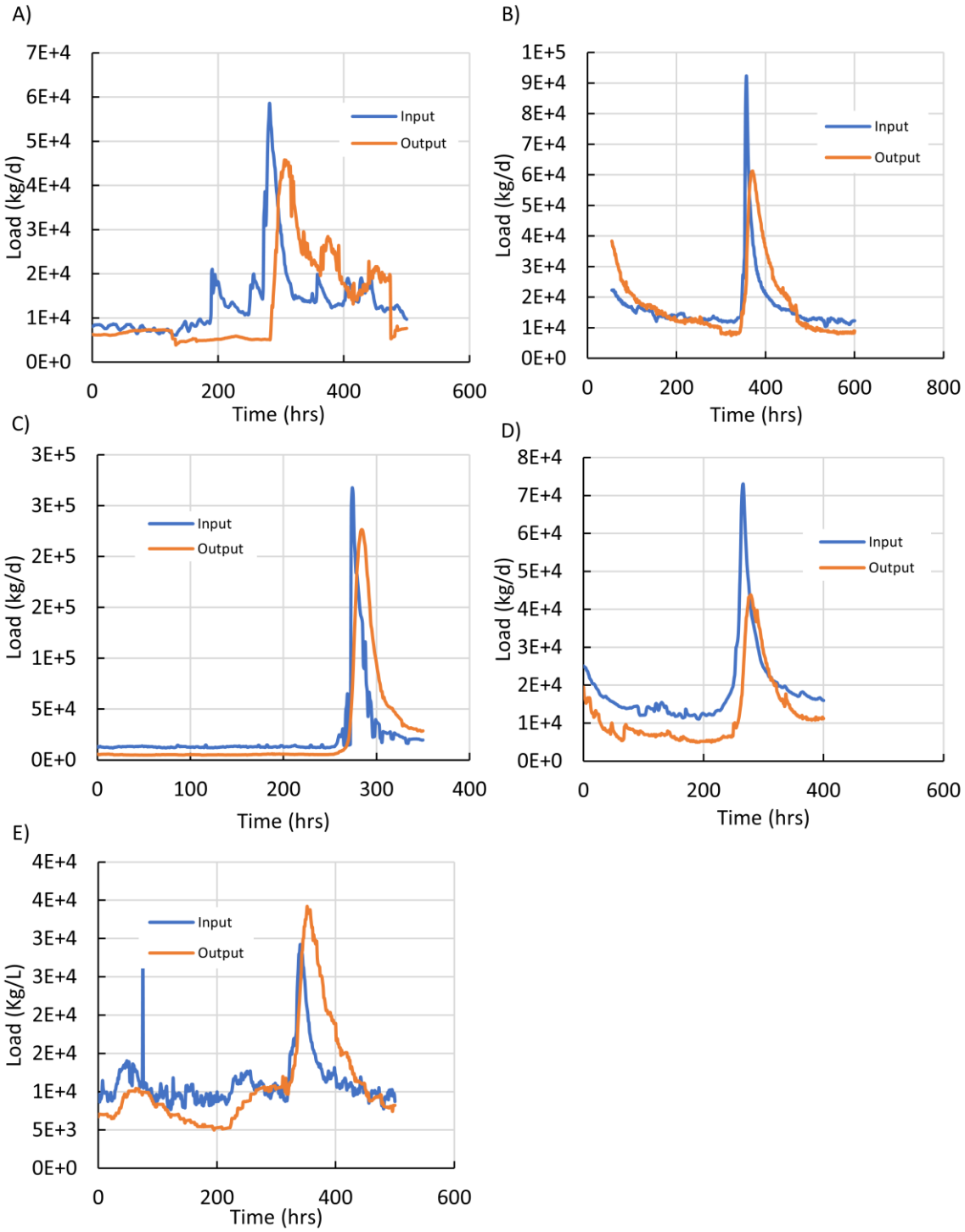
A)
Load (kg/d)
7E+4
6E+4
5E+4
4E+4
3E+4
2E+4
1E+4
0E+0
0
200
400
600
Time (hrs)
Input
Output
B)
Load (kg/d)
1E+5
9E+4
8E+4
7E+4
6E+4
5E+4
4E+4
3E+4
2E+4
1E+4
0E+0
0
200
400
600
800
Time (hrs)
Input
Output
C)
Load (kg/d)
3E+5
3E+5
2E+5
2E+5
1E+5
5E+4
0E+0
0
100
200
300
400
Time (hrs)
Input
Output
D)
Load (kg/d)
8E+4
7E+4
6E+4
5E+4
4E+4
3E+4
2E+4
1E+4
0E+0
0
200
400
600
Time (hrs)
Input
Output
E)
Load (Kg/L)
4E+4
4E+4
3E+4
3E+4
2E+4
2E+4
1E+4
5E+3
0E+0
0
200
400
600
Time (hrs)
Input
Output

Figure 5.4:The considered events for the salt load data; A) event #1, B) event #2, C) event #3, D) event #4, and E) event #5.

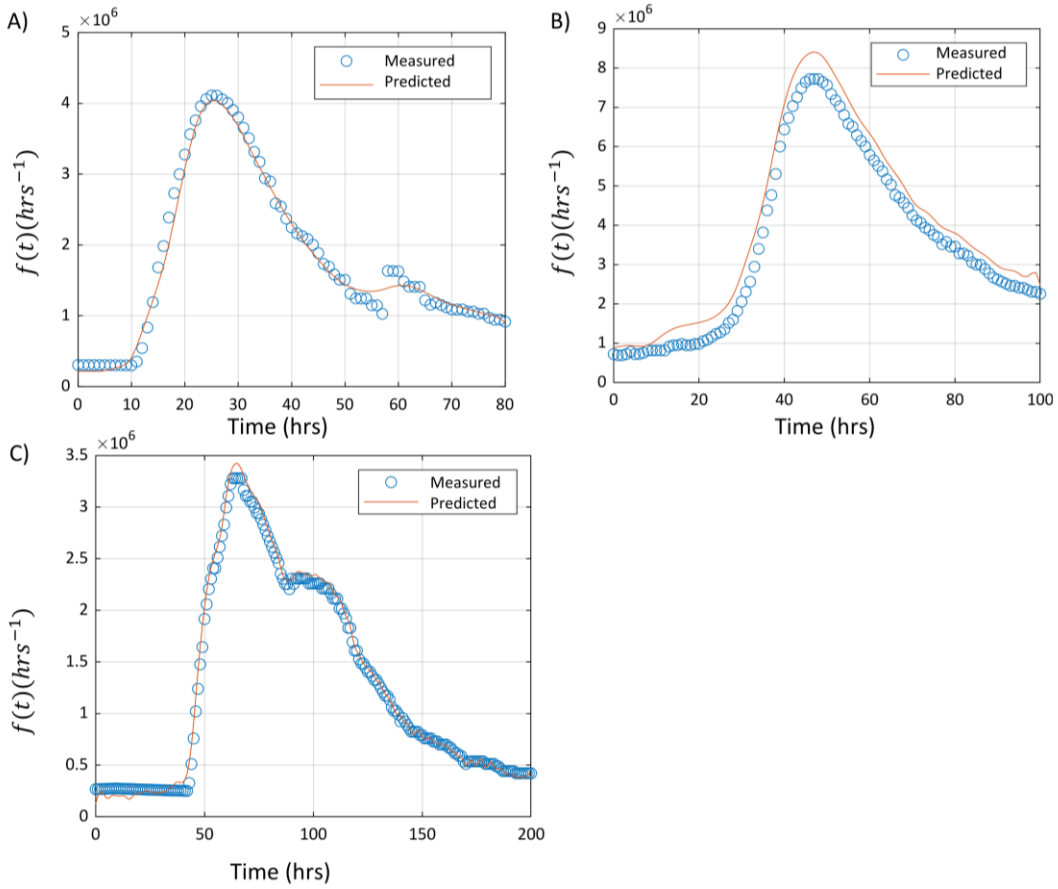

Figure 5.5: A comparison between the predicted outflow by the geostatistical method and the observed outflow at station ST01 for events #1 (A), #2 (B), and #3 (C).

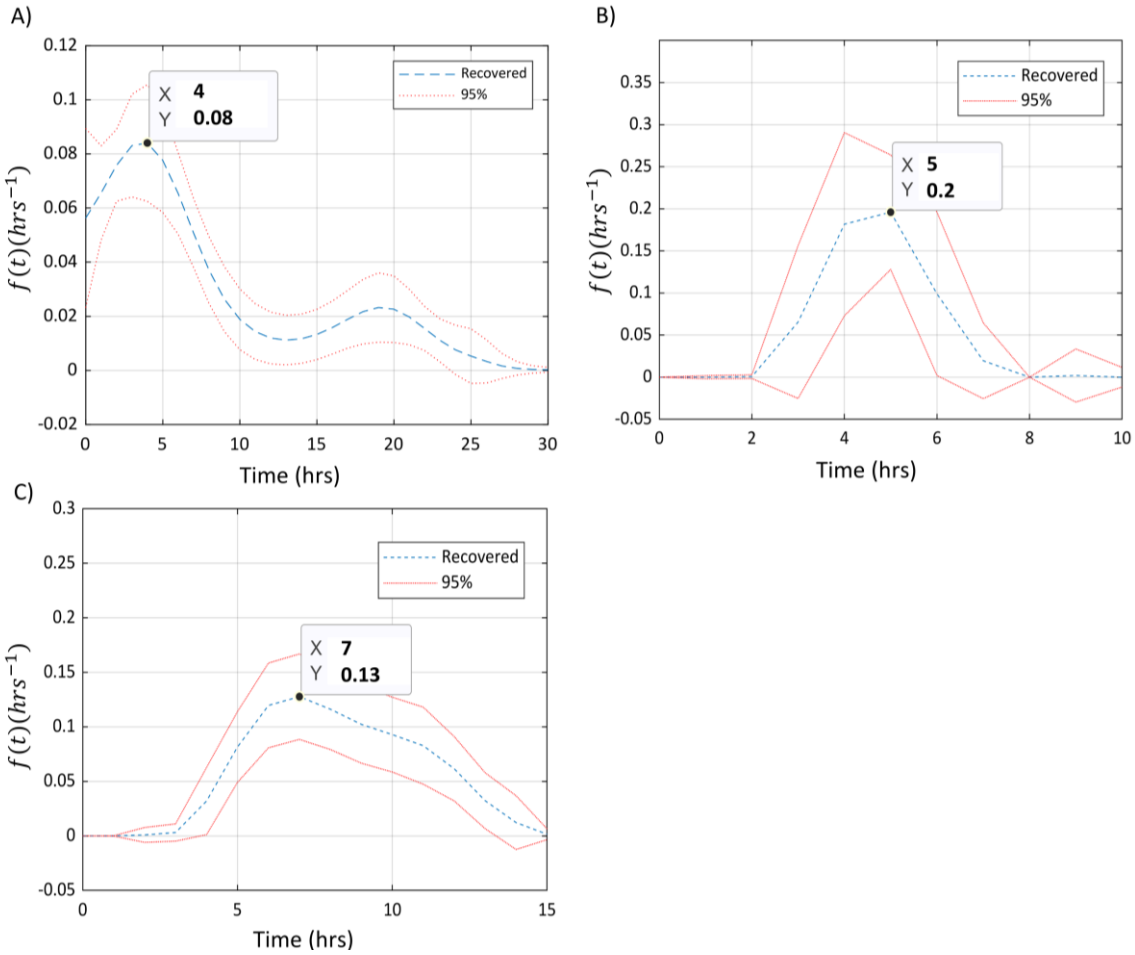

Figure 5.6: The results for the system response time for the outflow pulses for events #1 (A), #2 (B), and #3 (C).

5.3.2 Response Time for salt Concentration and load

For the two concentration events considered here in the Occoquan reservoir (Table 5.1), the predicted concentration pulses at the output coincide with the observed ones for both events (Figure 5.7) although the modeled peak value is slightly smoothed compared to the observed one, suggesting that the faster variations are not perfectly reproduced. The peak response time for the system to a variation in the concentration of salt is 8 and 9 days for event #1 (Figure 5.8A) and #2 (Figure 5.8B), respectively. These response times are much longer than those estimated for flow events, reflecting the fact that salt behaves as a tracer that requires days to months to travel through the reservoir and its response times represent actual travel times in the system. On the other hand, response to flow events is much faster

as system outflow is controlled by the water level in the reservoir, which adjusts relatively quickly to variations in inflow spikes. Figure 5.7 also shows that the whole range of response times of $f(t)$ is around 40-50 days, hence indicating that the system is influenced by changes in inflow concentrations for more than one month because of slow salt mixing in the reservoir.

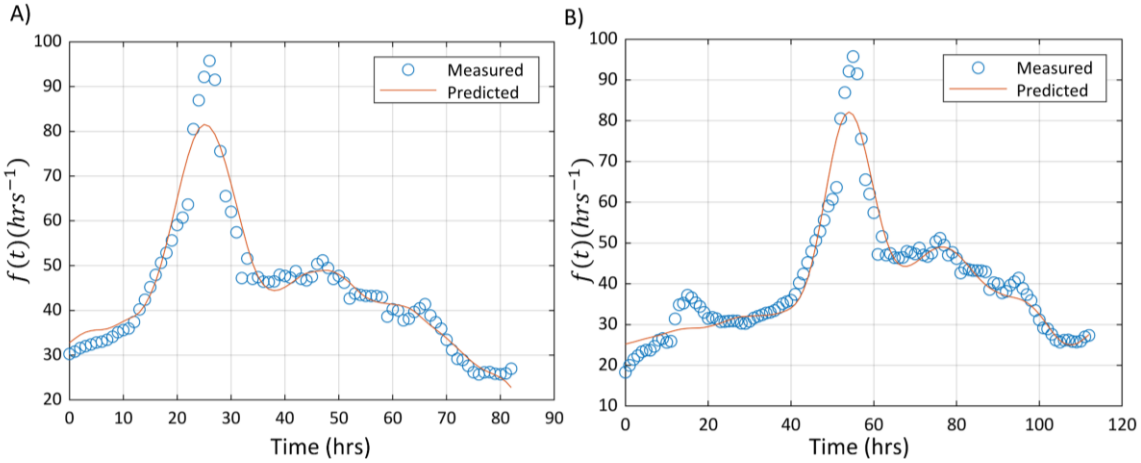

Figure 5.7: A comparison between the predicted concentration by the geostatistical method and the observed concentration at the output station for event #1 (A) and event #2 (B).

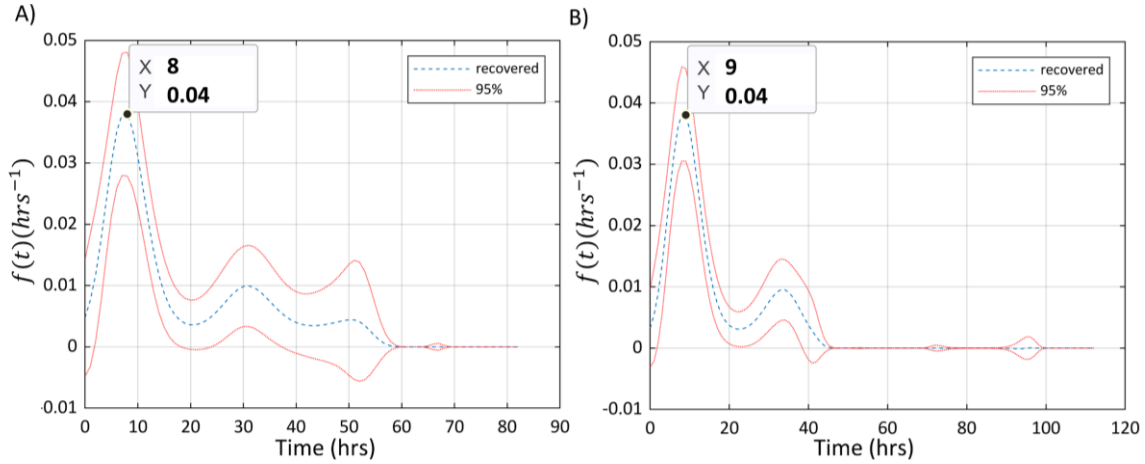

Figure 5.8: The results for the system response time for concentration spikes for events #1 (A) and #2 (B).

For the chosen 5 events to determine the response time for load, Figure 5.9 shows that the geostatistical method can precisely predict the load at the output station, as shown by

the comparison between the predicted and observed data. The response time of the system for a load spike at the input varies from 5 to 14 hours (Figure 5.10). These timescales are comparable with those evaluated from the flow data, which indicates that variation in salt load at the system outflow is mainly governed by flow variations.

5.4 Conclusion Remarks and Future research

Freshwater salinization has become an issue of concerns in many areas of the world. The management of the Occoquan reservoir and of the intake for Fairfax water treatment plant may require specific operation procedures because of freshwater salinization. The results presented in this chapter improve the understanding of water and solute transport in the Occoquan reservoir.

Detecting the travel (response) time for salt concentration and load spikes at the reservoir upstream to arrive at the Fairfax water intake can help in operating the treatment plant to avoid high concentration of salt ions in drinking water, especially because salt is added during water treatment (e.g., Na^{+},Al^{3+}, Fe^{3+}, Cl^{-}, F^{-}, ${PO_4}^{3-}$) for flocculation, disinfection, and corrosion control (Letterman, 1999; Shammas & Wang, 2015). As most ions are not fully removed by conventional treatment methods, they pass directly to the drinking water distribution system, and consequently, contributing to FSS (Kaushal et al., 2022).

A flow wave at the upstream section of the reservoir can influence the discharge through the dam within a few hours ($4-7$ hours), while a spike of salt concentration can take days ($8-9$ days) to arrive at the Fairfax water intake. Further investigation must be done to discover how to deal with such rising issue worldwide. As the sources of salt ions added to urban water systems result from different drivers, different community sectors must be involved including businesses, industry, government, and individual homeowners to reduce salt loads discharged to receiving waters, and thus the Freshwater Salinization Syndrome.

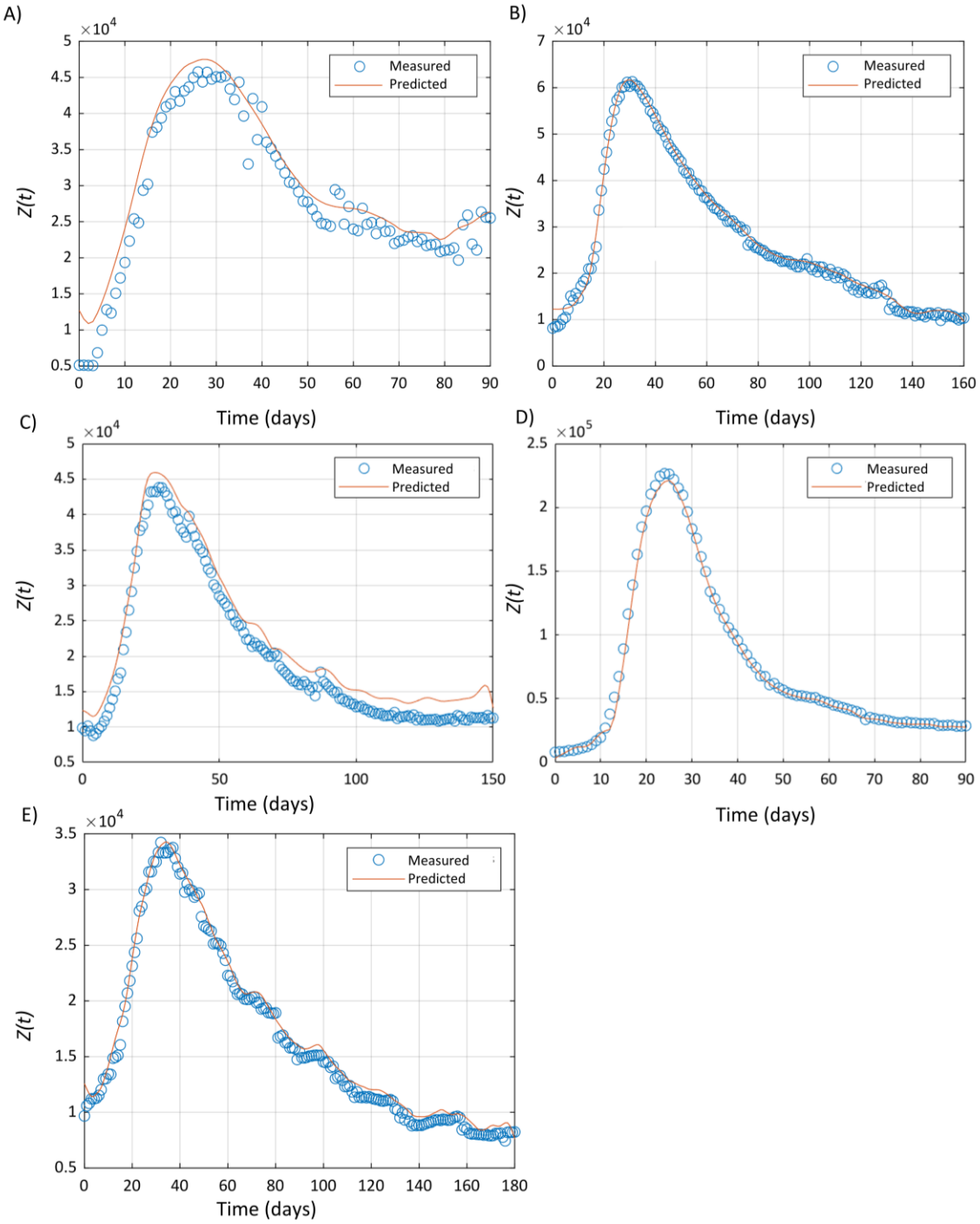

Figure 5.9: A comparison between the predicted salt load by the geostatistical method and the observed load at the output station for events #1 (A), #2 (B), #3 (C), #4 (D), and #5 (E).

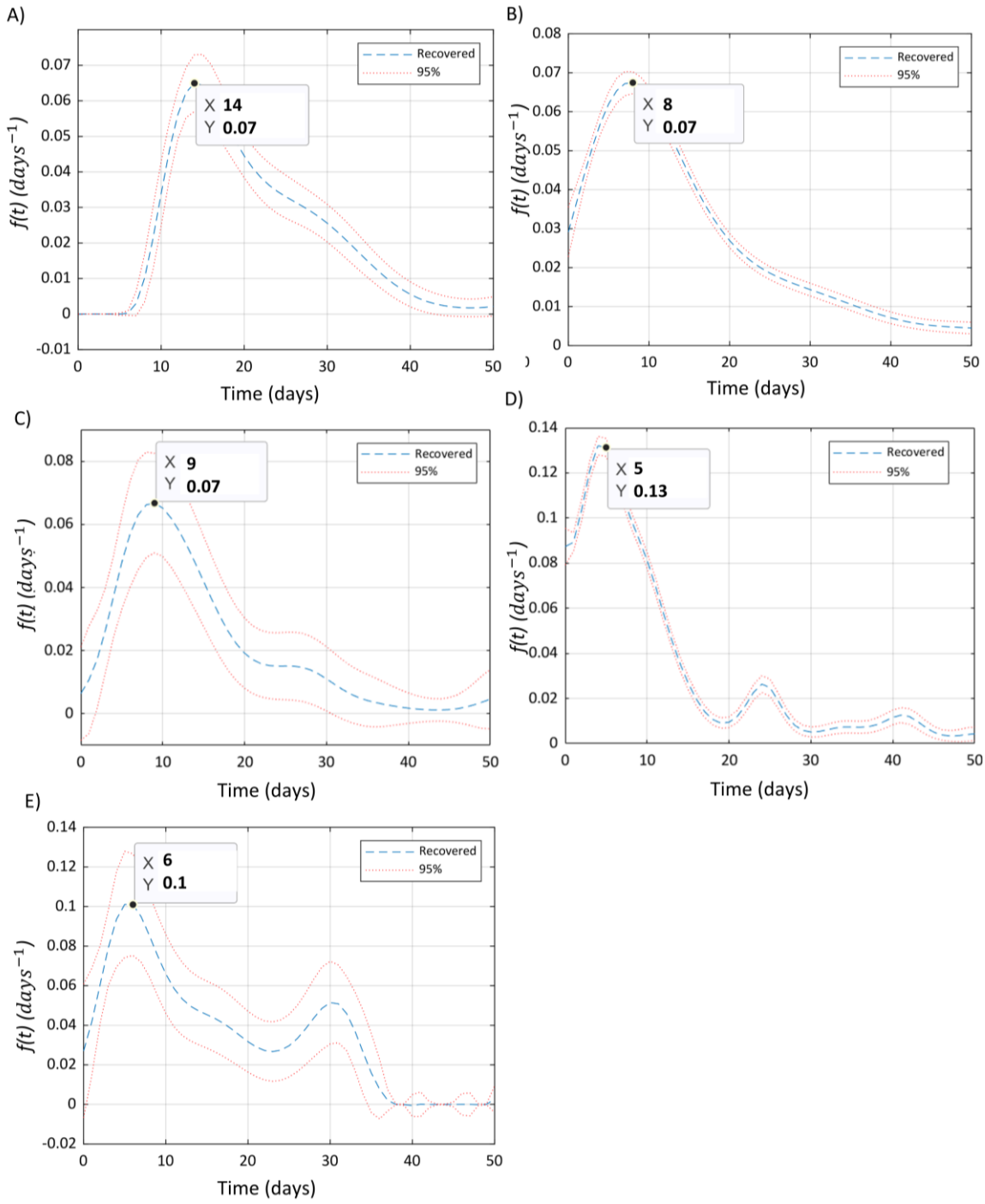

Figure 5.10: The results for the system response time for loads for events #1 (A), #2 (B), #3 (C), #4 (D), and #5 (E).

Appendices

APPENDIX A
Deriving The Diffusivity Model for conservative solute.

1. Duhamel's Theorem Solution for Turbulent mixing in the Benthic Biolayer.

The Duhamel's theorem version adopted here has three requirements that must be met (Myers, 1971): (1) the system must have zero initial state; (2) the differential equation and boundary conditions must be homogeneous except for single time-dependent boundary condition or source/sink term in the differential equation; and (3) the single nonhomogeneous term should be initially equal to zero.

By adapting the Duhamel's theorem to our system (Grant et al., 2020a), the interstitial solute concentration in the sediment can be expressed as a convolution of the time derivative of the water column concentration $c_w(\bar{t})$ and a so-called auxiliary function $c_s^A(\bar{y},\bar{t})$ where v is a dummy integration variable (Myers, 1971).

$$c_s(\bar{y},\bar{t}) = \int_0^{\bar{t}} c_s^A(\bar{y},\bar{t}-v)\frac{d}{dv}[c_w(v)H(v)]dv = \int_0^{\bar{t}} c_s^A(\bar{y},\bar{t}-v)\frac{dc_w}{dv}\,dv + c_s^A(\bar{y},\bar{t}) \quad \text{(A.1)}$$

The mass conservation for a conservative solute in a horizontally uniform systems, averaging over the turbulence timescale and assuming a constant porosity can be represented in dimensionless form:

$$\frac{\partial c_s(\bar{y},\bar{t})}{\partial \bar{t}} = \frac{\partial}{\partial \bar{y}}\left(D_{eff}(\bar{y})\frac{\partial c_s(\bar{y},\bar{t})}{\partial \bar{y}}\right) \quad \text{(A.2)}$$

$$c_s(\bar{y},\bar{t}) = \frac{C_s(\bar{y},\bar{t}) - C_{S0}}{C_{w0} - C_{S0}} \quad \text{(A.3)}$$

Where $C_s(\bar{y},\bar{t})$ is the solute concentration of solute at different time and at different vertical depths, C_{S0} is the initial solute concentration in sediment and C_{w0} is the initial concentration in the water column.

$$\bar{t} = t/t_T \geq 0, t_T = 1/\left(D_{eff0}a^2\right), \bar{y} = ay > 0 \quad \text{(A.4)}$$

Where $a(L^{-1})$ is the inverse depth scale, and its definition depends on the diffusivity profile.

$D_{eff}(\bar{y})$ representing the variation of effective diffusion over depth.

$$D_{eff}(\bar{y}) = D_{eff0}\, f(\bar{y}) \qquad \text{(A.5)}$$

Where D_{eff0} is the diffusion at the sediment water interface, and $f(\bar{y})$ is a function represents the vertical variation of diffusion.

The initial condition for Eq. (A.1) is

$$c_s(\bar{y}, \bar{t} = 0) = 0 \qquad \text{(A.6)}$$

The upper boundary condition of the sediment layer (at SWI; $\bar{y} = 0$) is correlated to the solute concentration in the water column ($c_w(\bar{t})$).

$$c_s(\bar{y} = 0, \bar{t}) = \frac{C_w(\bar{t}) - C_{s0}}{C_{w0} - C_{s0}}\, H(\bar{t}) = c_w(\bar{t}) H(\bar{t}) \qquad \text{(A.7)}$$

$$c_w(\bar{t}) = \frac{C_w(\bar{t}) - C_{s0}}{C_{w0} - C_{s0}}\,,\ c_w(\bar{t}) \in [0,1] \qquad \text{(A.8)}$$

$H(\bar{t})$ is the Heaviside step function which ensures that the upper boundary condition equals 0 at $\bar{t} \leq 0$, and otherwise at $\bar{t} > 0$. This function is used to satisfy one of the restrictions of the Duhamel's Theorem that requires the forcing Eq. (A.6) to be zero at $\bar{t} = 0$.

The sediment bed is assumed to be infinite; therefore, the lower boundary condition is

$$c_s(\bar{y} \to \infty, \bar{t}) = 0 \qquad \text{(A.9).}$$

By moving the system of equations into the Laplace domain (Eqs. (A.10a) to (A.10c)) and its auxiliary function (Eqs. (A.11a) to (A.11c)), where $\bar{s} = st_T$ is a scaled form of the Laplace transform variable s $[T^{-1}]$:

$$\bar{s}\, \tilde{c}_s(\bar{y}, \bar{t}) - \frac{d}{d\bar{y}}\left(f(\bar{y})\, \frac{d\tilde{c}_s}{d\bar{y}}\right) = 0 \qquad \text{(A.10a)}$$

$$\tilde{c}_s(\bar{y} = 0, \bar{s}) = \tilde{c}_w(\bar{s}) \qquad \text{(A.10b)}$$

$$\tilde{c}_s(\bar{y} \to \infty, \bar{s}) = 0 \qquad \text{(A.10c)}$$

$$\bar{s}\, \tilde{c}_s^A(\bar{y}, \bar{s}) - \frac{d}{d\bar{y}}\left(f(\bar{y})\, \frac{d\tilde{c}_s^A}{d\bar{y}}\right) = 0 \qquad \text{(A.11a)}$$

$$\tilde{c}_s^A(\bar{y}=0,\bar{s})=\frac{1}{\bar{s}} \qquad \text{(A.11b)}$$

$$\tilde{c}_s^A(\bar{y}\to\infty,\bar{s})=0 \qquad \text{(A.11c)}$$

The Duhamel's Theorem (A.1) can be written in the Laplace domain in the following form:

$$\tilde{c}_s(\bar{y},\bar{s})=\tilde{c}_s^A(\bar{y},\bar{s})\,[\bar{s}\,\tilde{c}_w\,(\bar{s})-c_w(0)]+\tilde{c}_s^A(\bar{y},\bar{s}),\ c_w(0)=1 \qquad \text{(A.12a)}$$

$$\tilde{c}_s(\bar{y},\bar{s})=\bar{s}\,\tilde{c}_w\,(\bar{s})\,\tilde{c}_s^A(\bar{y},\bar{s}) \qquad \text{(A.12b)}$$

By checking if the boundary conditions are satisfied for the Laplaced version of the system of equations ((A.10a) to (A.12b)). The upper boundary condition is satisfied as following:

$$\tilde{c}_s(\bar{y}=0,\bar{s})=\bar{s}\,\tilde{c}_w(\bar{s})\tilde{c}_s^A(\bar{y}=0,\bar{s})=\bar{s}\tilde{c}_w(\bar{s})(1/\bar{s})=\tilde{c}_w(\bar{s}) \qquad \text{(A.13a)}$$

As well as for the lower boundary condition:

$$\tilde{c}_s(\bar{y}\to\infty,\bar{s})=\bar{s}\,\tilde{c}_w(\bar{s})\,\tilde{c}_s^A(\bar{y}\to\infty,\bar{s})=0 \qquad \text{(A.13b)}$$

Using the so-called Green function, and its correlation to the auxiliary function is as following:

$$\bar{G}(\bar{y},\bar{t})=t_T\,G(\bar{y},\bar{t})=\frac{\partial c_s^A}{\partial \bar{t}} \qquad \text{(A.14)}$$

Therefore, Eq. (A.12b) takes on the following form using the Green function:

$$\tilde{c}_s(\bar{y},\bar{s})=\ \tilde{c}_w\,(\bar{s})\,\bar{G}(\bar{y},\bar{s}) \qquad \text{(A.15)}$$

2. Developing a General Solution accounting for the Two-way Feedback.

As in our system, the water and sediment concentrations are fully coupled through the mass flux across the SWI. Thus, the change of solute mass in the water column is equal to the rate of mass transfer across the SWI by dispersive mixing and turbulent diffusion:

$$A_b h_w\frac{dC_w}{dt}=A_b\Theta D_{eff0}\left.\frac{\partial C_s}{\partial y}\right|_{y=0,t} \qquad \text{(A.16a)}$$

In dimensionless form:

$$\frac{dc_w}{d\bar{t}} = \frac{1}{\bar{h}_w}\frac{\partial C_s}{\partial \bar{y}}\Big|_{\bar{y}=0,\bar{t}} \qquad \text{(A.16b)}$$

$$\bar{h}_w = \frac{ah_w}{\theta} \qquad \text{(A.16c)}$$

In Laplace form:

$$\bar{s}\,\tilde{c}_w(\bar{s}) - 1 = \frac{1}{\bar{h}_w}\frac{\partial \tilde{c}_s}{\partial \bar{y}}\Big|_{\bar{y}=0,\bar{s}} \qquad \text{(A.16d)}$$

Taking the derivative of Eq. (A.15) with respect to $\bar{y}$ and evaluating the expression at $\bar{y} = 0$:

$$\frac{\partial \tilde{c}_s}{\partial \bar{y}} = \tilde{c}_w(\bar{s})\frac{\partial \tilde{G}}{\partial \bar{y}}\Big|_{\bar{y}=0,\bar{s}} \qquad \text{(A.17)}$$

Substituting Eq. (A.17) into (A.16d) and solving for the concentration in the water column, we obtain the following result:

$$\tilde{c}_w(\bar{s}) = \frac{1/\bar{s}}{1-\frac{1}{\bar{s}\,\bar{h}_w}\left(\frac{\partial \tilde{G}}{\partial \bar{y}}\right)_{\bar{y}=0,\bar{s}}} \qquad \text{(A.18)}$$

The corresponding Laplace domain solution for the solute concentration in the sediment column follows by substituting Eq. (A.18) into (A.15):

$$\tilde{c}_s(\bar{y},\bar{s}) = \frac{\tilde{G}(\bar{y},\bar{s})/\bar{s}}{1-\frac{1}{\bar{s}\,\bar{h}_w}\left(\frac{\partial \tilde{G}}{\partial \bar{y}}\right)_{\bar{y}=0,\bar{s}}} \qquad \text{(A.19)}$$

The time-domain solution for solute concentration in the water column (Eq. (4.3)) and sediment bed (Eq. (4.4)) in Chapter 4 follows by taking the inverse Laplace of Eqs. (A.18) and (A.19) solving for the water column and sediment concentration, respectively.

3. Deriving the Green's Functions for the Constant and Exponential profiles.

Here, we are deriving the Green's functions for the constant (Eq. (4.1)) and the Exponential (Eq. (4.2)) profiles. The Green function G is derived from the auxiliary function (Eq. (A.14)). As it is plugged into Eqs. (4.3) and (4.4) in the Laplace form, we begin by taking the Laplace transform for both sides of Eq. (A.14)):

$$\tilde{G}(\bar{y},\bar{s}) = \bar{s}\,\tilde{c}_s^A(\bar{y},\bar{s}) - c_s^A(\bar{y},\bar{t}=0) \qquad \text{(A.20a)}$$

After applying the initial condition ($c_s^A(\bar{y},\bar{t}=0) = 0$):

$$\tilde{G}(\bar{y},\bar{s}) = \bar{s}\,\tilde{c}_s^A(\bar{y},\bar{s}) \qquad \text{(A.20b)}$$

For the C profile:

For the C profile, the depth profile function is, $f_c(\bar{y}) = 1$, which simplifies the auxiliary function's diffusion equation:

$$\bar{s}\,\tilde{c}_s^A(\bar{y},\bar{s}) - \frac{d^2\tilde{c}_s^A}{d\,\bar{y}^2} = 0 \qquad \text{(A.21a)}$$

Solving this equation in semi-infinite sediment depth, we obtain the following expression:

$$\tilde{c}_s^A(\bar{y},\bar{s}) = \frac{e^{-\bar{y}\sqrt{\bar{s}}}}{\bar{s}} \qquad \text{(A.21b)}$$

Substituting Eq. (A.21b) in (A.21a), we obtain Eq. (4.1).

For the E profile: For the choice of $f_E(\bar{y}) = e^{-y}$, the diffusion equation for the auxiliary function can be written as follows:

$$\frac{\partial c_s^A}{\partial \bar{t}} = \frac{\partial}{\partial \bar{y}}\left[e^{-\bar{y}}\frac{\partial c_s^A}{\partial \bar{y}}\right] = e^{-\bar{y}}\frac{\partial^2 c_s^A}{\partial \bar{y}^2} - e^{-\bar{y}}\frac{\partial c_s^A}{\partial \bar{y}} \qquad \text{(A.22a)}$$

Following the approach outlined by Yates (1992) Eq. (A.22a) can simplified by a change of the depth-coordinate, $\xi = e^{\bar{y}}$:

$$\frac{\partial c_s^A}{\partial \bar{t}} = \xi'\frac{\partial}{\partial \xi}\left[e^{-\bar{y}} * \xi'\frac{\partial c_s^A}{\partial \xi}\right] = \xi\,\frac{\partial^2 c_s^A}{\partial \xi^2}, \xi = e^{\bar{y}}, \xi' = \frac{\partial \xi}{\partial \bar{y}}, \bar{y} \geq 0 \qquad \text{(A.22b)}$$

The transformed initial condition and upper and lower boundary conditions are as follow:

$$c_s^A(\xi, \bar{t} = 0) = 0, \xi \geq 1 \qquad \text{(A.22c)}$$

$$c_s^A(\xi = 1, \bar{t}) = H(\bar{t}) \qquad \text{(A.22d)}$$

$$c_s^A(\xi \to \infty, \bar{t}) = 0 \qquad \text{(A.22e)}$$

where $H(\bar{t})$ is the Heaviside function $\begin{cases} 0 & \bar{t} \leq 0 \\ 1 & \bar{t} > 0 \end{cases}$.

Moving Eqs. (A.22b) to (A.22e) into the Laplace domain results in following equations:

$$\bar{s}\tilde{c}_s^A(\xi, \bar{s}) = \xi \frac{\partial^2 c_s^A}{\partial \bar{\xi}^2}, \xi \geq 1 \qquad \text{(A.23a)}$$

$$\tilde{c}_s^A(\xi = 1, \bar{s}) = 1/\bar{s} \qquad \text{(A.23b)}$$

$$\tilde{c}_s^A(\xi \to \infty, \bar{s}) = 0 \qquad \text{(A.23c)}$$

The system of Eqs. (A.23a) to (A.23c) can be solved and results in the following Laplace transformed auxiliary function:

$$\tilde{c}_s^A(\xi, \bar{s}) = \frac{\sqrt{\xi} K_1\left(2\sqrt{\bar{s}\xi}\right)}{\bar{s} K_1(2\sqrt{\bar{s}})}, \bar{y} \geq 0 \qquad \text{(A.24a)}$$

Back substituting the depth-coordinate transformation, we obtain the final result of the auxiliary function as following:

$$\tilde{c}_s^A(\bar{y}, \bar{s}) = \frac{\sqrt{e^{\bar{y}}} K_1\left(2\sqrt{\bar{s}e^{\bar{y}}}\right)}{\bar{s} K_1(2\sqrt{\bar{s}})}, \bar{y} \geq 0 \qquad \text{(A.24b)}$$

By substituting equation (A.24b) into (A.20b) results in Eq. (4.3).

APPENDIX B
Deriving the Diffusivity Model for Reactive Solute.

1. General Equation for Reactive Solute.

The mass conservation for a reactive solute in a horizontally uniform systems, averaging over the turbulence time scale and assuming a constant porosity and a constant reaction (sink) rate, and in dimensionless form:

$$\frac{\partial c_s(\bar{y},\bar{t})}{\partial \bar{t}} = \frac{\partial}{\partial \bar{y}}\left(D_{eff}(y)\frac{\partial c_s(\bar{y},\bar{t})}{\partial \bar{y}}\right) - \bar{\mu}\, c_s(\bar{y},\bar{t}) \qquad \text{(B.1)}$$

where $\bar{\mu} = \mu/a^2 D_{eff,0}$, and μ represents the solute reaction/degradation/sink rate $[T^{-1}]$.

Eq. (B.1) can take on the following form:

$$\frac{\partial c_s(\bar{y},\bar{t})}{\partial \bar{t}} = L\, c_s(\bar{y},\bar{t}) \qquad \text{(B.2)}$$

where:

$$L = \frac{\partial}{\partial \bar{y}}\left(f(\bar{y})\frac{\partial}{\partial \bar{y}}\right) - \bar{\mu} \qquad \text{(B.3)}$$

The boundary conditions for this system is the same as in Eqs. (A.6), (A.7) and (A.9).

By moving the system of equations into the Laplace domain (Eqs. (B.4a) to (B.4c)) and its auxiliary function (Eqs. (B.5a) to (B.5c)):

$$\bar{s}\,\tilde{c}_s(\bar{y},s) - 0 = L\,\tilde{c}_s(\bar{y},s) \qquad \text{(B.4a)}$$

$$\tilde{c}_s(\bar{y}=0,\bar{s}) = \tilde{c}_w(\bar{s}) \qquad \text{(B.4b)}$$

$$\tilde{c}_s(\bar{y}\to\infty,\bar{s}) = 0 \qquad \text{(B.4c)}$$

$$\bar{s}\,\tilde{c}_s^A(\bar{y},\bar{s}) - 0 = L\,\tilde{c}_s^A(\bar{y},\bar{s}) \qquad \text{(B.5a)}$$

$$\tilde{c}_s^A(\bar{y}=0,\bar{s})=\frac{1}{\bar{s}} \qquad \text{(B.5b)}$$

$$\tilde{c}_s^A(\bar{y}\to\infty,\bar{s})=0 \qquad \text{(B.5c)}$$

The Duhamel's Theorem for the system can be written in the Laplace domain as in APPENDIX A for the conservative solute:

$$\tilde{c}_s(\bar{y},\bar{s})=\bar{s}\,\tilde{c}_w\,(\bar{s})\,\tilde{c}_s^A(\bar{y},\bar{s}) \qquad \text{(B.6)}$$

2. Developing a General Solution accounting for the Two-way feedback.

Similar to the conservative solute, here we account for the two-way feedback between the water column and the sediment. Thus, the change of solute mass in the water column is equal to the rate of mass transfer across the SWI by dispersive mixing and turbulent diffusion:

$$A_b h_w \frac{dC_w}{dt}=A_b\Theta D_{eff0}\frac{\partial C_s}{\partial y}\Big|_{y=0,t} \qquad \text{(B.7)}$$

Following the same procedures as in APPENDIX A, general solutions for the solute concentration in the water column and in the sediment can be derived to be as following, in the time domain:

- For the water column:

$$\tilde{c}_w(\bar{t})=\ L^{-1}\left[\frac{1/\bar{s}}{1-\frac{1}{\bar{s}\,\bar{h}_w}\left(\frac{\partial\tilde{G}}{\partial\bar{y}}\right)_{\bar{y}=0,\bar{s}}}\right] \qquad \text{(B.8)}$$

- For the sediment:

$$\tilde{c}_s(\bar{y},\bar{t})=\ L^{-1}\left[\frac{\tilde{G}(\bar{y},\bar{s})/\bar{s}}{1-\frac{1}{\bar{s}\,\bar{h}_w}\left(\frac{\partial\tilde{G}}{\partial\bar{y}}\right)_{\bar{y}=0,\bar{s}}}\right] \qquad \text{(B.9)}$$

The time-domain solution for solute concentration in the water column (Eq. (4.3)) and sediment bed (Eq. (4.4)) in Chapter 4 follows by taking the inverse Laplace of Eqs.

(B.8) and (B.9) and solving for the water column and sediment concentration, respectively.

3. Deriving the Green's Functions for the Constant and Exponential profiles for the reactive solute.

Here, we are deriving the Green's functions for the constant (Eq. (4.1)) and the Exponential (Eq. (4.2)) profiles in order to be plugged in Eqs. (B.8) and (B.9) for reactive solutes. The Green function G is derived from the auxiliary function as following:

$$\tilde{G}(\bar{y},\bar{s}) = \bar{s}\,\tilde{c}_s^A(\bar{y},\bar{s}) - c_s^A(\bar{y},\bar{t}=0) \qquad \text{(B.10a)}$$

After applying the initial condition ($c_s^A(\bar{y},\bar{t}=0)=0$):

$$\tilde{G}(\bar{y},\bar{s}) = \bar{s}\,\tilde{c}_s^A(\bar{y},\bar{s}) \qquad \text{(B.10b)}$$

For the C profile:

For the C profile, the depth profile function is, $f_c(\bar{y}) = 1$, which simplifies Eq. (B.3) to:

$$L = \frac{\partial^2}{\partial \bar{y}^2} - \bar{\mu} \qquad \text{(B.11a)}$$

and therefore, the Auxiliary function can be written as following:

$$\bar{s}\,\tilde{c}_s^A(\bar{y},\bar{s}) = \left(\frac{\partial^2}{\partial \bar{y}^2} - \bar{\mu}\right)\tilde{c}_s^A(\bar{y},\bar{s}) \qquad \text{(B.11b)}$$

$$\bar{s}\,\tilde{c}_s^A(\bar{y},\bar{s}) - \frac{\partial^2}{\partial \bar{y}^2}\tilde{c}_s^A(\bar{y},\bar{s}) - \bar{\mu}\,\tilde{c}_s^A(\bar{y},\bar{s}) = 0 \qquad \text{(B.11c)}$$

Solving this equation in semi-infinite sediment depth, we obtain the following expression for the Auxiliary function:

$$\tilde{c}_s^A(\bar{y},\bar{s}) = \frac{e^{-\bar{y}\sqrt{\bar{s}+\bar{\mu}}}}{\bar{s}} \qquad \text{(B.12a)},$$

and therefore, the Green function is as following:

$$\tilde{G}(\bar{y},\bar{s}) = \bar{s}\,\tilde{c}_s^A(\bar{y},\bar{s}) = e^{-\bar{y}\sqrt{\bar{s}+\bar{\mu}}} \qquad \text{(B.12b)}$$

For the E profile:

For the choice of $f_E(\bar{y}) = e^{-y}$, the diffusion equation for the auxiliary function can be written as follows:

$$\bar{s}\,\tilde{c}_s^A(\bar{y},\bar{s}) = \frac{\partial}{\partial \bar{y}}\left(e^{-\bar{y}}\frac{\partial}{\partial \bar{y}}\right)\tilde{c}_s^A(\bar{y},\bar{s}) - \bar{\mu}\,\tilde{c}_s^A(\bar{y},\bar{s}) \qquad \text{(B.13a)}$$

Similarly to Eq. (A.22b), Eq. (B.13a) can simplified by a change of the depth-coordinate, $\xi = e^{\bar{y}}$:

$$(\bar{s}+\bar{\mu})\tilde{c}_s^A(\bar{\xi},\bar{s}) = \xi\,\frac{\partial^2 c_s^A(\bar{\xi},\bar{s})}{\partial \bar{\xi}^2}, \xi = e^{\bar{y}}, \bar{y} \geq 0 \qquad \text{(B.13b)}$$

The transformed initial condition and upper and lower boundary conditions in are as following:

$$c_s^A(\xi, \bar{t}=0) = 0, \xi \geq 1 \qquad \text{(B.13c)}$$

$$c_s^A(\xi = 1, \bar{t}) = H(\bar{t}) \qquad \text{(B.13d)}$$

$$c_s^A(\xi \to \infty, \bar{t}) = 0 \qquad \text{(B.13e)}$$

where $H(\bar{t})$ is the Heaviside function $\begin{cases} 0 & \bar{t} \leq 0 \\ 1 & \bar{t} > 0 \end{cases}$.

Moving Eqs. (B.13d) and (B.13e) into the Laplace domain results in following equations:

$$\tilde{c}_s^A(\xi = 1, \bar{s}) = 1/\bar{s} \qquad \text{(B.14a)}$$

$$\tilde{c}_s^A(\xi \to \infty, \bar{s}) = 0 \qquad \text{(B.14b)}$$

The previous system of equations can be solved and results in the following Laplace transformed auxiliary function:

$$\tilde{c}_s^A(\xi,\bar{s}) = \frac{\sqrt{\xi}K_1\left(2\sqrt{(\bar{s}+\bar{\mu})\xi}\right)}{\bar{s}K_1\left(2\sqrt{(\bar{s}+\bar{\mu})}\right)}, \bar{y} \geq 0 \qquad \text{(B.15a)}$$

Back substituting the depth-coordinate transformation, we obtain the final result of the auxiliary function as following:

$$\tilde{c}_s^A(\bar{y},\bar{s}) = \frac{\sqrt{e^{\bar{y}}}K_1\left(2\sqrt{(\bar{s}+\bar{\mu})e^{\bar{y}}}\right)}{\bar{s}K_1\left(2\sqrt{(\bar{s}+\bar{\mu})}\right)}, \bar{y} \geq 0 \qquad \text{(B.15b),}$$

and therefore, the Green function is as following:

$$\tilde{G}(\bar{y},\bar{s}) = \bar{s}\,\tilde{c}_s^A(\bar{y},\bar{s}) = \frac{\sqrt{e^{\bar{y}}}K_1\left(2\sqrt{(\bar{s}+\bar{\mu})e^{\bar{y}}}\right)}{K_1\left(2\sqrt{(\bar{s}+\bar{\mu})}\right)} \qquad \text{(B.15c)}$$

APPENDIX C
The Geostatistical Method.

The objective is to estimate an unknown function, in this case the release history ($f(t)$) from a point source in reservoir upstream to an observation point in the downstream, which is a function of time. The unknown function is represented as a random process because there is uncertainty associated with the function and its true value may never be found. However, we can imagine the set of all possible functions/solutions that fit the data, and are consistent with additional information. In a Bayesian approach, each of these functions is assigned a probability that is a solution. The best solution is the one with highest probability along with its covariance as a measure of the estimation uncertainty.

If the time domain is discretized in n instants t_j , the observations can be related to the source by the general expression:

$$Z_i = H_{ij}.f_i + v_i \qquad \text{(C.1)}$$

Z_i is an $[mx1]$ vector contains the observations at t_j, H_{ij} is a $[mxn]$ matrix represents the model function, f_i is $[nx1]$ vector represents the discretized release history, and v_i is an $[mx1]$ vector represents the measurement errors.

H_{ij} is expressed as following:

$$H_{ij} = M_{in}(t_i - t_j) \qquad \text{(C.2)}$$

where $M_{in}(t_i - t_j)$ corresponds to the source value at $t = t_i - t_j$. When the value $t_i - t_j$ is less than Zero, it accounts the legacy effect. For example, a concentration spike measured at time Zero at the output corresponds to a previous spike recorded at the model source. In our case, M_{in} represents salt concentration, load, or water flow.

As the problem dealt with here is an ill-posed problem (Boano et al., 2005), it is necessary to remove this ill-posedness. f_i is assumed to be a gaussian joint distribution with mean (Eq. (C.3a)) and covariance (Eq. (C.3b)):

$$E[f] = XB \qquad \text{(C.3a)}$$

$$E[(f - XB)(f - XB)^T] = Q(\Theta) \qquad \text{(C.3b)}$$

where X is an $[nx1]$ unit vector, B is the unknown mean, and Θ is a vector of unknown structural parameters.

The error v is also Gaussian, with a zero mean and covariance matrix $R = \sigma xI$, where I is the $[mxm]$ identity matrix.

Two models are proposed to represent the covariance (Eq. (C.3b)): Linear (Eq. (C.4a)), and Gaussian (Eq. (C.4b)):

$$Q\left(t_i - t_j|\Theta\right) = \sigma^2 - B^2\left|t_i - t_j\right|, \Theta^T = [\sigma, B] \qquad \text{(C.4a)}$$

$$Q\left(t_i - t_j|\Theta\right) = \sigma^2 exp\left[-\frac{(t_i - t_j)^2}{l^2}\right], \Theta^T = [\sigma, l] \qquad \text{(C.4b)}$$

Then the pdf's can be written as following:

$$p(f|B, \Theta) \ \alpha \ |Q|^{-1/2} exp\left[\frac{-1}{2}(f - XB)^T Q^{-1}(f - XB)\right] \qquad \text{(C.5a)}$$

$$p(z|f) \ \alpha \ |R|^{-1/2} exp\left[\frac{-1}{2}(z - Hf)^T R^{-1}(z - Hf)\right] \qquad \text{(C.5b)}$$

The geostatistical method consists of two steps: fist, estimating the structural parameters Θ (structural analysis) using the principle of maximum likelihood, then determining the release history $f(t)$ by the kriging estimator.

- **First step: The Structural Analysis.**

The observational pdf conditional on Θ is determined as

$$p(z|\Theta) = \int_B p(z|B, \Theta)\, dB = \int_B \int_f p(z, f|B, \Theta) df\, dB = \int_B \int_f p(z|f) p(f|B, \Theta) df\, dB \qquad \text{(C.6)}$$

The previous expression is maximized with respect to Θ, which is equivalent to minimizing

$$L(\Theta) = -\ln[p(z|\Theta)]\ \alpha\ \frac{1}{2}\ln(|\sum|.\,|X^T H^T \sum^{-1} HX|) + \frac{1}{2} z^T \Xi\, z \qquad \text{(C.7a)}$$

$$\sum = HQH^T + R \qquad \text{(C.7b)}$$

$$\Xi = \sum^{-1} - \sum^{-1} HX(X^T H^T \sum^{-1} HX)^{-1} X^T H^T \sum^{-1} \qquad \text{(C.7c)}$$

The problem can be solved iteratively using the Gauss-Newton method, with the addition of a line search (Press, 1992) to improve the convergence rate. If the lth estimate $\widehat{\Theta}_l$ is known, the next estimate can be found as

$$\widehat{\Theta}_{l+1} = \widehat{\Theta}_l - \rho F^{-1} g \qquad \text{(C.8)}$$

where ρ is a multiplicative factor for the line search.

$$g_i = \frac{\partial L}{\partial \Theta_i} = \frac{1}{2}\ Tr\left[\Xi\ \frac{\partial \Sigma}{\partial \Theta_i}\right] - \frac{1}{2} z^T \left[\Xi\ \frac{\partial \Sigma}{\partial \Theta_i}\ \Xi\right] z \qquad \text{(C.8a)}$$

$$F_{ij} = E\left[\frac{\partial^2 L}{\partial \Theta_i \partial \Theta_i}\right] = \frac{1}{2}\ Tr\left[\Xi\ \frac{\partial \Sigma}{\partial \Theta_i}\ \Xi\ \frac{\partial \Sigma}{\partial \Theta_j}\right] \qquad \text{(C.8b)}$$

The routine eventually converges to the final estimate $\widehat{\Theta}$ of the structural parameters. The matrix F^{-1} also represents an estimate of the covariance matrix of Θ.

- **Second step: Kriging Estimator for $\boldsymbol{f(t)}$.**

A linear estimator of kriging is

$$\hat{f} = \Lambda z \qquad \text{(C.9a)}$$

which is unbiased and minimizes the estimate error variance, that is,

$$E\left[\widehat{f} - f\right] = 0 \qquad \text{(C.9b)}$$

$$\min_{\widehat{f}} E[(\widehat{f} - f)(\widehat{f} - f)^T] \qquad \text{(C.9c)}$$

After updating the matrices Q and $\sum$ with the estimated structural parameters $\widehat{\Theta}$, the following system has to be solved

$$\begin{bmatrix} \sum & HX \\ (HX)^T & 0 \end{bmatrix} \begin{bmatrix} \Lambda^T \\ M \end{bmatrix} = \begin{bmatrix} HQ \\ X^T \end{bmatrix} \qquad \text{(C.10)}$$

where Λ is an $[nxm]$ matrix of coefficients and M is a $[1xn]$ vector of multipliers. This system is equivalent to Eqs. (C.9b) and (C.9c).

After solving Eq. (C.10), the value of Λ can be substituted in Eq. (C.9a) and the value of $f(t)$ is found.

The application of the kriging Eq. (C.10) corresponds to discarding, from the ensemble of the release histories, those that are not consistent with the observations z (Boano et al., 2015). The mean of the release history is then estimated by Eq. (C.9a), while its covariance matrix V can be evaluated as

$$V = -XM + Q - QH^T\Lambda^T \qquad \text{(C.11)}$$

The disadvantage of the usage of Eq. (C.1) is that the application of the geostatistical method on a linear model, as in the case here, allows the solution to present negative values. This is a numerical problem due to the $f(t)$ oscilations around the Zero; however, physically, this is not acceptable.

To avoid this problem in the code, the following function is considered to avoid the negativity:

$$\hat{f} = \alpha(f^{1/\alpha} - 1) \qquad \text{(C.12a)}$$

where α is prior defined parameters that constrain $\hat{f}$ to not be negative

$$\hat{f} + \alpha > 0 \qquad \text{(C.12b)}$$

Provided this condition is respected, it is a good choice to adopt a small value for a, since this will improve the convergence rate. Other transformations for the variable can also be chosen.

Nomenclature

Abbreviation:

AB	Alternate Bars
AD test	Anderson Darling test
AICc	Corrected Akaike Information Criterion
BIC	Bayesian Information Criterion
CDF	Cumulative Distribution Function
$CV.Err$	Cross-validation prediction error
D	Dunes
Da	Damköhler number
DBL	Diffusive Boundary Layer
EXP	Exponential Distribution
FB	Flat Bed
FR	Fréchet Distribution
FSS	Freshwater Salinity Syndrome
GAM	Gamma Distribution
Hrs	Hours
HZ	Hyporheic Zone
LN	Lognormal Distribution
MLE	Maximum Likelihood Estimation
MLR	Multiple Linear Regression
pdf	Probability Density Function
RE	Relative Error
R^2	Coefficient of Determination
RMSE	Root Mean Square Error

RSF	Reaction Significance Factor
RTDs	Residence Times Distributions
RTs	Hyporheic Residence times
SE	Standard Error
SWE	Surface Water Elevation
SWI	Sediment Water Interface

REFERENCES

Akaike, H. (1974). A New Look at the Statistical Model Identification. *IEEE Transactions on Automatic Control*, *19*(6), 716–723. https://doi.org/10.1109/TAC.1974.1100705

Anderson, T. W., & Darling, D. A. (1952). Asymptotic theory of certain" goodness of fit" criteria based on stochastic processes. *The Annals of Mathematical Statistics*, 193–212.

Azizian, M., Boano, F., Cook, P. L. M., Detwiler, R. L., Rippy, M. A., & Grant, S. B. (2017). Ambient groundwater flow diminishes nitrate processing in the hyporheic zone of streams. *Water Resources Research*, *53*(5), 3941–3967.

Azizian, M., Grant, S. B., Kessler, A. J., Cook, P. L. M., Rippy, M. A., & Stewardson, M. J. (2015). Bedforms as biocatalytic filters: A pumping and streamline segregation model for nitrate removal in permeable sediments. *Environmental Science & Technology*, *49*(18), 10993–11002.

Bardini, L., Boano, F., Cardenas, M. B., Revelli, R., & Ridolfi, L. (2012). Nutrient cycling in bedform induced hyporheic zones. *Geochimica et Cosmochimica Acta*, *84*, 47–61. https://doi.org/10.1016/j.gca.2012.01.025

Battin, T. J., Besemer, K., Bengtsson, M. M., Romani, A. M., & Packmann, A. I. (2016). The ecology and biogeochemistry of stream biofilms. In *Nature Reviews Microbiology* (Vol. 14, Issue 4, pp. 251–263). Nature Publishing Group. https://doi.org/10.1038/nrmicro.2016.15

Baxter, C. v, & Hauer, F. R. (2000). Geomorphology, hyporheic exchange, and selection of spawning habitat by bull trout (Salvelinus confluentus). *Canadian Journal of Fisheries and Aquatic Sciences*, *57*(7), 1470–1481.

Beaulieu, J. J., Tank, J. L., Hamilton, S. K., Wollheim, W. M., Hall, R. O., Mulholland, P. J., Peterson, B. J., Ashkenas, L. R., Cooper, L. W., Dahm, C. N., & others. (2011). Nitrous oxide emission from denitrification in stream and river networks. *Proceedings of the National Academy of Sciences*, *108*(1), 214–219.

Bencala, K. E. (1983). Simulation of solute transport in a mountain pool-and-riffle stream with a kinetic mass transfer model for sorption. *Water Resources Research*, *19*(3), 732–738.

Bergman, T., Bergman, T., Incropera, F., & Dewitt, D. (2011). *Fundamentals of heat and mass transfer*. https://books.google.com/books?hl=en&lr=&id=vvyIoXEywMoC&oi=fnd&pg=PR21&dq=Bergman+et+al.,+2011&ots=8KslRVdTG5&sig=92O6mnCZ-RSnfKxaRlfp9Ul7oes

Bhide, S. v., Grant, S. B., Parker, E. A., Rippy, M. A., Godrej, A. N., Kaushal, S., Prelewicz, G., Saji, N., Curtis, S., Vikesland, P., Maile-Moskowitz, A., Edwards, M., Lopez, K. G., Birkland, T. A., & Schenk, T. (2021). Addressing the contribution of indirect potable reuse to inland freshwater salinization. *Nature Sustainability*, *4*(8), 699–707. https://doi.org/10.1038/s41893-021-00713-7

Boano, F., Harvey, J. W., Marion, A., Packman, A. I., Revelli, R., Ridolfi, L., & Wörman, A. (2014). Hyporheic flow and transport processes: Mechanisms, models, and biogeochemical implications. In *Reviews of Geophysics* (Vol. 52, Issue 4, pp. 603–679). Blackwell Publishing Ltd. https://doi.org/10.1002/2012RG000417

Boano, F., Packman, A. I., Cortis, A., Revelli, R., & Ridolfi, L. (2007). A continuous time random walk approach to the stream transport of solutes. *Water Resources Research*, *43*(10).

Boano, F., Revelli, R., & Ridolfi, L. (2005). Source identification in river pollution problems: A geostatistical approach. *Water Resources Research*, *41*(7), 1–13. https://doi.org/10.1029/2004WR003754

Boano, F., Revelli, R., & Ridolfi, L. (2009). Quantifying the impact of groundwater discharge on the surface–subsurface exchange. *Hydrological Processes: An International Journal*, *23*(15), 2108–2116.

Boano, F., Revelli, R., & Ridolfi, L. (2011). Water and solute exchange through flat streambeds induced by large turbulent eddies. *Journal of Hydrology*, *402*(3–4), 290–296.

Boano, F., Scibetta, M., Ridolfi, L., & Giustolisi, O. (2015). Water distribution system modeling and optimization: A case study. *Procedia Engineering*, *119*(1), 719–724. https://doi.org/10.1016/j.proeng.2015.08.925

Bottacin-Busolin, A. (2019). Modeling the Effect of Hyporheic Mixing on Stream Solute Transport. *Water Resources Research*, *55*(11), 9995–10011.

Bottacin-Busolin, A., & Marion, A. (2010). Combined role of advective pumping and mechanical dispersion on time scales of bed form–induced hyporheic exchange. *Water Resources Research*, *46*(8).

Bouzourra, H., Bouhlila, R., Elango, L., Slama, F., & Ouslati, N. (2015). Characterization of mechanisms and processes of groundwater salinization in irrigated coastal area using statistics, GIS, and hydrogeochemical investigations. *Environmental Science and Pollution Research*, *22*(4), 2643–2660. https://doi.org/10.1007/s11356-014-3428-0

Cardenas, M. B. (2007). Potential contribution of topography-driven regional groundwater flow to fractal stream chemistry: Residence time distribution analysis of Tóth flow. *Geophysical Research Letters*, *34*(5).

Cardenas, M. B., & Wilson, J. L. (2006). The influence of ambient groundwater discharge on exchange zones induced by current–bedform interactions. *Journal of Hydrology*, *331*(1–2), 103–109.

Cardenas, M. B., Wilson, J. L., & Haggerty, R. (2008). Residence time of bedform-driven hyporheic exchange. *Advances in Water Resources*, *31*(10), 1382–1386.

Caruso, A., Boano, F., Ridolfi, L., Chopp, D. L., & Packman, A. (2017). Biofilm-induced bioclogging produces sharp interfaces in hyporheic flow, redox conditions, and microbial community structure. *Geophysical Research Letters*, *44*(10), 4917–4925. https://doi.org/10.1002/2017GL073651

Chandler, I. D., Guymer, I., Pearson, J. M., & van Egmond, R. (2016). Vertical variation of mixing within porous sediment beds below turbulent flows. *Water Resources Research*, *52*(5), 3493–3509.

Domenico, P., & Schwartz, F. (1998). *Physical and chemical hydrogeology*. https://www.academia.edu/download/30924656/99971569.pdf

Dugan, H. A., Bartlett, S. L., Burke, S. M., Doubek, J. P., Krivak-Tetley, F. E., Skaff, N. K., Summers, J. C., Farrell, K. J., McCullough, I. M., Morales-Williams, A. M., Roberts, D. C., Ouyang, Z., Scordo, F., Hanson, P. C., & Weathers, K. C. (2017). Salting our freshwater lakes. *Proceedings of the National Academy of Sciences of the United States of America*, *114*(17), 4453–4458. https://doi.org/10.1073/pnas.1620211114

Elliott, A. H., & Brooks, N. H. (1997a). Transfer of nonsorbing solutes to a streambed with bed forms: Laboratory experiments. *Water Resources Research*, *33*(1), 137–151.

Elliott, A. H., & Brooks, N. H. (1997b). Transfer of nonsorbing solutes to a streambed with bed forms: Theory. *Water Resources Research*, *33*(1), 123–136. https://doi.org/10.1029/96WR02784

Engmann, S., & Cousineau, D. (2011). Comparing distributions: the two-sample anderson-darling test as an alternative to the kolmogorov-smirnoff test. *Journal of Applied Quantitative Methods*, *6*(3).

Eylers, H. (1994). *Transport of adsorbing metal ions between stream water and sediment bed in a laboratory flume*. https://search.proquest.com/openview/1e4532181b97794663cabbd4ff03b791/1?pq-origsite=gscholar&cbl=18750&diss=y&casa_token=6-qVge2mIx4AAAAA:0uRqwOIUUXen_pzN3ZAnDfRwlkmJmUpeaD-dTEHT-jKjoFQGGQIrWWSL4WTblQNwBjxMu0gNSw

Feminella, J. W., & Walsh, C. J. (2005). Urbanization and stream ecology: an introduction to the series. *Journal of the North American Benthological Society*, *24*(3), 585–587.

Ferreira da Silva, A. M., & Yalin, M. S. (2017). Fluvial processes: 2nd edition. In *Fluvial Processes: 2nd Edition*. CRC Press. https://doi.org/10.4324/9781315206189

Fox, A., Boano, F., & Arnon, S. (2014). Impact of losing and gaining streamflow conditions on hyporheic exchange fluxes induced by dune-shaped bed forms. *Water Resources Research*, *50*(3), 1895–1907.

Franca, M. J., & Brocchini, M. (2015). Turbulence in rivers. In *GeoPlanet: Earth and Planetary Sciences* (pp. 51–78). Springer Verlag. https://doi.org/10.1007/978-3-319-17719-9_2

Freeman, J. B., & Dale, R. (2013). Assessing bimodality to detect the presence of a dual cognitive process. *Behavior Research Methods*, *45*(1), 83–97. https://doi.org/10.3758/s13428-012-0225-x

Frei, S., Azizian, M., Grant, S. B., Zlotnik, V. A., & Toundykov, D. (2019). Analytical modeling of hyporheic flow for in-stream bedforms: Perturbation method and implementation. *Environmental Modelling & Software*, *111*, 375–385.

G Schwarz. (1978). Estimating the dimension of a model. *The Annals of Statistics*, 461–464. https://www.jstor.org/stable/2958889

Galella, J. G., Kaushal, S. S., Wood, K. L., Reimer, J. E., & Mayer, P. M. (2021). Sensors track mobilization of 'chemical cocktails' in streams impacted by road salts in the Chesapeake Bay watershed. *Environmental Research Letters*, *16*(3), 035017. https://doi.org/10.1088/1748-9326/abe48f

Galloway, J., Fox, A., Lewandowski, J., & Arnon, S. (2019). The effect of unsteady streamflow and stream-groundwater interactions on oxygen consumption in a sandy streambed. *Scientific Reports*, *9*(1), 1–11.

Glose, T. J., Lowry, C. S., & Hausner, M. B. (2019). Vertically Integrated Hydraulic Conductivity: A New Parameter for Groundwater-Surface Water Analysis. *Groundwater*, *57*(5), 727–736. https://doi.org/10.1111/gwat.12864

Gomez, J. D., Wilson, J. L., & Cardenas, M. B. (2012). Residence time distributions in sinuosity-driven hyporheic zones and their biogeochemical effects. *Water Resources Research*, *48*(9).

Gomez-Velez, J. D., Harvey, J. W., Cardenas, M. B., & Kiel, B. (2015). Denitrification in the Mississippi River network controlled by flow through river bedforms. *Nature Geoscience*, *8*(12), 941–945.

Gomez-Velez, J. D., Krause, S., & Wilson, J. L. (2014). Effect of low-permeability layers on spatial patterns of hyporheic exchange and groundwater upwelling. *Water Resources Research*, *50*(6), 5196–5215.

Grant, S. B., Gomez-Velez, J. D., & Ghisalberti, M. (2018). Modeling the effects of turbulence on hyporheic exchange and local-to-global nutrient processing in streams. *Water Resources Research*, *54*(9), 5883–5889.

Grant, S. B., Gomez-Velez, J. D., Ghisalberti, M., Guymer, I., Boano, F., Roche, K., & Harvey, J. (2020a). A one-dimensional model for turbulent mixing in the benthic biolayer of stream and coastal sediments. *Water Resources Research*, e2019WR026822.

Grant, S. B., Litton-Mueller, R. M., & Ahn, J. H. (2011). Measuring and modeling the flux of fecal bacteria across the sediment-water interface in a turbulent stream. *Water Resources Research*, *47*(5).

Grant, S. B., & Marusic, I. (2011). Crossing turbulent boundaries: Interfacial flux in environmental flows. *Environmental Science and Technology*, *45*(17), 7107–7113. https://doi.org/10.1021/es201778s

Grant, S. B., Monofy, A., Boano, F., Gomez-Velez, J. D., Guymer, I., Harvey, J., & Ghisalberti, M. (2020b). Unifying advective and diffusive descriptions of bedform pumping in the benthic biolayer of streams. *Water Resources Research*, *56*(11), e2020WR027967.

Grant, S. B., Stewardson, M. J., & Marusic, I. (2012). Effective diffusivity and mass flux across the sediment-water interface in streams. *Water Resources Research*, *48*(5).

Grant, S. B., Stolzenbach, K., Azizian, M., Stewardson, M. J., Boano, F., & Bardini, L. (2014). First-order contaminant removal in the hyporheic zone of streams: Physical insights from a simple analytical model. *Environmental Science & Technology*, *48*(19), 11369–11378.

Haggerty, R., Wondzell, S. M., & Johnson, M. A. (2002). Power-law residence time distribution in the hyporheic zone of a 2nd-order mountain stream. *Geophysical Research Letters*, *29*(13), 11–18.

Hartigan, J. A., & Hartigan, P. M. (1985). The dip test of unimodality. *The Annals of Statistics*, 70–84.

Harvey, J., & Gooseff, M. (2015). River corridor science: Hydrologic exchange and ecological consequences from bedforms to basins. *Water Resources Research*, *51*(9), 6893–6922.

Harvey, J. W., Böhlke, J. K., Voytek, M. A., Scott, D., & Tobias, C. R. (2013). Hyporheic zone denitrification: Controls on effective reaction depth and contribution to whole-stream mass balance. *Water Resources Research*, *49*(10), 6298–6316.

Herzog, S. P., Higgins, C. P., Singha, K., & McCray, J. E. (2018). Performance of engineered streambeds for inducing hyporheic transient storage and attenuation of resazurin. *Environmental Science & Technology*, *52*(18), 10627–10636.

Hester, E. T., Eastes, L. A., & Widdowson, M. A. (2019). Effect of Surface Water Stage Fluctuation on Mixing-Dependent Hyporheic Denitrification in Riverbed Dunes. *Water Resources Research*, *55*(6), 4668–4687. https://doi.org/10.1029/2018WR024198

Hester, E. T., & Gooseff, M. N. (2010). Moving beyond the banks: Hyporheic restoration is fundamental to restoring ecological services and functions of streams. In *Environmental Science and Technology* (Vol. 44, Issue 5, pp. 1521–1525). American Chemical Society. https://doi.org/10.1021/es902988n

Hester, E. T., Santizo, K. Y., Nida, A. A., & Widdowson, M. A. (2021). Hyporheic transverse mixing zones and dispersivity: Laboratory and numerical experiments of hydraulic controls. *Journal of Contaminant Hydrology*, *243*, 103885. https://doi.org/10.1016/j.jconhyd.2021.103885

Hester, E. T., Young, K. I., & Widdowson, M. A. (2013). Mixing of surface and groundwater induced by riverbed dunes: Implications for hyporheic zone definitions and pollutant reactions. *Wiley Online Library*, *49*(9), 5221–5237. https://doi.org/10.1002/wrcr.20399

Higashino, M., Clark, J. J., & Stefan, H. G. (2009). Pore water flow due to near-bed turbulence and associated solute transfer in a stream or lake sediment bed. *Water Resources Research*, *45*(12).

Hondzo, M., Feyaerts, T., Donovan, R., & O'Connor, B. L. (2005). Universal scaling of dissolved oxygen distribution at the sediment-water interface: A power law.

Limnology and Oceanography, *50*(5), 1667–1676. https://doi.org/10.4319/lo.2005.50.5.1667

Horritt, M. S., & Bates, P. D. (2002). Evaluation of 1D and 2D numerical models for predicting river flood inundation. *Journal of Hydrology*, *268*(1–4), 87–99. https://doi.org/10.1016/S0022-1694(02)00121-X

Hrachowitz, M., Benettin, P., van Breukelen, B. M., Fovet, O., Howden, N. J. K., Ruiz, L., van der Velde, Y., & Wade, A. J. (2016). Transit times—the link between hydrology and water quality at the catchment scale. In *Wiley Interdisciplinary Reviews: Water* (Vol. 3, Issue 5, pp. 629–657). John Wiley and Sons Inc. https://doi.org/10.1002/wat2.1155

Huang, P., & Chui, T. F. M. (2018). Empirical Equations to Predict the Characteristics of Hyporheic Exchange in a Pool-Riffle Sequence. *Groundwater*, *56*(6), 947–958. https://doi.org/10.1111/gwat.12641

Huettel, M., Røy, H., Precht, E., & Ehrenhauss, S. (2003). Hydrodynamical impact on biogeochemical processes in aquatic sediments. In *The Interactions between Sediments and Water* (pp. 231–236). Springer Netherlands. https://doi.org/10.1007/978-94-017-3366-3_31

Jørgensen, B. B., & des Marais, D. J. (1990). The diffusive boundary layer of sediments: Oxygen microgradients over a microbial mat. *Limnology and Oceanography*, *35*(6), 1343–1355. https://doi.org/10.4319/lo.1990.35.6.1343

Julien, P. Y. (2002). *River Mechanics*. Cambridge University Press. https://doi.org/10.1017/CBO9781139164016

Kang, Y. J., & Noh, Y. (2019). Development of Hartigan's Dip Statistic with Bimodality Coefficient to Assess Multimodality of Distributions. *Mathematical Problems in Engineering*, *2019*. https://doi.org/10.1155/2019/4819475

Kaushal, S. S., Duan, S., Doody, T. R., Haq, S., Smith, R. M., Newcomer Johnson, T. A., Newcomb, K. D., Gorman, J., Bowman, N., Mayer, P. M., Wood, K. L., Belt, K. T., & Stack, W. P. (2017). Human-accelerated weathering increases salinization, major

ions, and alkalinization in fresh water across land use. *Applied Geochemistry*, *83*, 121–135. https://doi.org/10.1016/j.apgeochem.2017.02.006

Kaushal, S. S., Gold, A. J., Bernal, S., Johnson, T. A. N., Addy, K., Burgin, A., Burns, D. A., Coble, A. A., Hood, E., Lu, Y. H., Mayer, P., Minor, E. C., Schroth, A. W., Vidon, P., Wilson, H., Xenopoulos, M. A., Doody, T., Galella, J. G., Goodling, P., … Belt, K. T. (2018). Watershed 'chemical cocktails': forming novel elemental combinations in Anthropocene fresh waters. *Biogeochemistry*, *141*(3), 281–305. https://doi.org/10.1007/s10533-018-0502-6

Kaushal, S. S., Groffman, P. M., Likens, G. E., Belt, K. T., Stack, W. P., Kelly, V. R., Band, L. E., & Fisher, G. T. (2005). Increased salinization of fresh water in the Northeastern United States. *Proceedings of the National Academy of Sciences of the United States of America*, *102*(38), 13517–13520. https://doi.org/10.1073/pnas.0506414102

Kaushal, S. S., Likens, G. E., Pace, M. L., Haq, S., Wood, K. L., Galella, J. G., Morel, C., Doody, T. R., Wessel, B., Kortelainen, P., Räike, A., Skinner, V., & Utz, R. (2019). Novel 'chemical cocktails' in inland waters are a consequence of the freshwater salinization syndrome. *Philosophical Transactions of the Royal Society B: Biological Sciences*, *374*(1764). https://doi.org/10.1098/rstb.2018.0017

Kaushal, S. S., Likens, G. E., Pace, M. L., Reimer, J. E., Maas, C. M., Galella, J. G., Utz, R. M., Duan, S., Kryger, J. R., Yaculak, A. M., Boger, W. L., Bailey, N. W., Haq, S., Wood, K. L., Wessel, B. M., Park, C. E., Collison, D. C., Aisin, B. Y. 'aaqob I., Gedeon, T. M., … Woglo, S. A. (2021). Freshwater salinization syndrome: from emerging global problem to managing risks. *Biogeochemistry*, *154*(2), 255–292. https://doi.org/10.1007/s10533-021-00784-w

Kaushal, S. S., Likens, G. E., Pace, M. L., Utz, R. M., Haq, S., Gorman, J., & Grese, M. (2018). Freshwater salinization syndrome on a continental scale. *Proceedings of the National Academy of Sciences of the United States of America*, *115*(4), E574–E583. https://doi.org/10.1073/pnas.1711234115

Kaushal, S. S., Mayer, P. M., Likens, G. E., Reimer, J. E., Maas, C. M., Rippy, M. A., Grant, S. B., Hart, I., Utz, R. M., Shatkay, R. R., Wessel, B. M., Maietta, C. E., Pace, M. L., Duan, S., Boger, W. L., Yaculak, A. M., Galella, J. G., Wood, K. L., Morel, C. J., … Becker, W. D. (2022). Five state factors control progressive stages of freshwater

salinization syndrome. *Limnology And Oceanography Letters*. https://doi.org/10.1002/lol2.10248

Kefford, B. J., Papas, P. J., & Nugegoda, D. (2003). Relative salinity tolerance of macroinvertebrates from the Barwon River, Victoria, Australia. *Marine and Freshwater Research*, *54*(6), 755–765. https://doi.org/10.1071/MF02081

Keller, E. A. (1972). Development of alluvial stream channels: A five-stage model. *Bulletin of the Geological Society of America*, *83*(5), 1531–1536. https://doi.org/10.1130/0016-7606(1972)83[1531:DOASCA]2.0.CO;2

Kim, T., Blois, G., Best, J. L., & Christensen, K. T. (2020). Experimental evidence of amplitude modulation in permeable-wall turbulence. *Journal of Fluid Mechanics*, *887*.

Kirchner, J. W., Feng, X., & Neal, C. (2000). Frail chemistry and its implications for contaminant transport in catchments. *Nature*, *403*(6769), 524–527. https://doi.org/10.1038/35000537

Kitanidis, P. K. (1995). Quasi-Linear Geostatistical Theory for Inversing. *Water Resources Research*, *31*(10), 2411–2419. https://doi.org/10.1029/95WR01945

Kitanidis, P. K. (1996). On the geostatistical approach to the inverse problem. *Advances in Water Resources*, *19*(6), 333–342. https://doi.org/10.1016/0309-1708(96)00005-X

Kleinhans, M. G., & Vollmer, S. (2008). Effects of particle exposure, near-bed velocity and pressure fluctuations on incipient motion of particle-size mixtures Bio-morphological modeling of dynamic vegetation characteristics on estuarine planform and shape. View project Martian Chaotic Terrains View project Effects of particle exposure, near-bed velocity and pressure fluctuations on incipient motion of particle-size mixtures. *Vliz.Be*. https://doi.org/10.1201/NOE0415453639-c70

Knapp, J. L. A., González-Pinzón, R., Drummond, J. D., Larsen, L. G., Cirpka, O. A., & Harvey, J. W. (2017). Tracer-based characterization of hyporheic exchange and benthic biolayers in streams. *Water Resources Research*, *53*(2), 1575–1594.

Knapp, J. L. A., & Kelleher, C. (2020). A perspective on the future of transient storage modeling: Let's stop chasing our tails. *Water Resources Research*, *56*(3), e2019WR026257.

Lai, J. L., Lo, S. L., & Lin, C. F. (1994). Effects of hydraulic and medium characteristics on solute transfer to surface runoff. *Water Science and Technology*, *30*(7), 145.

Laube, G., Schmidt, C., & Fleckenstein, J. H. (2018). The systematic effect of streambed conductivity heterogeneity on hyporheic flux and residence time. *Advances in Water Resources*, *122*, 60–69.

Leopold, L. B., & Wolman, M. G. (1957). River channel patterns: Braided, meandering, and straight. In *Professional Paper*. https://doi.org/10.3133/PP282B

Letterman, R. (1999). *Water Quality and Treatment. AWW Association, ed*.

Liu, M. Y., Huai, W. X., & Chen, B. (2021). Predicting the effective diffusivity across the sediment–water interface in rivers. *Journal of Cleaner Production*, *292*. https://doi.org/10.1016/j.jclepro.2021.126085

Loh, W.-Y. (2011). Classification and regression trees. *Wiley Interdisciplinary Reviews: Data Mining and Knowledge Discovery*, *1*(1), 14–23.

Lorke, A., Müller, B., Maerki, M., & Wüest, A. (2003). Breathing sediments: The control of diffusive transport across the sediment-water interface by periodic boundary-layer turbulence. *Limnology and Oceanography*, *48*(6), 2077–2085. https://doi.org/10.4319/lo.2003.48.6.2077

Marie, A., & Vengosh, A. (2001). Sources of Salinity in Ground Water from Jericho Area, Jordan Valley. *Ground Water*, *39*(2), 240–248. https://doi.org/10.1111/j.1745-6584.2001.tb02305.x

Marion, A., Bellinello, M., Guymer, I., & Packman, A. (2002). Effect of bed form geometry on the penetration of nonreactive solutes into a streambed. *Water Resources Research*, *38*(10), 21–27.

Marzadri, A., Dee, M. M., Tonina, D., Bellin, A., & Tank, J. L. (2017). Role of surface and subsurface processes in scaling N2O emissions along riverine networks. *Proceedings of the National Academy of Sciences*, *114*(17), 4330–4335.

Marzadri, A., Tonina, D., Bellin, A., & Tank, J. L. (2014). A hydrologic model demonstrates nitrous oxide emissions depend on streambed morphology. *Geophysical Research Letters*, *41*(15), 5484–5491.

Marzadri, A., Tonina, D., Bellin, A., & Valli, A. (2016). Mixing interfaces, fluxes, residence times and redox conditions of the hyporheic zones induced by dune-like bedforms and ambient groundwater flow. *Advances in Water Resources*, *88*, 139–151.

Marzadri, A., Tonina, D., Bellin, A., Vignoli, G., & Tubino, M. (2010). Semianalytical analysis of hyporheic flow induced by alternate bars. *Water Resources Research*, *46*(7). https://doi.org/10.1029/2009WR008285

McGuire, K. J., McDonnell, J. J., Weiler, M., Kendall, C., McGlynn, B. L., Welker, J. M., & Seibert, J. (2005). The role of topography on catchment-scale water residence time. *Water Resources Research*, *41*(5).

Meybeck, M., & Helmer, R. (1989). The quality of rivers: From pristine stage to global pollution. *Palaeogeography, Palaeoclimatology, Palaeoecology*, *75*(4), 283–309. https://doi.org/10.1016/0031-0182(89)90191-0

Monofy, A., & Boano, F. (2021). The Effect of Streamflow, Ambient Groundwater, and Sediment Anisotropy on Hyporheic Zone Characteristics in Alternate Bars. *Water Resources Research*, *57*(1), e2019WR025069. https://doi.org/10.1029/2019WR025069

Morén, I., Wörman, A., & Riml, J. (2017). Design of remediation actions for nutrient mitigation in the hyporheic zone. *Water Resources Research*, *53*(11), 8872–8899.

Mulholland, M. R., Boneillo, G. E., Bernhardt, P. W., & Minor, E. C. (2009). Comparison of nutrient and microbial dynamics over a seasonal cycle in a mid-Atlantic coastal lagoon prone to Aureococcus anophagefferens (brown tide) blooms. *Estuaries and Coasts*, *32*(6), 1176–1194. https://doi.org/10.1007/s12237-009-9218-0

Myers, G. E. (1971). *Analytical methods in conduction heat transfer*. McGraw-Hill Book Company, New York.

Nagaoka, H., & Ohgaki, S. (1990). Mass transfer mechanism in a porous riverbed. *Water Research*, *24*(4), 417–425.

Nakagawa, H. (2017). *Turbulence in open channel flows*. Routledge.

Nelson, P. H. (1994). Permeability-porosity relationships in sedimentary rocks. *The Log Analyst*, *35*(03).

Newcomer, M. E., Hubbard, S. S., Fleckenstein, J. H., Maier, U., Schmidt, C., Thullner, M., Ulrich, C., Flipo, N., & Rubin, Y. (2016). Simulating bioclogging effects on dynamic riverbed permeability and infiltration. *Water Resources Research*, *52*(4), 2883–2900.

O'Connor, B. L., & Harvey, J. W. (2008). Scaling hyporheic exchange and its influence on biogeochemical reactions in aquatic ecosystems. *Water Resources Research*, *44*(12).

Ott, R., Longnecker, M., & Ott, L. (2004). *A first course in statistical methods*. https://users.stat.ufl.edu/~winner/sta6166/Solutions/Table%20of%20Contents.pdf

Packman, A. I., Brooks, N. H., & Morgan, J. J. (2000a). A physicochemical model for colloid exchange between a stream and a sand streambed with bed forms. *Water Resources Research*, *36*(8), 2351–2361.

Packman, A. I., Brooks, N. H., & Morgan, J. J. (2000b). Kaolinite exchange between a stream and streambed: Laboratory experiments and validation of a colloid transport model. *Water Resources Research*, *36*(8), 2363–2372.

Packman, A. I., & MacKay, J. S. (2003). Interplay of stream-subsurface exchange, clay particle deposition, and streambed evolution. *Water Resources Research*, *39*(4).

Packman, A. I., & Salehin, M. (2003). Relative roles of stream flow and sedimentary conditions in controlling hyporheic exchange. *Hydrobiologia*, *494*, 291–297. https://doi.org/10.1023/A:1025403424063

Packman, A. I., Salehin, M., & Zaramella, M. (2004). Hyporheic exchange with gravel beds: basic hydrodynamic interactions and bedform-induced advective flows. *Journal of Hydraulic Engineering*, *130*(7), 647–656.

Paul, R., Brindha, K., Gowrisankar, G., Tan, M. L., & Singh, M. K. (2019). Identification of hydrogeochemical processes controlling groundwater quality in Tripura, Northeast India using evaluation indices, GIS, and multivariate statistical methods. *Environmental Earth Sciences*, *78*(15), 1–16. https://doi.org/10.1007/s12665-019-8479-6

Press, W. H. (1992). *Numerical recipes in FORTRAN : the art of scientific computing*. Cambridge University Press.

Ramos, P. L., Nascimento, D., & Louzada, F. (2017). The Long Term Fr\'echet distribution: Estimation, Properties and its Application. *ArXiv Preprint ArXiv:1709.07593*.

Raymond, P. A., Oh, N. H., Turner, R. E., & Broussard, W. (2008). Anthropogenically enhanced fluxes of water and carbon from the Mississippi River. *Nature*, *451*(7177), 449–452. https://doi.org/10.1038/nature06505

Rehg, K. J., Packman, A. I., & Ren, J. (2005). Effects of suspended sediment characteristics and bed sediment transport on streambed clogging. *Hydrological Processes: An International Journal*, *19*(2), 413–427.

Reidenbach, M. A., Limm, M., Hondzo, M., & Stacey, M. T. (2010). Effects of bed roughness on boundary layer mixing and mass flux across the sediment-water interface. *Water Resources Research*, *46*(7).

Ren, J., & Packman, A. I. (2004). Stream-subsurface exchange of zinc in the presence of silica and kaolinite colloids. *Environmental Science & Technology*, *38*(24), 6571–6581.

Rengasamy, P. (2006). World salinization with emphasis on Australia. *Journal of Experimental Botany*, *57*(5), 1017–1023. https://doi.org/10.1093/jxb/erj108

Richardson, C. P., & Parr, A. D. (1988). Modified Fickian model for solute uptake by runoff. *Journal of Environmental Engineering*, *114*(4), 792–809.

Roche, K. R., Blois, G., Best, J. L., Christensen, K. T., Aubeneau, A. F., & Packman, A. I. (2018). Turbulence links momentum and solute exchange in coarse-grained streambeds. *Water Resources Research*, *54*(5), 3225–3242.

Roche, K. R., Li, A., Bolster, D., Wagner, G. J., & Packman, A. I. (2019). Effects of turbulent hyporheic mixing on reach-scale transport. *Water Resources Research*, *55*(5), 3780–3795.

Runkel, R. L. (1998). *One-dimensional transport with inflow and storage (OTIS): A solute transport model for streams and rivers* (Vol. 98, Issue 4018). US Department of the Interior, US Geological Survey.

Salameh, E. (2001). Sources of Water Salinities in the Jordan Valley Area/Jordan. *Acta Hydrochimica et Hydrobiologica*, *29*(6–7), 329. https://doi.org/10.1002/1521-401X(200112)29:6/7<329::AID-AHEH329>3.0.CO;2-6

Salehin, M., Packman, A. I., & Paradis, M. (2004). Hyporheic exchange with heterogeneous streambeds: Laboratory experiments and modeling. *Water Resources Research*, *40*(11).

Santizo, K. Y., Widdowson, M. A., & Hester, E. T. (2020). Abiotic Mixing-Dependent Reaction in a Laboratory Simulated Hyporheic Zone. *Water Resources Research*, *56*(9). https://doi.org/10.1029/2020WR027090

Santos, I. R., Eyre, B. D., & Huettel, M. (2012). The driving forces of porewater and groundwater flow in permeable coastal sediments: A review. In *Estuarine, Coastal and Shelf Science* (Vol. 98, pp. 1–15). Academic Press. https://doi.org/10.1016/j.ecss.2011.10.024

Sawyer, A. H., Bayani Cardenas, M., & Buttles, J. (2012). Hyporheic temperature dynamics and heat exchange near channel-spanning logs. *Water Resources Research*, *48*(1).

Sawyer, A. H., & Cardenas, M. B. (2009). Hyporheic flow and residence time distributions in heterogeneous cross-bedded sediment. *Water Resources Research*, *45*(8).

Schulz, C.-J., & Cañedo-Argüelles, M. (2019). Lost in translation: the German literature on freshwater salinization. *Philosophical Transactions of the Royal Society B: Biological Sciences*, *374*(1764), 20180007. https://doi.org/10.1098/rstb.2018.0007

Schwarz, G., & others. (1978). Estimating the dimension of a model. *Annals of Statistics*, *6*(2), 461–464.

Shammas, N. K., & Wang, L. K. (2015). *Water engineering: hydraulics, distribution and treatment*. John Wiley & Sons.

Snodgrass, M. F., & Kitanidis, P. K. (1997). A geostatistical approach to contaminant source identification. *Water Resources Research*, *33*(4), 537–546. https://doi.org/10.1029/96WR03753

Stets, E. G., Sprague, L. A., Oelsner, G. P., Johnson, H. M., Murphy, J. C., Ryberg, K., Vecchia, A. v., Zuellig, R. E., Falcone, J. A., & Riskin, M. L. (2020). Landscape Drivers of Dynamic Change in Water Quality of U.S. Rivers. *Environmental Science and Technology*, *54*(7), 4336–4343. https://doi.org/10.1021/acs.est.9b05344

Stewardson, M. J., Datry, T., Lamouroux, N., Pella, H., Thommeret, N., Valette, L., & Grant, S. B. (2016). Variation in reach-scale hydraulic conductivity of streambeds. *Geomorphology*, *259*, 70–80.

Sukhodolov, A. N., Fedele, J. J., & Rhoads, B. L. (2006). Structure of flow over alluvial bedforms: an experiment on linking field and laboratory methods. *Earth Surface Processes and Landforms: The Journal of the British Geomorphological Research Group*, *31*(10), 1292–1310.

Thibodeaux, L. J., & Boyle, J. D. (1987). Bedform-Generated convective transport in Bottom sediment. *Nature*, *325*(6102), 341–343. https://doi.org/10.1038/325341a0

Tjandraatmadja, G., Pollard, C., Sheedy, C., & Gozukara, Y. (2010). *Sources of contaminants in domestic wastewater: nutrients and additional elements from household products Water for a Healthy Country Flagship Report series*. www.scienceimage.csiro.au

Tomasek, A. A., Hondzo, M., Kozarek, J. L., Staley, C., Wang, P., Lurndahl, N., & Sadowsky, M. J. (2019). Intermittent flooding of organic-rich soil promotes the formation of denitrification hot moments and hot spots. *Ecosphere*, *10*(1), e02549. https://doi.org/10.1002/ecs2.2549

Tonina, D., & Buffington, J. M. (2007). Hyporheic exchange in gravel bed rivers with pool-riffle morphology: Laboratory experiments and three-dimensional modeling. *Water Resources Research*, *43*(1).

Tonina, D., & Buffington, J. M. (2009). Hyporheic exchange in mountain rivers I: Mechanics and environmental effects. In *Geography Compass* (Vol. 3, Issue 3, pp. 1063–1086). https://doi.org/10.1111/j.1749-8198.2009.00226.x

Tonina, D., & Buffington, J. M. (2011). Effects of stream discharge, alluvial depth and bar amplitude on hyporheic flow in pool-riffle channels. *Water Resources Research*, *47*(8). https://doi.org/10.1029/2010WR009140

Tonina, D., de Barros, F. P. J., Marzadri, A., & Bellin, A. (2016). Does streambed heterogeneity matter for hyporheic residence time distribution in sand-bedded streams? *Advances in Water Resources*, *96*, 120–126.

Tonina, D., Marzadri, A., & Bellin, A. (2015). Benthic uptake rate due to hyporheic exchange: The effects of streambed morphology for constant and sinusoidally varying nutrient loads. *Water*, *7*(2), 398–419.

Tóth, J. (1962). A theory of groundwater motion in small drainage basins in central Alberta, Canada. *Journal of Geophysical Research*, *67*(11), 4375–4388.

Trauth, N., Schmidt, C., Maier, U., Vieweg, M., & Fleckenstein, J. H. (2013). Coupled 3-D stream flow and hyporheic flow model under varying stream and ambient groundwater flow conditions in a pool-riffle system. *Water Resources Research*, *49*(9), 5834–5850.

van den Berg, J. H. (1995). Prediction of alluvial channel pattern of perennial rivers. *Geomorphology*, *12*(4), 259–279. https://doi.org/10.1016/0169-555X(95)00014-V

Vaux, W. G. (1968). Intragravel flow and interchange of water in a streambed. *Fishery Bulletin of the Fish and Wildlife Service*, *66*(3), 479–489.

Voermans, J. J., Ghisalberti, M., & Ivey, G. N. (2017). The variation of flow and turbulence across the sediment–water interface. *Journal of Fluid Mechanics*, *824*, 413–437.

Voermans, J. J., Ghisalberti, M., & Ivey, G. N. (2018). A Model for Mass Transport Across the Sediment-Water Interface. *Water Resources Research*, *54*(4), 2799–2812. https://doi.org/10.1002/2017WR022418

White, D. S., Elzinga, C. H., & Hendricks, S. P. (1987). Temperature patterns within the hyporheic zone of a northern Michigan river. *Journal of the North American Benthological Society*, *6*(2), 85–91.

Williams, W. D. (2001). Anthropogenic salinisation of inland waters. In *Saline Lakes* (pp. 329–337). Springer Netherlands. https://doi.org/10.1007/978-94-017-2934-5_30

Wörman, A., Packman, A. I., Johansson, H., & Jonsson, K. (2002). Effect of flow-induced exchange in hyporheic zones on longitudinal transport of solutes in streams and rivers. *Water Resources Research*, *38*(1), 1–2.

Wörman, A., Packman, A. I., Marklund, L., Harvey, J. W., & Stone, S. H. (2007). Fractal topography and subsurface water flows from fluvial bedforms to the continental shield. *Geophysical Research Letters*, *34*(7), L07402. https://doi.org/10.1029/2007GL029426

Wu, F.-C. (2000). Modeling embryo survival affected by sediment deposition into salmonid spawning gravels: Application to flushing flow prescriptions. *Water Resources Research*, *36*(6), 1595–1603.

Wu, L., Singh, T., Gomez-Velez, J., Nützmann, G., Wörman, A., Krause, S., & Lewandowski, J. (2018). Impact of Dynamically Changing Discharge on Hyporheic Exchange Processes Under Gaining and Losing Groundwater Conditions. *Water Resources Research*, *54*(12), 10,076-10,093. https://doi.org/10.1029/2018WR023185

Yates, S. R. (1992). An analytical solution for one-dimensional transport in porous media with an exponential dispersion function. *Water Resources Research*, *28*(8), 2149–2154. https://doi.org/10.1029/92WR01006

Zaramella, M., Packman, A. I., & Marion, A. (2003). Application of the transient storage model to analyze advective hyporheic exchange with deep and shallow sediment beds. *Water Resources Research*, *39*(7).

Zarnetske, J. P., Haggerty, R., Wondzell, S. M., Bokil, V. A., & González-Pinzón, R. (2012). Coupled transport and reaction kinetics control the nitrate source-sink function of hyporheic zones. *Water Resources Research*, *48*(11).

Zhong, Q., Chen, Q., Wang, H., Li, D., & Wang, X. (2016). Statistical analysis of turbulent super-streamwise vortices based on observations of streaky structures near the free surface in the smooth open channel flow. *Water Resources Research*, *52*(5), 3563–3578.